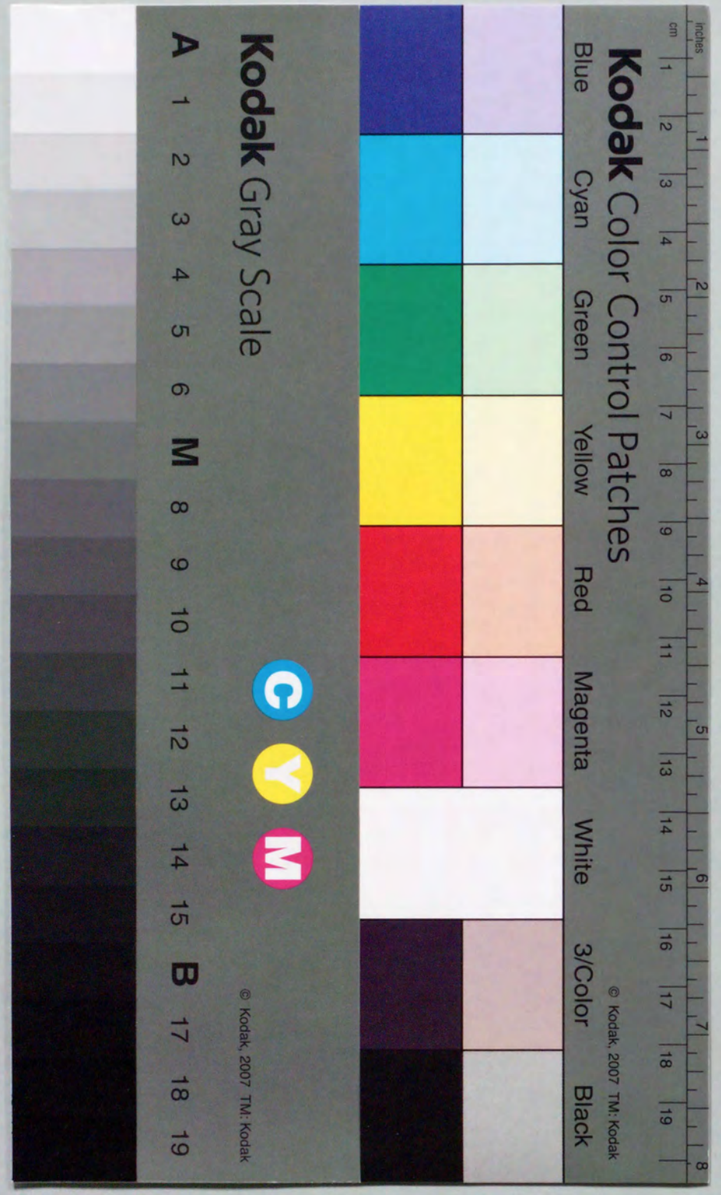

Hyperfine Interactions of Short-Lived ^{12}B in Si Crystal

Takuji Izumikawa

DISSERTATION IN PHYSICS

THE OSAKA UNIVERSITY

GRADUATE SCHOOL OF SCIENCE

TOYONAKA, OSAKA

(1)

Hyperfine Interactions of Short-Lived ^{12}B in Si Crystal

Takuji Izumikawa

Dissertation in Physics, 1999

Graduate School of Science
Osaka University
Toyonaka, Osaka, Japan

Abstract

The lattice locations of boron atom implanted in the semiconductor Si were studied by detecting β-NMR using the polarized β-emitter ^{12}B. While the B atom is one of the typical dopants in Si, little has been known rigidly about the location of implanted B except for the substitutional site and the temperature dependence of its fraction. Moreover, in the previous β-NMR studies there was a missing fraction ($\sim$30 %) of implanted B and were some contradictions even in the fraction of the substitutional B. The purpose of the present study is to investigate the locations of the implanted B and their fractions as a function of temperature through the careful detection of the β-NMR in order to understand the behavior of B atoms in Si.

The polarized ^{12}B nuclei were produced through ^{11}B(d, p)^{12}B reaction with the deuteron of 1.5 MeV and with restricting the recoil angle of about 40°. The ^{12}B was implanted in a Si sample, whose temperature was kept constant, placed with its $\langle 110 \rangle$ axis set parallel to the applied magnetic field of 6.000 kOe. Then applying rf and detecting β-ray from ^{12}B nuclei, we observed the NMR of the ^{12}B in Si. Three Si samples with different densities of dopants were prepared (3×10^{14} B/cm^3, 7×10^{17} B/cm^3, 6×10^{14} P/cm^3). From the resonance frequencies and NMR amplitudes, we distinguished the lattice sites and obtained their fractions.

It has been known before the present study that the main fraction of ^{12}B is located in the substitutional (B_s) site and some fraction is located in a nonsubstitutional (B_{ns}) site with $\langle 111 \rangle$ axial symmetry. In addition to these two sites, we found in the present study a broad resonance around the Larmor frequency, which we call the B_x site. Thus, at the temperature below 260 K, all the fractions of the implanted ^{12}B were made clear without any missing fraction.

The fractions of these three different sites were measured as a function of temperature in a range from 100 K to 800 K. Two remarkable results were obtained; (1) the B_{ns} nuclei become undetectable suddenly at 260 K and above; (2) while the sum of the fractions ($B_s + B_x$) is constant from 100 K to 450 K, the fraction increases to 100 % above 450 K.

The steep decrease of B_{ns} fraction is caused by a thermal jump of the B_{ns} atom between the identical locations, *i.e.*, the fluctuating electric field gradient due to the thermal jump causes the fast spin-lattice relaxation of the nuclear polarization of ^{12}B

in B_{ns} sites. Assuming the Arrhenius behavior of the thermal jump, the jump rate of the B_{ns} was deduced based on the (B_s- Si_i) pair model for the atomic configuration which was predicted theoretically to be most probable. The obtained jumping rate is (2.5×10^9) $\exp(-0.47 \pm 0.04(\mathrm{eV})/kT)$ kHz (the error of the pre-exponential factor is $+6 \times 10^9$, -1.5×10^9). As well as the decrease of the B_{ns} fraction, the recovery of the ^{12}B fraction in the B_s site or the B_x site above 450 K is successfully understood by the dissociation of (B_s- Si_i) pair with the dissociation rate of $5 \times 10^9 \exp(-0.84 \pm 0.06(\mathrm{eV})/kT)$ kHz (the error of the pre-exponential factor is $+1.1 \times 10^{10}$, -3.5×10^9). Thus the two remarkable features are consistently explained by the thermal jump and the dissociation within the (B_s- Si_i) pair model.

The electric field gradient q at the B_{ns} site was precisely determined to be $1.14 \pm 0.04 \times 10^{17}$ V/cm^2. In order to make sure the atomic configuration for B_{ns} site, a theoretical calculation based on the KKR method for the energy minimum configuration and for the field gradient is urged.

It was disclosed that the broad resonance ($\sim$10 kHz) from B_x site is due to static quadrupole interactions with no special symmetry. The fraction of B_x decreases as increasing temperature. From the these results, the most probable site for the B_x component is also the substitutional site with small electric field gradient due to crystal defects like vacancies. However, the detail of the character and the cause of this defect need further advanced investigation.

Although the present study is still in the first stage of the β-NMR study of semiconductor Si, we detected for the first time all the diamagnetic state of the implanted B and revealed a dynamic behavior of the boron related defects.

Contents

Acknowledgments

The author wishes to express his sincere gratitude to all of those who have helped to make this work successful:

Professor T. Minamisono for his proposing the present experiment, providing earnest guidance and discussing during the work, and encouragement.

Associated Professor K. Matsuta for his providing earnest guidance and discussions, constant collaboration, and encouragement.

Professor Y. Nojiri for his constant collaboration, discussions, and encouragement.

Research Associate M. Fukuda for his constant collaboration, discussions, and encouragement.

Professor G. Langouche for his valuable advice and providing me with samples.

Dr. T. Ohtsubo for his constant collaboration, discussions, and encouragement.

Mr. Y. Takahashi for his technical supports during the experiment and for the Van de Graaff Accelerator.

Mr. M. Sakamoto for his technical supports during the experiment and for the developing the experimental setups.

Mr. T. Mizuta and Mr. K. Onishi for thier technical supports during the experiment.

Dr. M. Tanigaki, Mr. T. Miyake, and Dr. K. Sato for their collaboration and discussions during the experiment.

Dr. S. Momota, Dr. S. Fukuda, Dr. M. Mihara, Dr. T. Yamaguchi, Dr. K. Minamisono, and Ms. Y. Maruyama for their supports in the experiment.

Ms. K. Ohsawa for her technical support concerning paper works.

Last, but not least, I would like to thank Professor N. Takahashi, Professor T. Ohyama, Professor H. Akai, and Associated Professor T. Shimoda for their encouragement and for reading this thesis.

Chapter 1

Introduction

We have investigated implantation sites of B and the related defects in semiconductor silicon by use of the β-NMR technique, which is one of the microscopic research methods.

Because the implantation of boron as a dopant into semiconductor Si is quite useful technique for the fabrication of semiconductor devices, macroscopic phenomena, such as the range of ions, the distribution of damage and the annealing of damage have been well studied [Zie92, Mos80, K$^+$86] in order to control the dopant location more strictly. However the microscopic knowledge like the implantation sites and the configuration and dynamics of defects has been still poor [FGP89].

Until now, ESR (Electron Spin Resonance) and channelling techniques have been widely used for the microscopic studies on the location of the boron in the lattice and on the defects associated with implantation. As described later, the ESR studies by Watkins on defects of electron-irradiated silicon greatly contributed to the physics of the defects in semiconductors [Wat63, Wat69, Sta98].

The NMR (Nuclear Magnetic Resonance) technique which is expected to bring the supplementary information of diamagnetic states of atoms is also quite helpful for the study of defects and lattice locations. It is, however, difficult to apply conventional NMR method to the dopants in semiconductors, because the NMR technique requires a large number of spins (typically 10^{18} spins). Therefore there has been only a few NMR studies on boron in extremely highly doped silicon [SH64, HK91, H$^+$92], which turns into, however, metallic Si whose electric properties are quite different from those of semiconductor Si.

In big contrast, the β-NMR technique used in the present study has great advantage compared with the conventional one, because of the large polarization of the probe nuclide, the short lived β-emitters, produced through nuclear reactions, that is a few hundred thousand times larger than the polarization created in nuclide placed in $\sim$10 kOe at thermal equilibrium at room temperature. Besides this advantage, because the measurement is based on the detection of the asymmetric β-ray distribution, this β-NMR has high sensitivity. For example, the impurity density of approximately 10^8

spins/cm^3·s was sufficient for the present study. Therefore, unlike the conventional NMR, the β-NMR technique is a very efficient tool for the study of dilute impurities such as dopants in semiconductor. In addition to this again, the high sensitivity of this technique makes the measurements free from the effect due to the radiation damages caused by its implantation. Such damages are unavoidable in the channelling experiments which required much more dose of ions into the sample.

Up to now, taking advantages mentioned above, the lattice location of ^{12}B in Si was already studied to some extent using the β-NMR technique by McDonald *et al.* [MM74,MM76], Minamisono *et al.* [MNDA83] and Ackermann *et al.* [MSS$^+$90a,SFD$^+$92] independently. From these researches, it was disclosed that a part of the implanted boron is settled at the substitutional site of Si lattice and its fraction relative to the all of the implanted B depends on the temperature. As temperature increases, the fraction of substitutional B increases. However, they gave different values on the fraction. This inconsistency has to be clarified. In addition to this discrepancy, a nonsubstitutional site with $\langle 111 \rangle$ axial symmetry was found by Ackermann *et al.* [FSD$^+$92]. The fraction of the nonsubstitutional B has to be clarified since, it was not studied in detail then, at least on its temperature dependence *etc.*

Though the two implantation sites of B in Si were found by use of the ESR technique, the fractions of the discovered sites have been ambiguous still. In addition, the sum of borons in these two sites was considerably below the amount of the total implanted B. However, from the study of Minamisono *et al.* [MNDA83], it was known that the maintained polarization of ^{12}B is close to the reaction polarization at temperatures between 117 K and 285 K. In other words, there must be still missing fraction of B. In the present experiment, we studied all these two sites in detail as well as the identification of this missing fraction of B and their temperature dependences.

The followings are the contents of this paper. First of all overview of the previous studies on the lattice locations of B in Si will be described in the following section. In the next chapter, the principle of the β-NMR method used in this study will be described. In Chapter 3, the experimental apparatus, in Chapter 4, the experimental procedure and experimental results will be described. Finally in Chapter 5, interpretation of the present results will be given and will be compared with other previous studies.

1.1 Historical Overview

Before reviewing the microscopic studies like β-NMR, we will mention the annealing behavior of electrical activity of the B-implanted Si. The electrical activity is defined

as the fraction of the electrical conductivity relative to that expected from the dopant density. So it shows the fraction of the effective dopants, hence, is a direct probe of the fraction of the B atom in the substitutional site. As shown in Fig.1.1, the annealing behavior depends on the dose rate. At low doses ($< 10^{13}$/cm^3), the electrical activity increases as a function of temperature and approaches to 100 % monotonically, while at higher doses a 'negative annealing' region is observed. This negative annealing region II (in Fig.1.1) is interpreted in terms of a precipitation of B and formation of defects, where B atom is uncharged and cannot conduct carriers effectively. In region III, the number of substitutional B increases rapidly with the activation energy of about 5 eV. Since this activation energy is close to the sum of the formation energy of vacancy ($\sim$4 eV) and the migration energy of the B atom ($\sim$1 eV), this behavior in the region III is interpreted as the recombination of the precipitated B atom with the help of the vacancies which become thermally mobile. In this manner, the behavior of implanted atom depends on its implantation dose markedly.

In the present experiment, however, as the dose rate was about $\sim 10^4$ ions/cm^2·s and the total dose for one run of the measurement was less than 10^8 ions/cm^2, we can observe the phenomena arising from single B atom itself, free from the influence from other B impurities or the precipitated B cluster.

Channeling experiments

North and Gibson [NG70] and Fladda *et al.* [FBLS70] utilized α particles emitted from the ^{11}B(p, α)^{8}Be reaction to investigate the lattice location of B atom in Si by use of the channeling technique. After implantation at room temperature the fraction of B in the substitutional site showed variety from about 60 % for a dose of $\sim 10^{14}$ ions/cm^2 to about 30 % for a dose of $\sim 10^{15}$ ions/cm^2. They also found that the rest of the B atom does not occupy a perfect tetrahedral interstitial site, in contrast with the heavier group III elements [EDJM69]. For a reference, the naive pictures on the interstitial sites of B in the diamond structure is shown in Fig.1.4. In Fig.1.2, the experimental substitutional fraction given from the channeling experiments is illustrated as a function of dose (after Fink *et.al* [F$^+$83]). As for a interstitial site, they suggested some kinds of configuration [F$^+$83], but it could not be reliable to prove this due to the difficulty of the experiment or of the analysis of experimental results.

ESR measurement

The defects in Si crystals were intensively studied by use of ESR and ENDOR (Electron Nuclear Double Resonance) techniques by Watkins *et al.* They have found B related defects in B-doped Si [Wat75, TW80]. The defects were introduced by the electron irradiation technique in Si samples at low temperature (20.4 K), and then observed photo induced ESR or ENDOR signals, which were stable up to 50 K. This phenomenon is interpreted as follows. The defect has two energy levels (or three charge states of $B^{(-)}$, $B^{(0)}$ and $B^{(+)}$) in the band gap of Si; a single donor level ($B^{(0)}/B^{(+)}$, $E_c = -0.13$ eV) and a single acceptor level ($B^{(-)}/B^{(0)}$, E_c=−0.37 eV) [TW80, HNW87] (Fig.1.3). This defect shows negative-U property [BKS80] due to the Jahn–Teller effect with the metastable state $B^{(0)}$. Among these charge state, only the $B^{(0)}$ state is observed by ESR, because other two states are diamagnetic and are not detected. Initially, the $B^{(-)}$ states are produced by the electron irradiation. By the photo transition the $B^{(-)}$ states turn into the $B^{(0)}$ states as follows and are detected by ESR,

$$B^{(-)} \xrightarrow{h\nu} B^{(0)} + e^{-}.$$

However, the $B^{(0)}$ states release an electron to the conduction band by thermal activation at higher temperatures to be converted into $B^{(+)}$ state as

$$B^{(0)} \xrightarrow{0.13\ \mathrm{eV}} B^{(+)} + e^{-}.$$

As a result, ESR signal disappears at higher temperatures, since the ESR cannot detect the $B^{(+)}$ state directly. Thus, warming the sample up to 50 K, $B^{(0)}$ spectrum was lost, and, then by recooling it down to 20.4 K, the spectrum naturally appeared again.

The ESR study have established firmly that $B^{(0)}$ state is in a low-symmetry site (C_{1h}), which distorted slightly from the position with axial ⟨111⟩ symmetry (C_{3v}) in the {110} plane. In the $B^{(0)} \longleftrightarrow B^{(+)}$ thermal conversion, the major direction of ⟨111⟩ axis of the defect is unchanged but the memory of the direction of the off-axis distortion is lost. From this fact, they suggested that $B^{(+)}$ has pure ⟨111⟩ axial symmetry and in the conversion to $B^{(0)}$ it is distorted into one of the six possible directions provided by the three {110} planes containing this ⟨111⟩ axis.

They also found that the major ⟨111⟩ axis is changed to the other ⟨111⟩ direction when warmed up to about 180 K with its activation energy of about 0.60 eV. Moreover, after warmed up to about 300 K, no spectrum was observed. This thermal activation energy was proven to be about 0.6 eV, which was same as the activation energy for the ⟨111⟩ direction change. From this same activation energies of the direction change and

the annealing, they concluded that a migration causes not only the changes of the major ⟨111⟩ axis but also the annealing of the defect.

As mentioned above, though Watkins *et al.* found this B-related defect in Si and measured various properties of it, its microscopic configuration is still unknown. They proposed three possible configurations which agree with the observed symmetry of the defect (Fig.1.5).

β-NMR measurements

One of the sophisticated NMR method, the β-NMR, was developed at Osaka university by Sugimoto [S+66] and has been improved by Minamisono *et al.* [MNS74, MNO81, M+92]. Although it was developed in order to study nuclear physics, especially to measure nuclear moments, it was revealed to be a unique tool to investigate ion implantation process and hyperfine fields in solids [HNN+76, MY81, Min85, ONM+93, MSA+98]. However, a very few β-NMR experiments on semiconductor were carried out, compared with the studies on metallic samples so far. In Table 1.1, the studies on the locations of impurities in semiconductor Si are listed.

Table 1.1 β-NMR studies on locations of impurities in semiconductor Si.

Impurity (Probe)	Method	Temperature Dopant	Results Remarks	Ref.
Boron				
^{11}B(d,p)^{12}B	β-NMR	RT	ν_L	
E_i=1.5MeV		Unspecified (100-200	$\Rightarrow$ Frequency shifts	[MM74]
θ_R=45°		Ωcm)	(compared with metallic hosts)	
^{11}B(d,p)^{12}B	β-NMR	RT	$\Delta\nu_L, \Delta a$ (around ν_L(AFP))	
E_i=1.5MeV		Unspecified (130 Ωcm	$\Rightarrow$ f(sub) = 67(6)%	[MM76]
θ_R=45°		)		
^{11}B(d,p)^{12}B	β-NMR	100-900K	$\Delta a(T)$ around ν_L ($+-10$ kHz),	
E_i=2.9MeV	β-asym	Unspecified	$P(H_{ext})$	[MNDA83]
θ_R=20°			$\Rightarrow$ f(sub($\nu_L \pm$ 10kHz)) = 26 $\sim$ 92% (100$\sim$900K)	
			P/P_0=100% (117$\sim$285K)	
^{11}B(d,p)^{12}B	β-NMR	300$\sim$950K B (5×10^{18},	$\Delta a(T)$ $\Rightarrow$ f(sub)=20$\sim$100%	
E_i=1.5MeV		2×10^{15}, $<\times10^{13}$ /cc)	(300$\sim$950K)	[MSS$^+$90a,
θ_R=45°		P ($<\times10^{13}$, 9×10^{14}	Annealing process	MSS$^+$90b]
		/cc) Sb (1.5×10^{18} /cc)		
^{11}B(d,p)^{12}B	β-NMR	320K, 280K	eqQ/h=360(15)kHz at 320K	
E_i=1.5MeV		B 2×10^{15}/cc	$\langle 111\rangle$ B$^+$.	[FSD$^+$92]
θ_R=45°			Jump between four $\langle 111\rangle$ directions. Vanish eqQ split at 280K.	
^{11}B(d,p)^{12}B	β-NMR	50-1000K B (5×10^{18},	$\Delta a(T)$,	
E_i=1.5MeV		2×10^{15}, $<\times10^{13}$	eqQ split. $\Rightarrow$ f(sub)=0$\sim$100%	[SFD$^+$92,
θ_R=45°		/cc), P ($<\times10^{13}$, 9×10^{14}, 3×10^{18} /cc),	(50$\sim$1000K).	FSF$^+$93]
			$\Rightarrow$ Annealing process	
		Sb (1.5×10^{18} /cc)		
^{11}B(d,p)^{12}B	β-NMR	240,340K	At 240K eqQ/h=375(15)kHz	
E_i=1.5MeV		P(9×10^{14}/cc)	$\langle 111\rangle$ $\Rightarrow$ B$^+$ charge state.	[FAD$^+$93]
θ_R=45°			Disappear at 340K.	
^{11}B(d,p)^{12}B	β-NMR	50K$\sim$370K B (5×10^{18},	$\Delta a(T)$ at ν_Q	
E_i=1.5MeV		2×10^{15} /cc), P ($9\times$	$\Rightarrow$ Diffusive jumping.	[FDE$^+$94]
θ_R=45°		10^{14}, Schottoky diodes (Au 50nm))		

(Cont.)

(Cont.)

Impurity (Probe)	Method	Temperature Dopant	Results Remarks	Ref.
Nitrogen				
^{10}B(^{3}He,n)^{12}N	β-NMR	100-980K	No NMR signal near ν_L,	
E_i=3.0MeV	β-asym	Unspecified	P/P_0=37$\sim$0%(100$\sim$980K)	[MNDA83]
θ_R=20°				
Litium				
^{8}Li: p-induced fragmentation	Laser pumping of mass-separated beam	30-300K Si, Si(B), Si(P)	NMR at ν_L, $\Delta\nu_L$, $\Delta a(T)$	[B$^+$88]

Using the advantage of β-NMR method for dilute impurity, the first β-NMR experiment on ^{12}B implanted in Si was performed by McDonald *et al.* [MM74, MM76]. They observed a sharp resonance at the Larmor frequency and measured the linewidth as a function of crystal orientation relative to the external magnetic field. Comparing the experimental linewidths with the theoretical values obtained from second-moment calculations of the dipolar broadening (Table 1.2), they concluded that the resonance came from the ^{12}B nuclei in the substitutional sites. They also deduced the fraction of substitutional B (67 ± 7 %) at room temperature from the amplitude of the spectrum.

In 1983, the temperature dependence of the substitutional ^{12}B fraction was observed by Minamisono *et al.* for the first time [MNDA83]. As shown in Fig.1.6, the fraction is about 30 % at the low temperature (100 K) and it increases with temperature until it reaches 100 % at 800 K. It is noted that the fraction at temperatures between 300 K and 500 K shows constant plateau. On the contrary, they also revealed that all the polarization of ^{12}B produced in nuclear reaction is maintained below 285 K, though only a part of the polarization was observed at the Larmor frequency. Thus two problems have been left unsolved; why the substitutional fraction shows such temperature dependence and where is the location of the missing ^{12}B at low temperatures.

Table 1.2 Line widths of the resonances at the Larmor frequency.(From [MM76].)

Crystal orientation	Linewidth (FWHM in Hz)		
	Exp.	Theory (substitutional)	Theory (Tetrahedral)
$\langle 100 \rangle$	107 ± 19	80	197
$\langle 110 \rangle$	168 ± 19	196	202
$\langle 111 \rangle$	194 ± 19	220	203

Since 1990, a research group in Germany has been studying on this problem. Their results are summarized as follows ([MSS$^+$90a, SFD$^+$92, FSF$^+$93, FSD$^+$92, FDE$^+$94]).

(1) As shown in Fig.1.7, the fraction of the substitutional B is almost zero at low temperature (50 K). It increases monotonically to almost 100 % at high temperature.

(2) The fraction of the substitutional B depend not only on temperature but also on the type and the density of the dopant. In the heavily p-type impurity doped Si case, a plateau was found at above 400 K. Going toward intrinsic material and toward further n-type impurity doped material the plateau becomes shorter and eventually disappears completely. Another remarkable feature is the doping dependence of the saturation

temperature. It increases from 600 K to 1000 K going from heavily doped n-type Si to heavily doped p-type Si.

(3) According to their qualitative interpretation, there are two sites for the implanted ^{12}B, one is substitutional site and the other is nonsubstitutional site; primary location just after the implantation is the nonsubstitutional site independent of temperature, and then nonsubstitutional B diffuse into the substitutional site by thermal activation within the nuclear lifetime of ^{12}B. Based on this view, they deduced activation energies as shown in Table 1.3.

Table 1.3 Activation energy for a substitutional B in Si. (After [MSS$^+$90a])

Sample number	Type of conduction	Dopant	Dopant concentration (cm^{-3})	Production process	Logarithm of pre-exponent factor $\log_{10}(\mu_0$ [Hz])	Activation energy E_a (eV)
1	p	B	5×10^{18}	CG	$7.3^{+4.2}_{-2.8}$	$0.9^{+0.6}_{-0.4}$
2	p	B	2×10^{15}	CG	$5.3^{+2.6}_{-1.7}$	$0.5^{+0.3}_{-0.2}$
3	p	B	$\leq 10^{13}$	FZ	$5.6^{+3.5}_{-2.0}$	$0.5^{+0.4}_{-0.2}$
4	n	P	$\leq 10^{13}$	FZ	$6.5^{+5.5}_{-2.5}$	$0.6^{+0.6}_{-0.3}$
5	n	P	9×10^{14}	FZ	$3.3^{+1.5}_{-2.3}$	0.23 ± 0.15
6	n	Sb	1.5×10^{18}	CG	4.1 ± 1.8	0.23 ± 0.15

CG=Crucible Grown, FZ=Float Zone

(4) From these results, they suggested that the nonsubstitutional B is identified with the defect of the $B^{(+)}$ which was found previously by ESR study, because the deduced activation energy of the nonsubstitutional B agrees with that of the $B^{(+)}$ found by ESR for the same doping level.

(5) They found quadrupole split resonance in the NMR spectra for p-type Si at 320 K. It shows $\langle 111 \rangle$ axial symmetry with the coupling constant $|eqQ/h|$ of 360 kHz. They demonstrated that the ^{12}B in this site thermally migrate between the four identical sites which correspond to the four $\langle 111 \rangle$ axis of the crystal. This fact also agrees with the case of the $B^{(+)}$ found by ESR which was supposed to be $\langle 111 \rangle$ axial symmetry and shows the same thermal behavior.

(6) The fraction of ^{12}B in this site with quadrupole split also depends on the temperature. The resonance disappears as temperature increases. The temperature dependence

slightly depends on the type and the density of dopants. For a heavily doped p-type Si, the resonance remains up until higher temperature than for the n-type Si (Fig.1.8). They performed the same measurement using the Schottky diode made of n-type Si, in order to observe the effect of the Fermi level. When a reverse bias was applied to it at $T = 340$ K so as to move the Fermi level, the quadrupole split resonance, which was not observed in the n-type Si was observed. However, the details are not clarified yet.

As described above, the location of the implanted B is still ambiguous except for the substitutional site. Besides, even among β-NMR studies the fraction of the substitutional sites at room temperature are inconsistent with each measurement (Table 1.4).

As previously stated, the purpose of this study is to confirm the fractions of the B located in each site definitely as a function of temperature, and the property and behavior of the B atom in the $\langle 111 \rangle$ axial-symmetry site, which cannot be clarified by the ESR method.

Table 1.4 The fractions of the substitutional B implanted into Si at room temperature (~300 K).

Method	Substitutional fraction (%)	Dopant	Dose	Reference
Channeling	63	1–100 Ω cm n-, & p- type	1.1×10^{14} /cm^2	[FBLS70]
β-NMR	67± 6	130 Ω cm	10×10^{10} /cm^2	[MM76]
β-NMR	~50	—	$< 10 \times 10^{5}$ /cm^2 /s	[MNDA83]
β-NMR	20 ~ 30	various	$< 10 \times 10^{5}$ /cm^2 /s	[MSS$^+$90a]

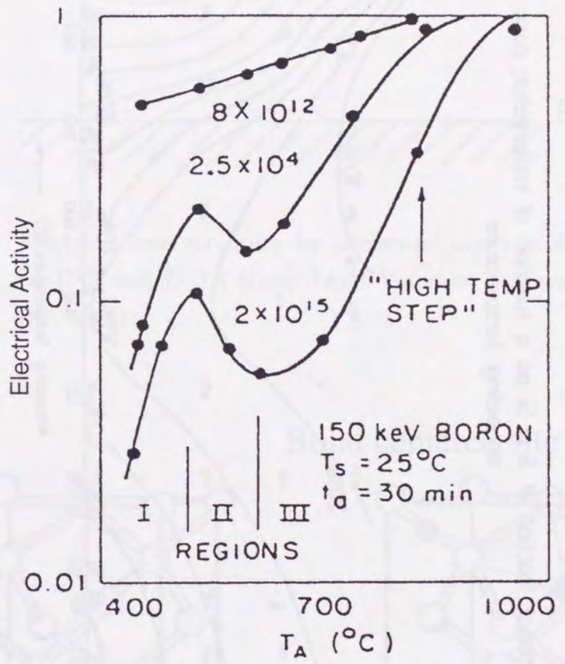

Figure 1.1 Effect of dose on the electrical activity to prove the fraction of ion implanted boron in substitutional site during annealing T_A. (after [NG71])

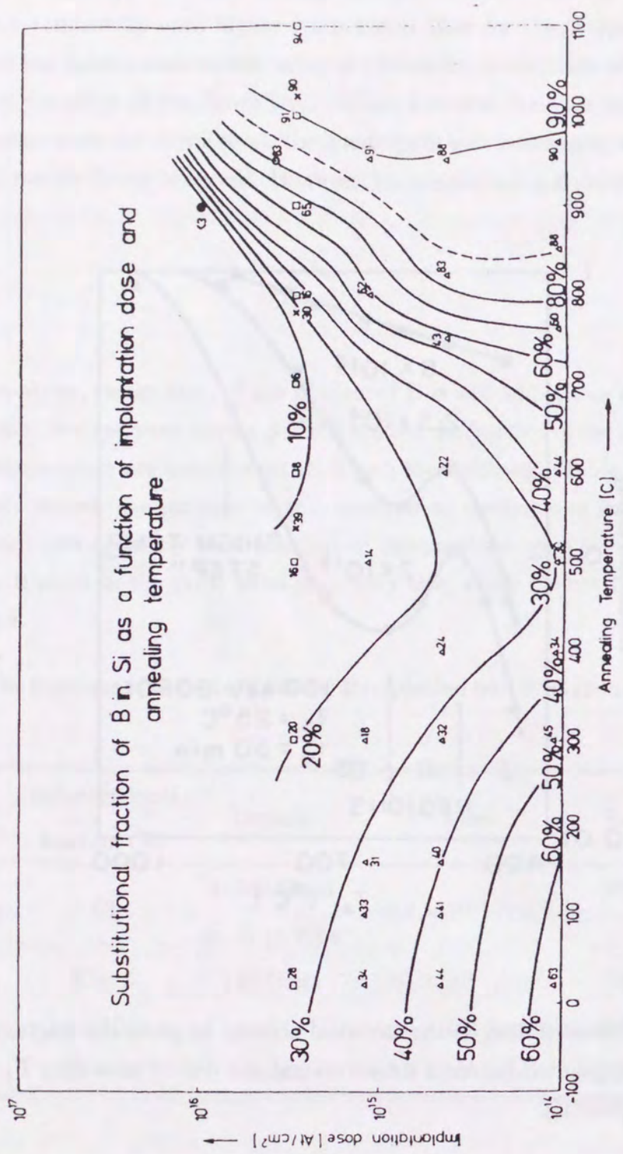

Figure 1.2 The substitutional fraction of boron in silicon in the region of maximum concentration as a function of implantation dose and annealing temperature. •··· [AH73], ×··· [SJF78], ○··· [SB73], △··· [FBLS70], □··· [NG70]. The numbers at each point indicates the measured substitutional fractions, corresponding to the maximum of the implanted B concentration profiles. Contour lines are drawn to guide the eye. (after [F+83])

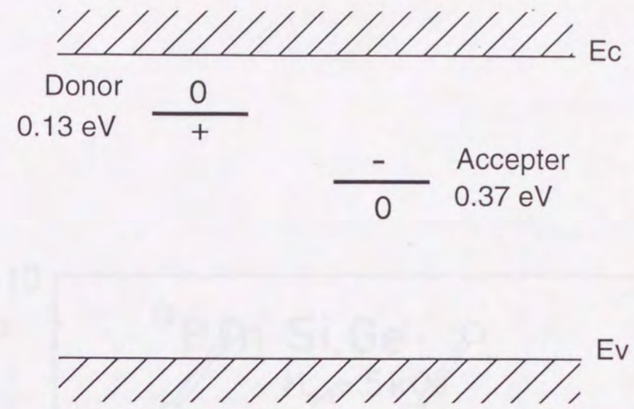

Figure 1.3 Electrical level structure for interstitial boron in silicon observed by ESR and DLTS (Deep Level Transient Spectroscopy). (after [HNW87])

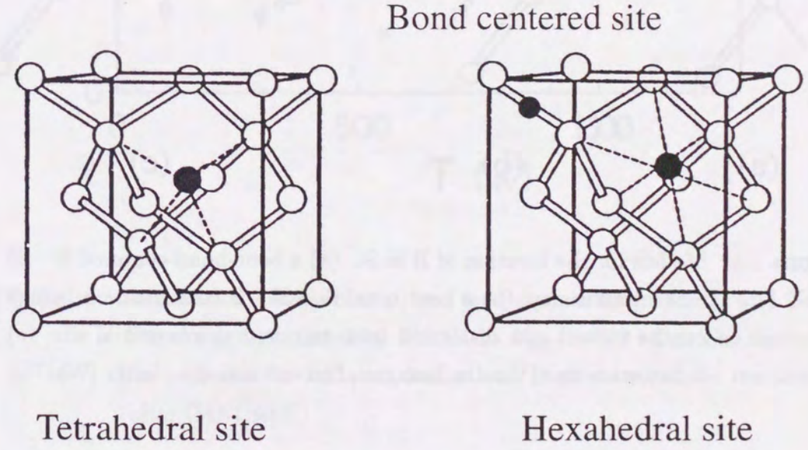

Figure 1.4 Three naive pictures on the possible interstitial sites of B implanted in diamond lattice. All these three sites have high symmetry. However, as for B atom in Si, neither by the channeling nor by the ESR study they could observe the B atom at these sites.

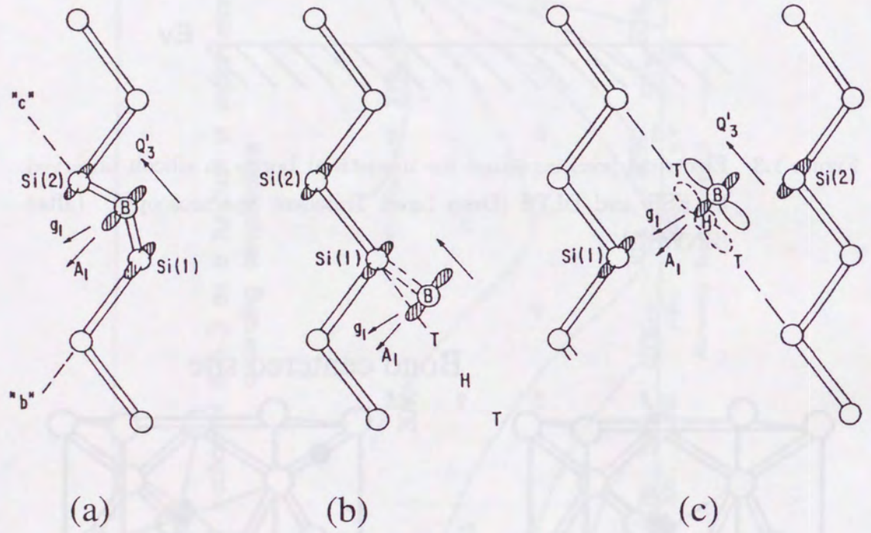

Figure 1.5 Models for the location of B in Si. (a) a bent-bond-centered Si – B – Si interstitialcy; (b) a bent-bond Si – Si – B configuration, which can be viewed as a distortion from tetrahedral interstitial site; (c) a distortion from the the hexagonal interstitial site. (after [Wat75])

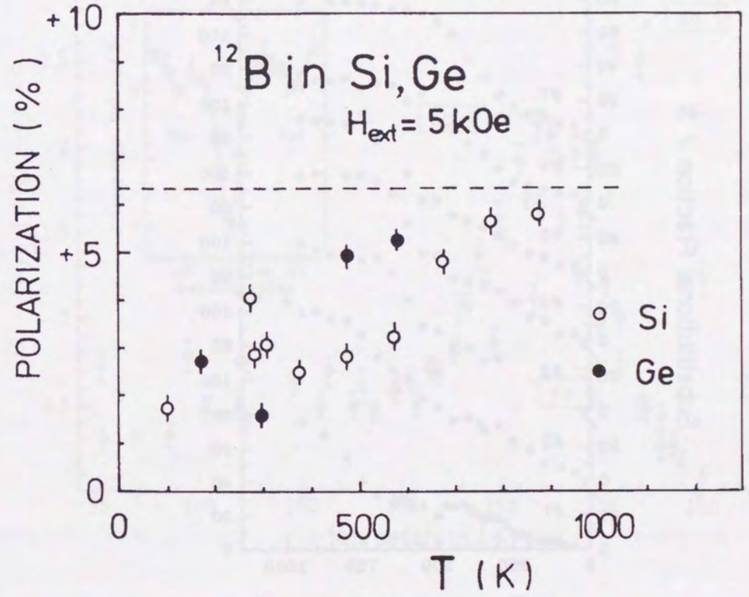

Figure 1.6 Polarization observed at ν_L vs. temperature for ^{12}B in Si and Ge. The rf was modulated by 20 kHz at $H_{\text{ext}} = 5.0$ kOe. The dashed line indicates the full polarization of ^{12}B produced in the reaction. (after [MNDA83])

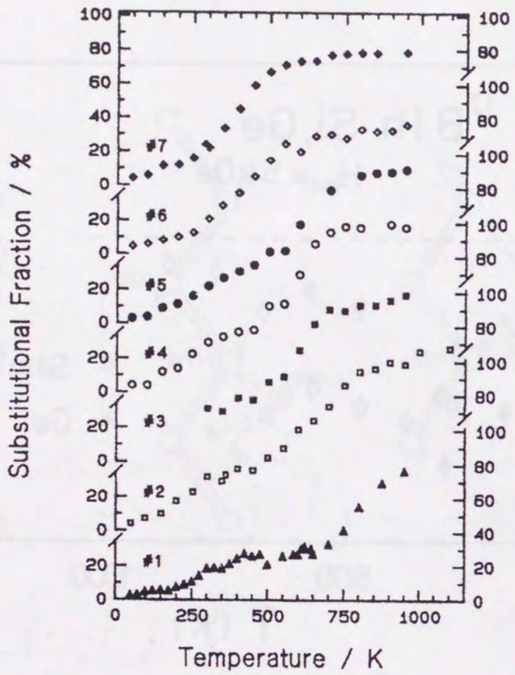

Figure 1.7 β-NMR measurements of the substitutional fraction f_s versus T of ^{12}B implanted in differently doped Si samples. Nos.1–3 are p-type, nos.4–7 are n-type with dopant concentration in cm^{-3}: 5×10^{18} B (1), 2×10^{15} B (2), $\leq 10^{13}$ B (3), $\leq 10^{13}$ P (4), 9×10^{14} P (5), 1.5×10^{18} Sb (6), 3×10^{18} P (7). (after [FSF+93])

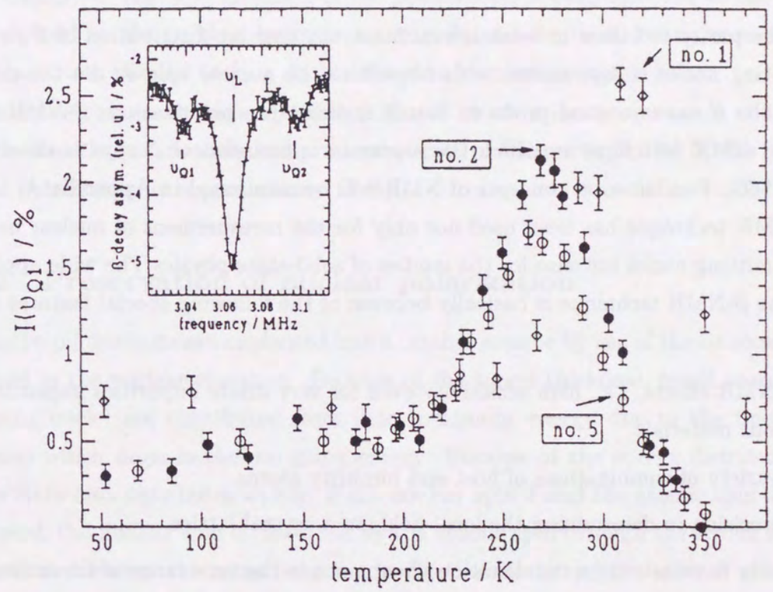

Figure 1.8 β-NMR signal intensities of the quadrupole shifted resonance $I(\nu_{Q1})$ corresponding to B_i^+ as function of temperature for three differently doped samples: no.1: Si:B (c=5×10^{18} /cm^3), no.2: Si:B (c=2×10^{15} /cm^3), no.5: Si:P (c=9×10^{14} /cm^3). The inset shows a β-NMR spectrum for sample no.5 at T=240 K, B=400.6 mT, $\angle$(B, [001])=6.5°. (after [FDE+94])

Chapter 2

Experimental methods

Due to the parity violation in weak interactions, the angular distribution of β rays from β emitting nuclei is asymmetric with respect to the nuclear spin I. So the distribution of the β ray is a good probe to detect nuclear spin polarization: β-NMR is the advanced NMR technique in which the asymmetric emission of β rays is detected [Con59, S$^+$66]. Fundamental concepts of NMR will be mentioned in Appendix A.

The β-NMR technique has been used not only for the measurement of nuclear moments of β emitting nuclei but also for the studies of solid-state physics.The wide applicability of the β-NMR technique is basically because of the following special features of the technique.

- Large NMR effects, *i.e.*, high sensitivity even for very dilute impurities implanted in various materials.
- Wide variety of combinations of host and impurity atoms.
- High precision in determining the local fields in a crystal lattice.
- Simplicity in measuring spin relaxation phenomena in the time range of the nuclear lifetime.

Because of its high sensitivity (typically below 10^9 nuclei are sufficient), this method has an advantage in investigating the hyperfine interactions of very dilute impurities like a dopant in semiconductors.

The technique consists of the following 4 procedures:

(1) Production of the polarized β-emitting nuclei through nuclear reaction.

(2) Implantation of the β emitters into materials to preserve polarization produced in the reaction.

(3) Detection of the polarization by means of β-ray asymmetry.

(4) Resonant destruction or inversion of the spin polarization by NMR.

In this chapter, principle of the β-NMR technique are described. Experimental apparatus and setup, including sample treatment will be described in the next chapter.

2.1 β-NMR technique

2.1.1 Production of polarized nuclei

In the present experiment, hyperfine interactions of ^{12}B implanted Si crystal have been studied. ^{12}B nuclei are produced through ^{11}B(d,p)^{12}B reaction ($Q = 1.149$ MeV). A large polarization is obtained in the product nuclei by selecting recoil angle and incident beam energy [T$^+$76]. The direction of the polarization is perpendicular to the reaction plane defined by the incident beam momentum $\boldsymbol{k}_i$ and the recoil beam momentum $\boldsymbol{k}_f$; the polarization parallel to $\boldsymbol{k}_i \times \boldsymbol{k}_f$ is defined to be positive in this issue.

We chose the recoil angle of $40° \pm 2.5°$ and incident deuteron energy of 1.5 MeV, to optimized the polarization and production rate of ^{12}B nuclei [T$^+$76].In this condition typical polarization is approximately 11 %.

2.1.2 Preservation of nuclear polarization

The recoil products are implanted into a catcher sample by use of the its recoil energy obtained in the nuclear reactions. Because of the target thickness, recoil energy of the out-going nuclei are distributed from 0 to maximum energy due to the finite target thickness which degrade the out-going energy. Because of the energy distribution, the charge state also distributes widely. If the nuclear spin I and the atomic spin J are not decoupled, the nuclear spin is disturbed by the atomic spin through the strong hyperfine interactions between the spins resulting in the destruction of the nuclear polarization produced in the reaction. To decouple the interaction between the nuclear spin and the atomic spin during flight in vacuum, a strong magnetic field was applied in the region from the reaction target to the implantation medium.

2.1.3 Detection of polarization

The polarization of the β emitters are observed from asymmetric distribution of β rays. The angular distribution of β rays from polarized β emitters is given as

$$W(\theta) = 1 + \frac{v}{c} AP\cos(\theta), \tag{2.1}$$

where θ is the polar angle of the electron momentum relative to the polarization axis, v is the velocity of the electron, c is the light velocity, A is the asymmetry parameter of the β decay, and P is the polarization of β emitting nuclei.

In the present case ($^{12}\mathrm{B}(1^+) \rightarrow {}^{12}\mathrm{C}(0^+)$), $v/c \approx 1$, and $A = -1$, so the equation 2.1 can be simply written as

$$W(\theta) = 1 - P\cos(\theta). \tag{2.2}$$

For an efficient measurement of the spin polarization, β-ray counters were placed at $\theta = 0°$ (up counter) and $\theta = 180°$ (down counter). The ratio R_{off} between the counting rate of the up counter (N_u) and that of the down counter (N_d) is thus given as

$$\begin{aligned} R_{\mathrm{off}} &= \frac{N_u}{N_d} = \frac{nG_uW(0°)}{nG_dW(180°)} \\ &= \frac{G_u(1-P)}{G_d(1+P)}, \end{aligned} \tag{2.3}$$

where n is the β-decay rate and G_u and G_d are the geometrical efficiencies for the up and down counters, respectively.

2.1.4 NMR detection

When an rf magnetic field is applied to the sample perpendicular to the external magnetic field, the polarization is changed diminished to P - ΔP depending on the rf frequency ν and intensity H_1. The ratio of the count rates then becomes

$$R(\nu, H_1) = \frac{G_u[1-(P-\Delta P(\nu, H_1))]}{G_d[1+(P-\Delta P(\nu, H_1))]}. \tag{2.4}$$

Normalized by the ratio R_{off}, the geometrical asymmetries are canceled out, and when $P(P-\Delta P) \ll 1$, the polarization change $\Delta P(\nu, H_1)$ is deduced as

$$\Delta P(\nu, H_1) = \frac{[R(\nu, H_1)/R_{\mathrm{off}}] - 1}{[R(\nu, H_1)/R_{\mathrm{off}}] + 1} \tag{2.5}$$

Time sequence of β NMR detection

In the present experiment, the pulsed beam method (next section) was employed to separate the counting period from the beam-on period to reject unwanted background. The rf was applied right after the beam-on period. Typical timing program was as shown in Fig.2.1 with schematics to explain β-ray yield and the nuclear spin polarization.

The time development of the polarization $P(t)$ and the number of nuclei $N(t)$ should hold the following differential equations;

$$\frac{d}{dt}P(t) = \frac{q}{N(t)}P_0 - (\Lambda + \lambda + W)P(t), \tag{2.6}$$

$$\frac{d}{dt}N(t) = q - \lambda N(t). \tag{2.7}$$

Here, the meaning of the parameters are as follows.

- P_0: Initial polarization
- q: Implantation (production) rate of the nuclei ($q = 0$, except for beam-on period)
- Λ: Spin-lattice relaxation rate: reciprocal of the spin-lattice relaxation time T_1
- λ: Decay-rate: reciprocal of the mean life of the nucleus τ_β (29.1ms: for ^{12}B)
- W: Transition probability between magnetic substates by the destructive rf field.

The transition probability W for $I = 1$ nucleus is

$$W = \frac{1}{2}(\gamma H_1)^2 f(\nu), \quad \text{for single quantum transition } \Delta m_I = \pm 1, \tag{2.8}$$

where $f(\nu)$ is the intrinsic line shape function.

Under the timing program shown in Fig.2.1, the polarization in the counting time is given as a function of time as

$$P(t) = P_0 \frac{\lambda}{\Lambda + \lambda + W} \frac{1 - \mathrm{e}^{-(\Lambda+\lambda+W)t_1}}{1 - \mathrm{e}^{-\lambda t_1}} \mathrm{e}^{-\Lambda(t_2+t)}, \tag{2.9}$$

where t_1 and t_2 are the beam bombarding time and the rf time, respectively.

2.2 β-NQR method

If the nuclear quadrupole moment Q of a nucleus ($I \geq 1$) is not zero, the host atoms interact with electric field gradient q from the surrounding host atoms(Appendix A). Under the electric quadrupole interaction added to the magnetic interaction, the resonance frequency shifts from the Larmor frequency ν_L, and the resonance line splits into $2I$ resonance frequencies. Because only a pair of neighboring sublevels is involved in a single transition, the NMR signal becomes weaker than the case of pure magnetic interaction (Fig.2.2). To observe NMR in good efficiency even in this case, we employed a modified β-NMR method, so called β-NQR method [M$^+$92].

When the electric quadrupole interaction is much smaller than the magnetic interaction, it can be treated as a perturbation. In the first- and second-order perturbation theory, the transition frequency between substate m and m-1 is given (Appendix A) as

$$\nu_m = \frac{E_{m-1} - E_m}{h} = \nu_L + \nu_m^{(1)} + \nu_m^{(2)} + \cdot \quad (m = I, I-1 \ldots I+1), \tag{2.10}$$

$$\nu_m^{(1)} = -\frac{1}{2}\nu_Q(m - \frac{1}{2})(3\cos^2\theta - 1 + \eta\cos 2\phi \sin^2\theta), \tag{2.11}$$

For the given Larmor frequency ν_L, the crystal orientation θ, ϕ and the asymmetry parameter of the field gradient η, a set of transition frequencies can be calculated. In the

present β-NQR method, simultaneous application of $2I$-rf's corresponding to the correct coupling frequencies given above induce all the transitions and destroys polarization completely, as a schematically shown in Fig.2.3, in the case of ^{12}B (I=1).

Considering pure polarization, that is, initial substate populations are distributed linearly ($a_m = \alpha m + \beta$) and each transition is saturated by rf's, we will obtain full polarization, *i.e.*, $P_0 = \alpha(I+1)(2I+1)/3$. On the other hand, in conventional β NMR, *i.e.* when a pair of substate populations are equalized, the obtained polarization change is reduced to $\alpha/2$. So that, $2(I+1)(2I+1)/3$ times larger polarization change is expected by the present β-NQR method. Thus, this technique help NMR measurement effective especially for large spin I. For the nuclei with $I = 1$ like ^{12}B the enhancement factor is already 4. This means 32 ($= 4^2 \times (2I)$) times more effective than the conventional NMR.

2.3 Relaxation mechanisms of nuclear polarization

2.3.1 General

The nuclear polarization produced through nuclear reaction decreases as a function of time toward the value in the thermal equilibrium which is practically zero compared with the preset nuclear polarization. The motion of the polarization is described phenomenologically by the Bloch equations using the spin-lattice relaxation time T_1 and the spin–spin relaxation time T_2 as

$$\frac{d\langle I_z\rangle}{dt} = -\frac{\langle I_z\rangle - I_{z0}}{T_1}, \tag{2.12}$$

$$\frac{d\langle I_x\rangle}{dt} = \gamma(\langle \boldsymbol{I}\rangle \times \boldsymbol{H})_x - \frac{\langle I_x\rangle}{T_2}, \tag{2.13}$$

$$\frac{d\langle I_y\rangle}{dt} = \gamma(\langle \boldsymbol{I}\rangle \times \boldsymbol{H})_y - \frac{\langle I_y\rangle}{T_2}. \tag{2.14}$$

T_1 represents the rate of the relaxation of the polarization $\langle I_z\rangle$ toward the thermal equilibrium value I_{z0}, caused by contact with the lattice as a thermal reservoir. T_2 is the characteristic time for the dephasing process of the spin ensemble.

Here, we concentrate on T_1. There are two essential causes for the relaxation. One is due to a fluctuating local fields at the nucleus, and the other is due to spin-flip scattering with electrons known as the Fermi contact interaction. In order to explain the experimental results quantitatively, we will describe these relaxation mechanism in this section.

2.3.2 Spin–lattice relaxation by the motion of the atom

A nucleus in matter interacts with the internal local fields, such as the magnetic field and the electric field gradient, produced by the neighboring atoms as well as with the external fields. The local field varies according to the lattice site of the atom, because the local field depends on the geometrical configuration around the nucleus. Therefore, when the atom jumps from a lattice site to the other, the nucleus experiences a time-varying local field. It can cause the polarization relaxation. The mean residence time $\bar{\tau}$ of an atom, which is an average of the time bin that an atom stays at a lattice site, can be described by the Arrhenius formula,

$$\frac{1}{\bar{\tau}} = \frac{1}{\tau_0}\exp\left(-\frac{E_a}{kT}\right), \tag{2.15}$$

where τ_0 is the mean residence time at infinite temperature, E_a is the activation energy for a jump. Each jump usually obeys the Poisson process with the mean occurrence of $1/\bar{\tau}$, and then the distribution of the residence time τ is expressed by a simple exponential

$$P(\tau) = P_0\exp\left(-\frac{|\tau|}{\bar{\tau}}\right). \tag{2.16}$$

Therefore, the distribution of the jump frequency is obtained by Fourier transformation of $P(\tau)$

$$\begin{aligned} P(\omega) &= \frac{1}{2\pi}\int_{-\infty}^{\infty} P(\tau)\, e^{-i\omega\tau} d\tau \\ &= \frac{2P_0}{\pi}\frac{\bar{\tau}}{1+\omega^2\bar{\tau}^2}. \end{aligned} \tag{2.17}$$

As shown in Fig.2.4, when the frequency distribution has a component at the Larmor frequency ω_L (for the case of spin $I = 1/2$), it causes the polarization relaxation. Thus, the quantity $P(\omega_L)$ is proportional to the transition rate and hence the relaxation rate

$$\frac{1}{T_1} \propto \frac{\bar{\tau}}{1+\omega_L^2\bar{\tau}^2}. \tag{2.18}$$

The characteristic time for the changes of the local field is, in fact, the correlation time τ_c of the Hamiltonian of a system, which tells how long the Hamiltonian at a certain moment is correlated to a later value, which is, within a factor of order unity, the same as the mean residence time $\bar{\tau}$ described above. Fig.2.5 shows the relaxation rate $1/T_1$ as a function of the correlation time. According to eq.(2.18), it is shown that for $\tau_c \ll 1/\omega_L$, the $1/T_1$ is proportional to τ_c; for $\tau_c \gg 1/\omega_L$, $1/T_1$ is proportional to $1/\tau_c$. That is, the relaxation rate $1/T_1$ is strongest at $\tau_c = 1/\omega_L$. Therefore, under assumption of the Arrhenius behavior, the relaxation time becomes shorter as increasing temperature till it

reaches minimum at a certain temperature, and then becomes longer as the temperature. Thus, the relaxation time can be seriously short only in a certain temperature range.

Now a quantitative formula will be given to the above described qualitative discussion on the relaxation of the nuclear polarization (mainly following after Ref. [Abr63, Sli90]). This will be important formula for the later analysis. Since the nuclear polarization is a statistical physical quantity of spin ensemble, the motion of polarization is described using a density matrix ρ of the system in the quantum mechanics treatment. The statistical average $\langle Q \rangle$ of any observable Q can is expressed as follows, when the density matrix of the spin system is given.

$$\langle Q \rangle = \mathrm{Tr}\left\{\rho Q\right\}. \tag{2.19}$$

So, the motion of $\langle Q \rangle$ can be described as

$$\frac{\mathrm{d}}{\mathrm{d}t}\langle Q \rangle = Tr\left\{\left(\frac{\mathrm{d}\rho}{\mathrm{d}t}\right)\cdot Q\right\}. \tag{2.20}$$

Therefore, we know the motion of $\langle Q \rangle$ by solving the equation of motion for the density matrix ρ,

$$\frac{1}{i}\frac{\mathrm{d}\rho}{\mathrm{d}t} = -\left[\mathrm{H}, \rho\right]. \tag{2.21}$$

When the Hamiltonian is separated into two parts,*i.e.*, $\mathrm{H}(t) = \mathrm{H}_0 + \mathrm{H}_1(t)$, the sum of a large static component H_0 and a small time-dependent component H_1, where the H_0 commutates with Q, the equation of motion can be written in the interaction representation as

$$\frac{\mathrm{d}}{\mathrm{d}t}\langle Q \rangle = \mathrm{Tr}\left\{\left(\frac{\mathrm{d}\rho^*}{\mathrm{d}t}\right)\cdot Q\right\}, \tag{2.22}$$

$$\frac{1}{i}\frac{\mathrm{d}\rho^*}{\mathrm{d}t} = -\left[\mathrm{H}_1^*(t), \rho^*\right], \tag{2.23}$$

where $\mathrm{H}_1^*(t)$ and $\rho^*(t)$ are defined by,

$$\mathrm{H}_1^*(t) = \exp(i\mathrm{H}_0 t/\hbar)\mathrm{H}_1 \exp(-i\mathrm{H}_0 t/\hbar), \tag{2.24}$$

$$\rho^*(t) = \exp(i\mathrm{H}_0 t/\hbar)\rho \exp(-i\mathrm{H}_0 t/\hbar). \tag{2.25}$$

Integrating eq.2.23 from $-t$ to t and making successive approximation to the second order of H_1, we obtain

$$\frac{\mathrm{d}}{\mathrm{d}t}\rho^*(t) = -\frac{1}{2\hbar^2}\int_{-t}^{t}\mathrm{d}\tau\left[\mathrm{H}_1^*(0), \left[\mathrm{H}_1^*(\tau), \rho^*(t)\right]\right]. \tag{2.26}$$

Since there are numbers of ensembles of systems of identical H_0 and ρ, the average of these ensembles should be treated as

$$\frac{\mathrm{d}}{\mathrm{d}t}\rho^*(t) = -\frac{1}{2\hbar^2}\int_{-t}^{t}\overline{\mathrm{d}\tau\left[\mathrm{H}_1^*(0), \left[\mathrm{H}_1^*(\tau), \rho^*(t)\right]\right]}. \tag{2.27}$$

For the spin polarization, $Q{=}I_z$, when the perturbation Hamiltonian is given by the product of the spin component A_q and the space-time component F_q as

$$\mathrm{H}_1(t) = \sum_q A_q F_q(t), \tag{2.28}$$

then the equation of motion is given as

$$\begin{aligned}\frac{\mathrm{d}}{\mathrm{d}t}\rho^*(t) &= -\frac{1}{2\hbar^2}\sum_{q,q'}\mathrm{e}^{i(\omega_q+\omega_{q'})t}\int_{-t}^{t}\overline{G_{q'q}(\tau)}\mathrm{e}^{i\omega_q\tau}\mathrm{d}\tau\left[A_{q'}, \left[A_q, \rho^*\right]\right], \\ &\overline{G_{q'q}(\tau)} = \overline{F_{q'}(0)F_q(\tau)}, \\ &\mathrm{H}_0 A_q = \hbar\omega_q A_q.\end{aligned} \tag{2.29}$$

Assuming that the correlation of each component suffixed by q is independent, that is $\overline{G_{q'q}(\tau)} = \delta_{-q'q}\overline{G_q(\tau)}$, the equation 2.29 can be written as

$$\frac{d}{dt}\rho^*(t) = -\frac{1}{2\hbar^2}\sum_q\int_{-t}^{t}G_q(\tau)e^{-i\omega_q\tau}d\tau\left[A_{-q}, \left[A_q, \rho^*\right]\right]. \tag{2.30}$$

Thus, by substituting (2.30) into (2.22) the equation of motion of $\langle I_z \rangle$ is obtained as

$$\frac{\mathrm{d}\langle I_z \rangle}{\mathrm{d}t} = -\frac{1}{2\hbar^2}\sum_q\int_{-\infty}^{\infty}G_q(\tau)\mathrm{e}^{-i\omega_q\tau}d\tau\mathrm{Tr}\left\{\left[A_{-q}, \left[A_q, \rho^*\right]\right]\right\}\langle I_z \rangle, \tag{2.31}$$

where the limit of integration is taken to be $\pm\infty$, so that it becomes independent of time as is in the case with $t \gg \tau_c$.

From the equation (2.31), if the correlation function $G(\tau)$ of the spin system is given, the relaxation time can be calculated. The explicit form of the correlation function depends on the detail process of the atomic jump.

2.3.3 Polarization relaxation due to the fluctuation of the electric field gradient

In this section, using the equation (2.31) the relaxation time due to the fluctuation of the local electric field gradient will be given for the analysis of the present experimental results.

Suppose the case that only the direction of the principal axis of the electric field gradient around a nucleus changes with time, with its coupling constant unchanged. The perturbation Hamiltonian is written as

$$\mathrm{H}_1 = \mathrm{H}_Q = \frac{eqQ}{4I(2I-1)} \sum_q F^q(t) A^q, \tag{2.32}$$

$$F^q(t) = \begin{cases} \sqrt{\frac{4\pi}{5}}\mathrm{Y}_2^0(\Omega(t)) & \text{for } q = 0 \\ \sqrt{\frac{6\pi}{5}}\mathrm{Y}_2^{-1}(\Omega(t)) & \text{for } q = 1 \\ -\sqrt{\frac{6\pi}{5}}\mathrm{Y}_2^{1}(\Omega(t)) & \text{for } q = -1 \\ \sqrt{\frac{6\pi}{5}}\mathrm{Y}_2^{-2}(\Omega(t)) & \text{for } q = 2 \\ \sqrt{\frac{6\pi}{5}}\mathrm{Y}_2^{2}(\Omega(t)) & \text{for } q = -2 \end{cases}, \tag{2.33}$$

$$A^q = \begin{cases} 3I_z^2 - I^2 & \text{for } q = 0 \\ I_+I_z + I_zI_+ & \text{for q= 1} \\ I_-I_z + I_zI_- & \text{for q=-1} \\ I_+^2 & \text{for q= 2} \\ I_-^2 & \text{for q=-2} \end{cases}, \tag{2.34}$$

where Y_2^q is the second-order spherical harmonics and the direction of the electric field gradient is denoted by Ω. Using eq.(2.31) we obtain

$$\frac{\mathrm{d}\langle I_z\rangle}{\mathrm{d}t} = -\frac{1}{2\hbar^2}\left\{\frac{eqQ}{4I(2I-1)}\right\}^2 \sum_q k_q(\omega_q)\mathrm{Tr}\left\{\left[A^q,\left[A^{-q},I_z\right]\right]\rho^*\right\}\langle I_z\rangle, \tag{2.35}$$

$$k_q(\omega_q) = \int_{-\infty}^{\infty} \overline{F^{-q}\left(\Omega(0)\right)F^q\left(\Omega(\tau)\right)}\, \mathrm{e}^{-i\omega_q\tau}\mathrm{d}t. \tag{2.36}$$

For the nuclei of spin I =1 as is in the case of ^{12}B, the eq.(2.35, 2.36) can be simplified as

$$\frac{1}{T_1} = \frac{1}{\langle I_z\rangle}\frac{\mathrm{d}\langle I_z\rangle}{\mathrm{d}t} = \frac{(eqQ)^2}{8\hbar}\left\{k_1(\omega_0) + 4k_2(2\omega_0)\right\}. \tag{2.37}$$

As mentioned above, the correlation function depends on a specific model of the fluctuation such as the path and frequency of the atomic jump. For example, the expression of relaxation mechanism due to fluctuation of the electric field gradient which shows entirely isotropic change such as the rotation of a molecule has been widely used in the analysis of behavior of the atoms and molecules.

Here, we assume the following model in order to deduce the correlation functions k_1 and k_2. There are four electric field gradients which are different in its directions but identical in strength. The atoms are jumping from a site to another site with the mean jumping rate $1/\tau_c$. (The time required for a jump is assumed to be much shorter than τ_c.) In this case, the correlation function between $t = 0$ and $t = \tau$ is given as

$$\overline{F^q(0)F^q(\tau)} = \frac{\alpha}{4}\left\{P_A(\tau)\sum_i \mathrm{Y}_2^q(\Omega_i)\mathrm{Y}_2^q(\Omega_i) + P_B(\tau)\sum_{i\neq j}\mathrm{Y}_2^q(\Omega_i)\mathrm{Y}_2^q(\Omega_j)\right\}, \tag{2.38}$$

where Ω_i (i=1, 2, 3, 4) are the directions of the field gradients, $P_A(\tau)$, $P_B(\tau)$ are the probabilities for an atom to be found in the same site or in the different sites after $t = \tau$, respectively. α is $4\pi/5$ for q=0 and $6\pi/5$ for q=1, 2. When the rate of the jump is $1/\tau_c$, the $P_A(\tau)$, $P_B(\tau)$ can be calculated as

$$P_A(\tau) = \frac{1}{4} + \frac{3}{4}\mathrm{e}^{-4\tau/3\tau_c} \tag{2.39}$$

$$P_B(\tau) = \frac{1}{4} - \frac{1}{4}\mathrm{e}^{-4\tau/3\tau_c} \tag{2.40}$$

$$P_A(\tau) + 3P_B(\tau) = 1$$

Then we obtain the correlation functions as

$$k_1(\omega_0) = \frac{1}{4}\frac{2\tau}{1+\omega_0^2\tau_c^2}, \tag{2.41}$$

$$k_2(2\omega_0) = \frac{5}{16}\frac{2\tau}{1+4\omega_0^2\tau_c^2}. \tag{2.42}$$

Detail of these calculations will be described in Appendix C. In conclusion, the relaxation time for this jump model is given by the equations (2.37), (2.41), and (2.42)

2.3.4 Spin–lattice relaxation due to conduction electrons

There is another important spin-lattice relaxation process due to conduction electrons. It can be explained as spin between of the nuclear spin I and the spins of conduction electrons. This process is a dominant mechanism of the relaxation in metals not in semiconductors. So, only a brief summary will be given here.

The Fermi contact interaction is proportional to the square of the electron wave function at the nucleus $|\phi(0)|^2$. Then transition probability is obtained as

$$\frac{1}{T_1} = \frac{(4\pi)^3}{9}\gamma_n^2\gamma_e^2\hbar^3\,|\phi(0)|^4\,D(E_F)^2k_BT, \tag{2.43}$$

where $D(E_F)$ is the density of state at the Fermi surface.

Since the frequency shift K (the Knight shift) in a magnetic field due to the paramagnetism of the conduction electrons for Fermi gas is also proportional to $|\phi(0)|^2 D(E_F)$, that is

$$K \equiv \frac{\Delta H}{H} = \frac{4\pi}{3}\gamma_e^2\hbar^2 |\phi(0)|^2 D(E_F), \tag{2.44}$$

so the relaxation time and the Knight shift have the relation known as the Korringa relation,

$$K^2 T_1 T = \frac{\hbar}{4\pi k_B}\left(\frac{\gamma_e}{\gamma_n}\right)^2. \tag{2.45}$$

Although this formula gives only a contribution from the s-state electron, it is still useful to predict spin-lattice relaxation time.

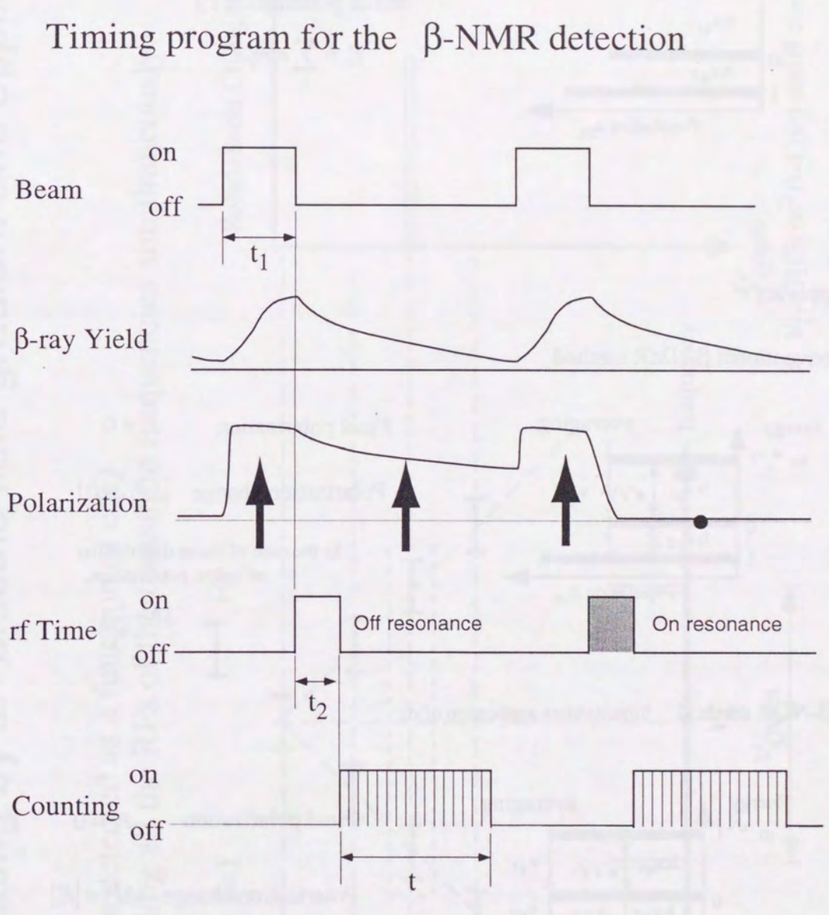

Figure 2.1 Typical timing program for the β-NMR detection.

Initial polarization and energy levels.
For nuclear spin I

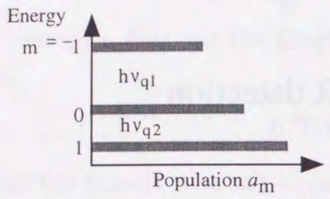

Initial polarization P_0

$$P_0 = \sum_i a_i m_i$$

After applying rf

1) Conventional β-NMR method

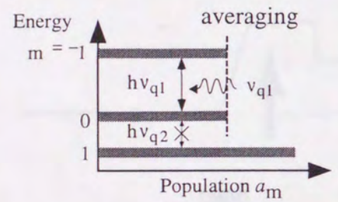

Final polarization $P_1 \neq 0$

Polarization change $|\Delta P| < |P_0|$

In the case of linear distribution of initial populations,

$$\Delta P = \frac{1}{4} P_0$$

2) β-NQR method Simultanious application of rfs

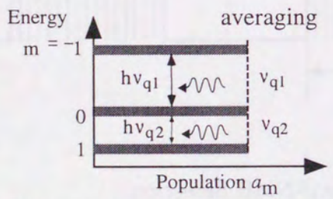

Final polarization $P_2 = 0$

Polarization change $|\Delta P| = |P_0|$

Figure 2.2 Partial and complete depolarizations. Single rf can induce just one of two transitions. The polarization change due to partial depolarization is only 1/4 of that in the case of complete depolarization.

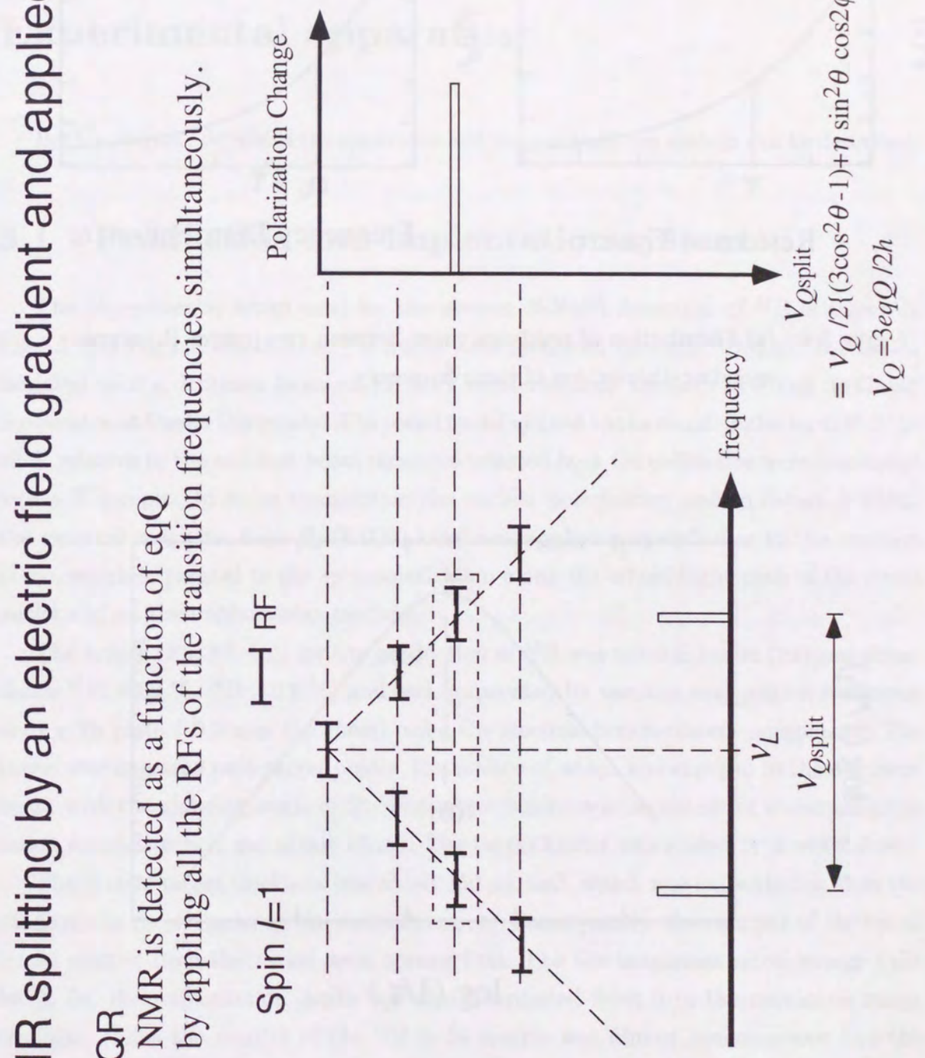

Figure 2.3 Principle of the β-NQR method. The spectrum is measured as a function of the quadrupole coupling constant.

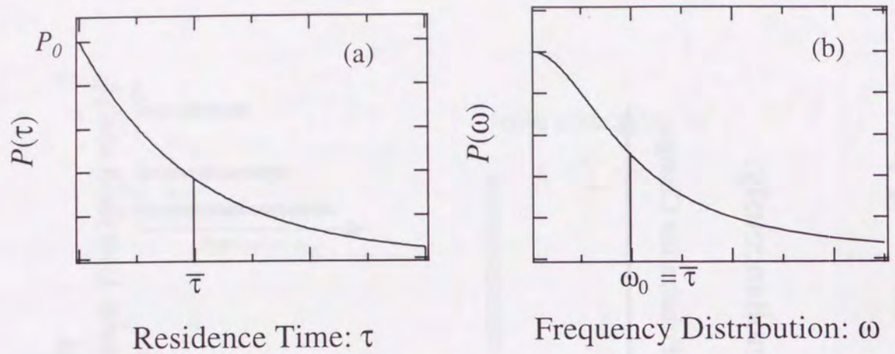

Figure 2.4 (a) Distribution of residence times between two jumps, (b) corresponding distribution of jump frequency.

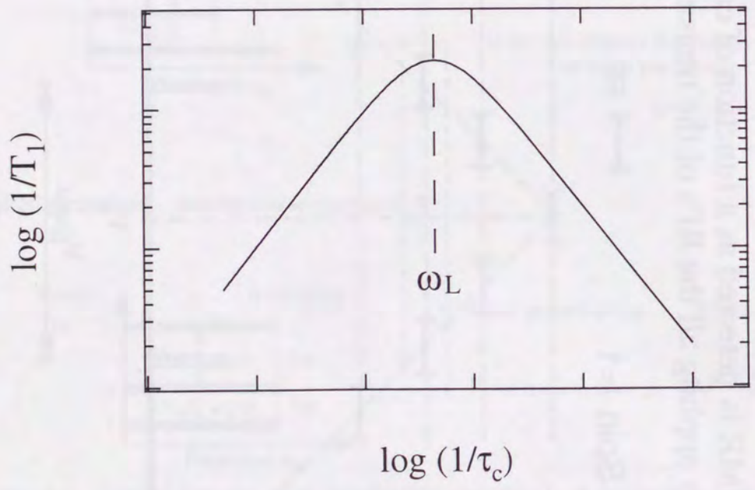

Figure 2.5 The relationship between relaxation rate $1/T_1$ and reciprocal of the correlation time τ_c. The $1/T_1$ shows a peak at $1/\tau_c=\omega_L$.

Chapter 3

Experimental apparatus

In this chapter, details of the apparatus and data-acquisition system will be described.

3.1 Production and implantation system

The experimental setup used for the present β-NMR detection of ^{12}B is shown in Fig.3.1 and Fig.3.2. Short-lived ^{12}B nuclei were produced through ^{11}B(d,p)^{12}B reaction initiated with a deuteron beam of 1.5 MeV accelerated by the 4.75 MV Van de Graaff accelerator at Osaka University. The recoil nuclei ejected to the recoil angles form 37.5° to 42.5° relative to the incident beam direction selected by a Cu collimator were implanted into a Si sample. In order to maintain the nuclear polarization and to detect β-NMR, the external magnetic field H_0 (6.0000 kOe) was applied perpendicular to the reaction plane, which is parallel to the spin polarization along the whole flight path of the recoil nuclei and on the implantation medium.

The target (Fig.3.1–(c)) for the production of ^{12}B was natural boron (natural abundance ^{11}B: 80.2 %, ^{10}B: 19.8 %) and was evaporated by vacuum evaporation technique onto a Ta plate (0.5 mm thickness) using the electron-bombardment equipment. The target was mounted on a target holder, the surface of which was exposed to the deuteron beam with the glancing angle of 5°. The target holder was insulated for monitoring the target current, which was about 15 μA. The target holder was cooled by a water flow.

The typical target thickness was about 150 μg/cm^2, which was twice thicker than the range of the recoil nuclei in the recoil direction. Consequently, the energies of the recoil nuclei ejected from the target were spread from 0 to the maximum recoil energy (450 keV). So, the implantation depth was also distributed from 0 to the maximum range of 1 μm. Thus the density of the ^{12}B in Si sample was almost homogeneous and the corresponding dose rate was about 10^8 ion/cm^3/s (total dose for a sample was about 10^{12} ion/cm^3), which is much less than the one of the doped B in the present samples (see §3.6).

In the magnetic field, no magnetic material was placed for not to disturb the homo-

Table 3.1 Properties of the rf coil.

Turn number	6×2
Inductance	3.6 μH
Intensity at the center of the coil	2.5 Oe / A

geneity of the field. The chamber was made of copper except for β-ray windows (Al 200 μm). As a result, the inhomogeneity of the magnetic field was less than approximately 10^{-5} in the sample volume.

3.2 RF system

The rf oscillating magnetic field was applied for the detection of the NMR by an rf coil which is the square–shaped Helmholtz type as shown in Fig.3.3. It was made of Cu wire (0.5 mm–diameter). In order to insulate each turn of the coil, the Cu wire was threaded with (aluminous) ceramic tubes. The coil was fixed on a coil holder. The properties of this coil are listed in Table 3.1.

The rf control system for the NMR are shown in Fig.3.4. Two rf signals from two frequency synthesizers were mixed to generate frequency modulated rf. The one for the carrier frequency can be controlled by the supervising computer for its frequencies within 100 μs. And the other generates the frequency-modulated rf through the voltage controlled oscillator (VCO).

When an rf start pulse was sent from the PC through the parallel I/O interface, the carrier frequency data was sent simultaneously to the fast switching synthesizer. To avoid the disturbance at the transient period for the frequency switching, the rf gate signal was triggered after $\sim$300 μs delayed from the start pulse. By the rf gate pulse, the frequency modulation for the other generator was started. These two rfs were mixed to obtain a required frequency, as shown in Fig.3.5. Thus synthesized rf signal was amplified by a preamplifier, and then transmitted to a 1000-W power amplifier at the experimental hall after checked for its frequency, wave form and amplitude with a frequency counter and an oscilloscope.

The amplified rf power was fed into the LC resonance circuit (fig.3.6) so as to be supplied to the rf coil effectively. For an impedance matching, a transformer was installed at the first stage of the resonance circuit. The LC circuit was tuned by a variable vacuum

capacitor. The intensity of the rf-field, *i.e.*, the voltage applied to the coil, was monitored at the test point divided by small capacitors. The maximum intensity obtained by the present rf system was about 20 Oe at the center of the coil. Typical rf wave form is shown in Fig.3.6. As shown in the figure, the Q value at the present rf system was about 10.

3.3 β-ray counting system

β rays were detected by two sets of counter telescopes placed at 0° (up) and 180° (down) relative to the external magnetic field H_0. Each counter telescope consisted of two plastic scintillation counters; a thin 1.5 mm–thick counter (ΔE-counter) and 7 mm–thick counter (E-counter). β rays were identified by the coincidence logic of these two counters. A thin Cu plate (0.5 mm) was placed between the ΔE-counter and the E-counter in order to reject low energy β rays that came from background activities. The geometry of the counters is shown in Fig.3.7.

The counters were set outside of the chamber facing the β-ray windows. The solid angel covered by the counter system was about 0.5 steradian. In this thesis no correction for this finite solid angle was made, because it is about 3 % and does not seriously affect the results compared with statistical errors. To avoid any gain shifts of photomultiplier tubes due to the strong magnetic field, photomultiplier tubes were shielded by steel and μ-metal tubes, and were placed away from the magnet behind a steel-wall.

The present data taking system is shown in Fig.3.8. Anode pulses of the photomultiplier tube (R329-02, E934/Hamamatsu) were converted to a fast logic signal by discriminators. The threshold level was adjusted to reject low energy backgrounds and electric noises. The pulse widths were 10 ns and 20 ns for ΔE and E counters, respectively. The true signal was provided by the coincidence logic $\Delta E \cap E$. Thus obtained two logic signals were counted by a CAMAC scaler. The scaler data were transferred and stored by PCs in each bin.

Typical β-ray time spectrum is shown in Fig.3.9. It is shown that the contamination from the background activities was less than 0.5 % of the total counts.

3.4 Timing program of the experiment

In order to reject unwanted backgrounds and to see the relaxation of the nuclear polarization, the pulsed beam method was employed, *i.e.*, the counting period was separated from the beam-bombardment period. In order to make this pulsed beam method

possible, a beam chopper system was used, where the electric beam deflector was employed. All these the electric beam chopper, the rf system and the β-ray counting system was supervised by PCs. The timing program is shown in Fig.3.10(a). A beam cycle composed three periods. The durations of the beam-bombardment period, the rf-period and the counting period were 25 ms, 15 ms (typical) and approximately 40 ms, respectively. Total duration of one cycle was at least 80 ms, with which conditions the number of ^{12}B produces in the previous cycle reduced to 1/16. A set of cycles (beam / rf / counting) were repeated with changing the rf frequencies until necessary counting statistics were accumulated, in order to avoid a possible long-time fluctuation of the beam condition. The computer programs are listed in APPENDIX D

In order to destroy the polarization in an appropriate frequency range, the rf frequencies were modulated linearly 5 times in one rf period (Fig.3.10-(b)). In β-NQR measurements, a set of the rfs which correspond to the two transition frequencies between sublevels were also repeated sequentially. In β-NQR measurement, the rf period of 15 ms was needed; 1.2 ms (one modulated-rf time) + 0.3 ms (a frequency-switching time)] $\times$ 10 repetition. In the conventional β-NMR measurement, however, when modulation duration of 1.2 ms is adopted, the total duration becomes 1.2 ms $\times$ 5 repetition = 6 ms. Because it is desirable to keep the same timing program, in this case, rf-off (blank) time of 9 ms was inserted following actual rf-applying time of 6 ms to make the total rf period the same as that for β-NQR..

At the end of the rf period, the β-ray counting time was started. The counting period was divided into eight sections to observe the relaxation phenomena. By use of Eq.2.4, the polarization change for the i-th section was deduced as

$$P_i = \frac{R_i/R_{i,\mathrm{off}} - 1}{R_i/R_{i,\mathrm{off}} + 1}, \tag{3.1}$$

$$R_i = N_i(0°)/N_i(180°). \tag{3.2}$$

('off' means the rf with frequency far off (10 MHz) from the resonance frequency.)

3.5 Temperature control system

The temperature of the sample was kept constant by a temperature control system. The controlled temperature range was about 100 K to 300 K with LN_2 (liquid N_2) as a coolant, and about 300 K to 750 K without LN_2.

The diagram of this system is illustrated in Fig.3.11. A sample holder made of Mo

Table 3.2 Samples used in the present experiment.

Sample No.	Type	Dopant	Dopant density (cm^{-3})	Production process
1	p	B	3×10^{14}	FZ
2	p	B	7×10^{17}	FZ
3	n	P	6×10^{14}	FZ

was extended from a Cu-block in which a heater (30 W) was installed. The sample system was well isolated from the room temperature by two thermal shields. To keep temperature constant, the on/off control method was used; where heater was on at a certain temperature, heater was off above the temperature. Since it is not the sample but the Cu-block which shows fast response to a temperature change, a thermocouple (Chromel–Alumel of ϕ0.3 mm) was installed for temperature control on the surface of the Cu-block. The temperature of the sample was measured with another thermocouple at the end of the sample holder. Considering the temperature gradient of the sample, the stability of the control system and the accuracy of the temperature measurement, the total errors of the measured temperature was estimated to be about 1.2 K at the temperatures under 600 K and about 2.5 K at the temperatures above 600 K.

3.6 Sample preparation

Three kinds of the samples were prepared. Two of them were B doped p-type silicons with electric resistance of 40–60 Ωcm and 0.07–0.13 Ωcm. The other is P doped n-type crystal with 8–10 Ωcm. The concentrations of dopants were about 3×10^{14} B/cm^3, 7×10^{17} B/cm^3 and 6×10^{14} P/cm^3, respectively [Irv62].

The size of the samples was 17 $\times$ 17 mm cut from the Si wafers (300 μm thickness). The surface was lapped mechanically and was etched in an etchant, which is the mixture of 6 parts of HNO_3 (70 %), 1 part of HF (50%) and 2 parts of CH_3COOH (100 %) solution in volume, for mirror-like smooth surface [Syo76]. As a result of etching, the thickness of the samples became about 200 μm. Just before using, it was rinsed with dilute HF solution ($\sim$2.5 %) and pure water.

(a) Beam Transport system

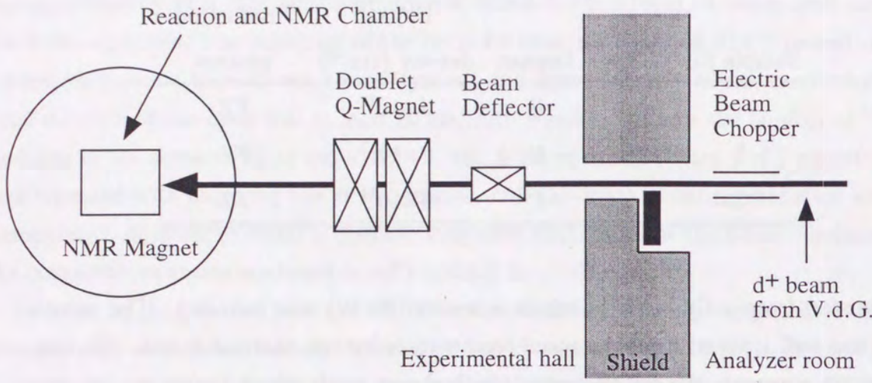

(b) Reaction and NMR Chamber

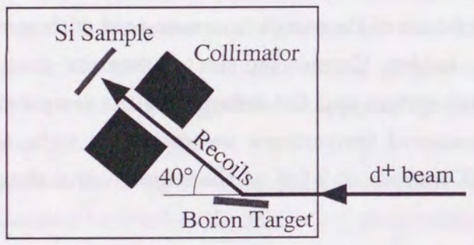

(c) Boron Target

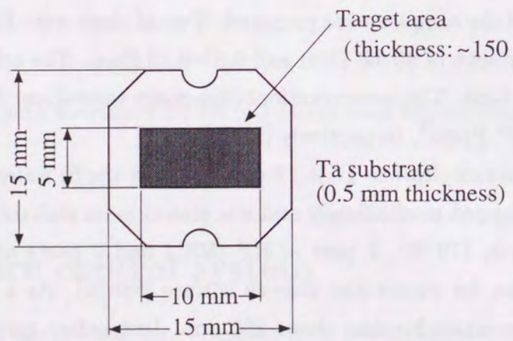

Figure 3.1 Sketches of (a) the beam transport system, (b) the recoil-angle selection, and (c) the boron target.

Overview of the β-NMR chamber

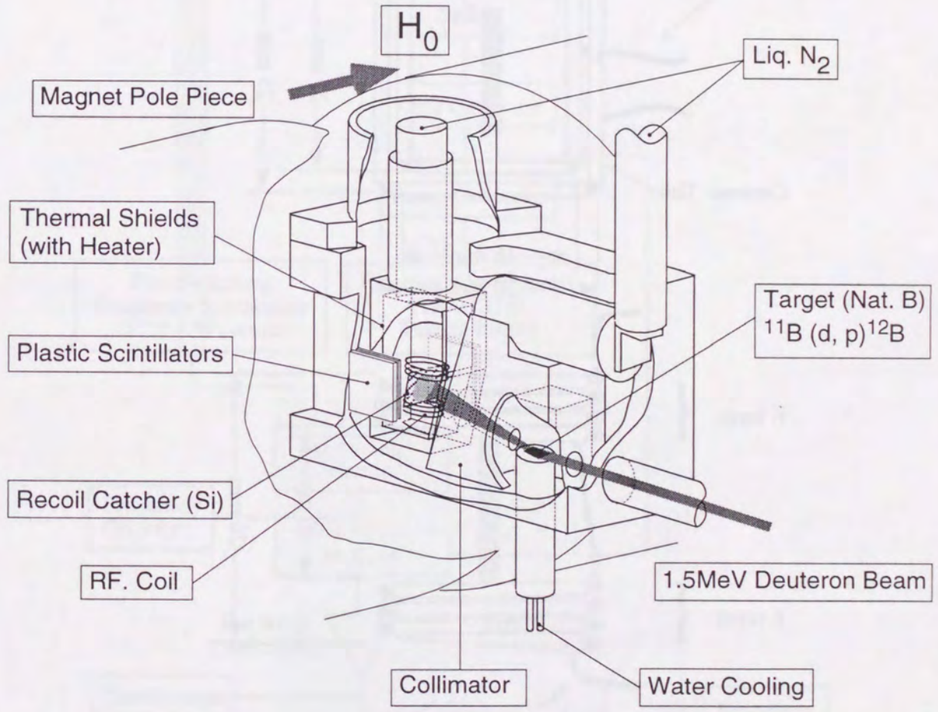

Figure 3.2 The overview of the β-NMR chamber.
The target was bombarded by the 1.5 MeV d^+ beam. The polarized nuclei obtained by selecting its recoil angle were implanted into the sample of Si. Their spins were manipulated by rf-fields. The β-rays were detected by the scintillation counters.

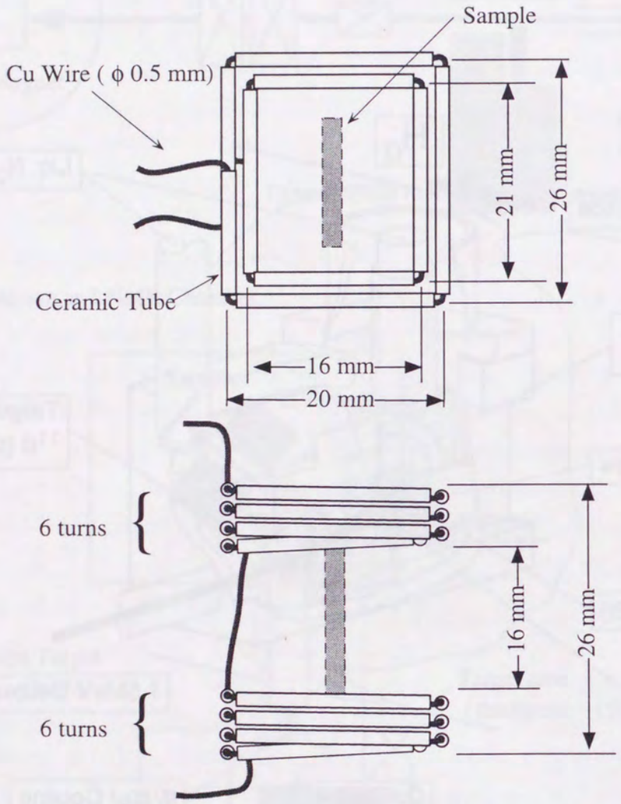

Figure 3.3 Sizes of the rf coil.

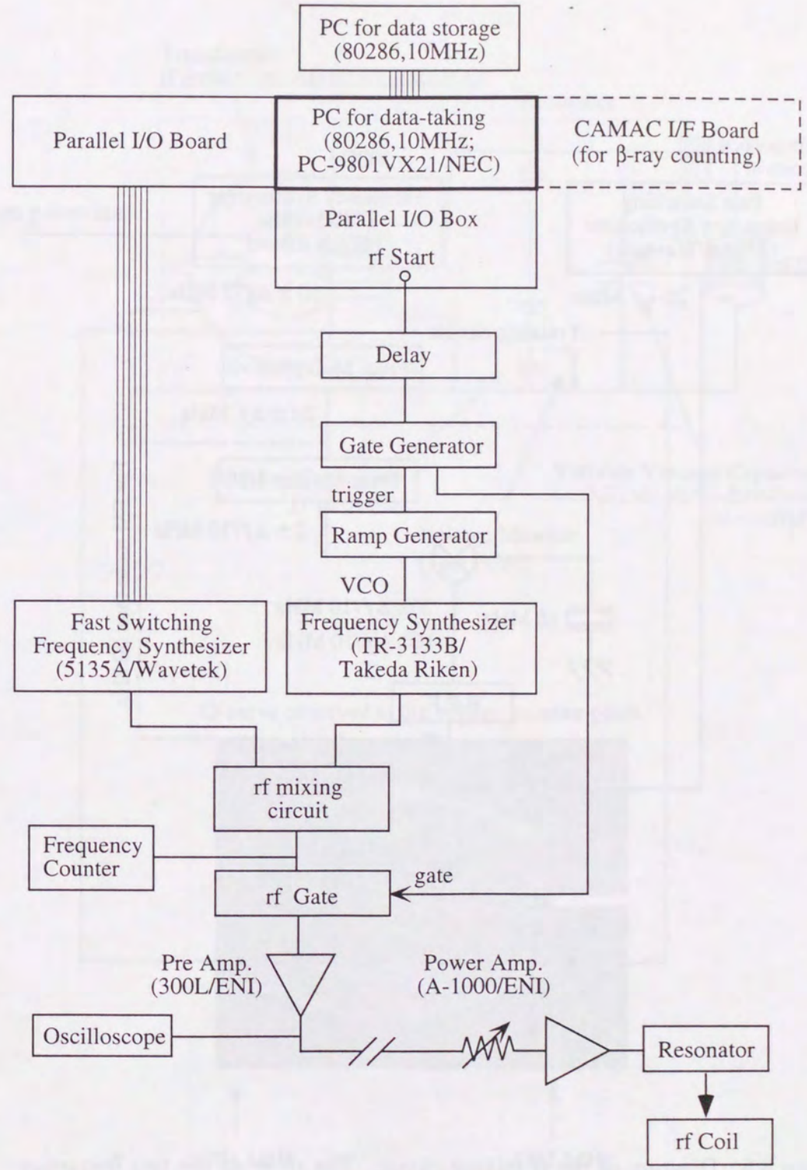

Figure 3.4 Block diagram of the rf control system. The frequency and the timing of the pulses was controlled by the PC. The electric circuits of 'rf mixing circuit' and 'resonator' are shown in Fig.3.5 and Fig.3.6, respectively.

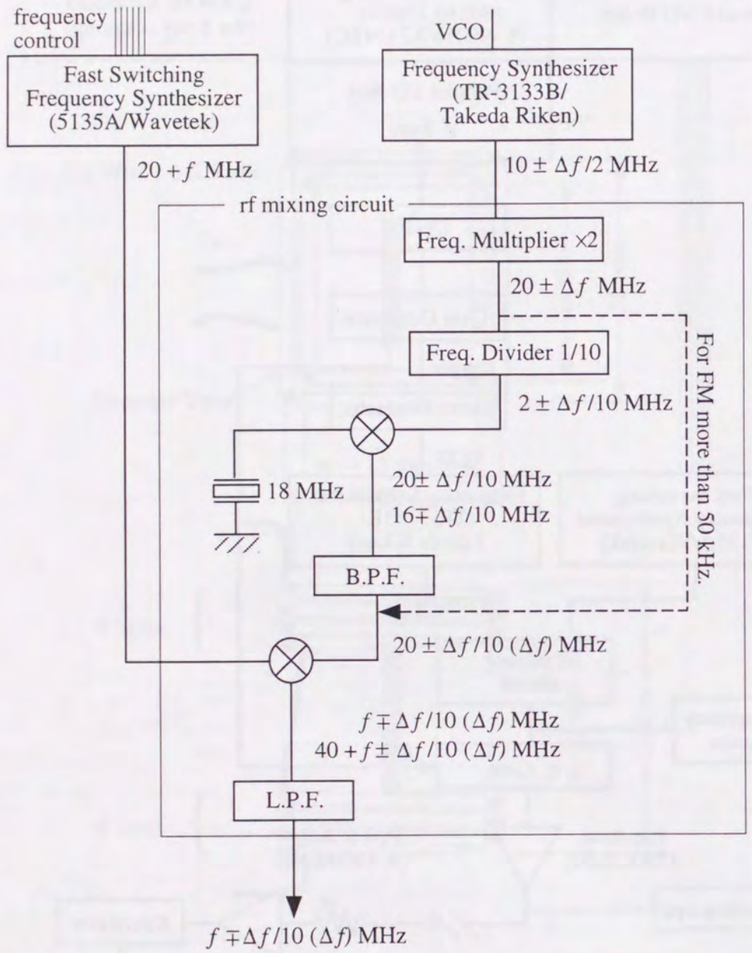

Figure 3.5 Diagram of the rf mixing circuit. The rfs from the two frequency synthesizers are mixed and filtered.

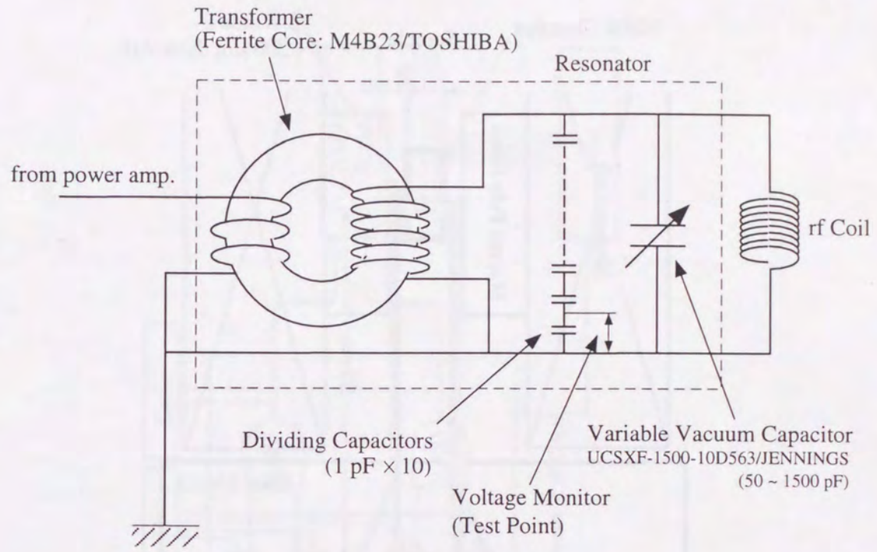

Q-curve observed at the voltage monitor point.

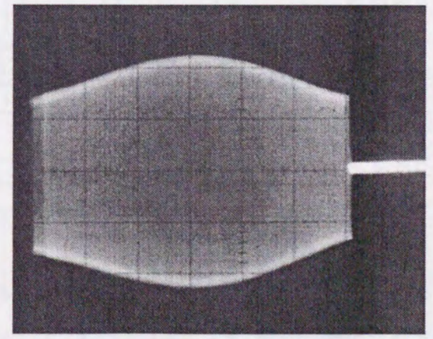

Figure 3.6 Resonator–parallel LC resonance circuit and a Q-curve of this resonance circuit.

(a) Geometrical arrangement of the detectors

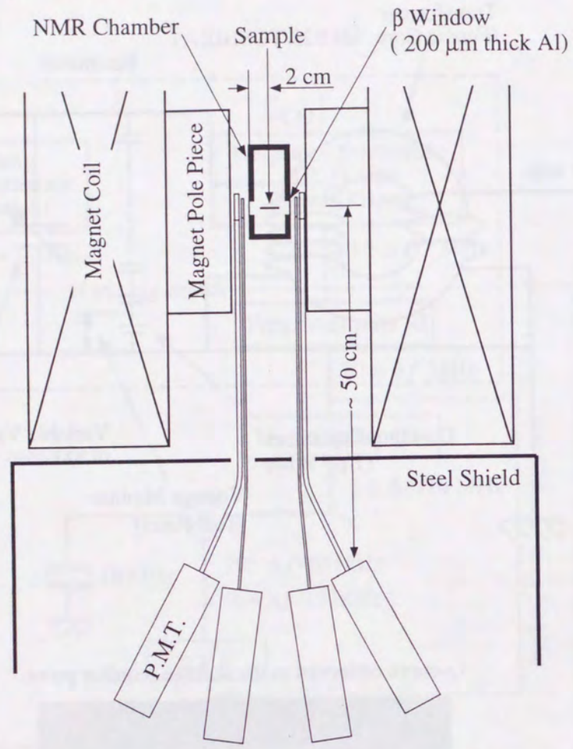

(b) Sizes of the detectors

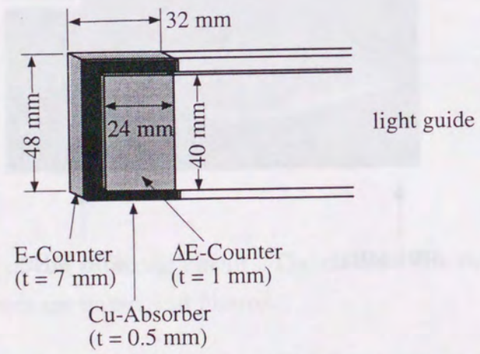

Figure 3.7 Experimental setups of β counters.

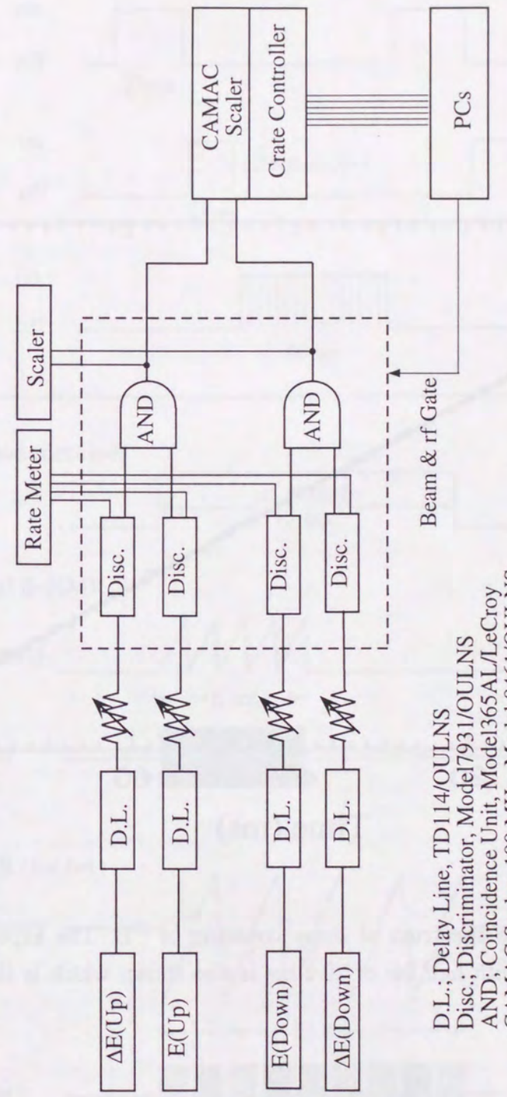

Figure 3.8 Block diagram of the β-ray detection system.

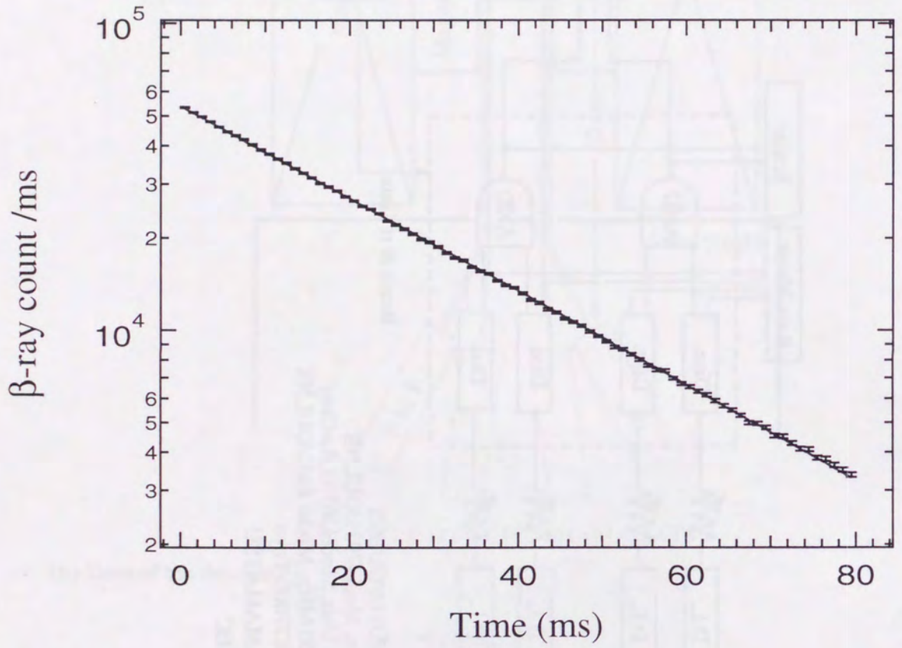

Figure 3.9 Typical time spectrum of β-ray counting of ^{12}B. The exponetial decay line with half life of 20.2 ms is also shown which is the one of ^{12}B.

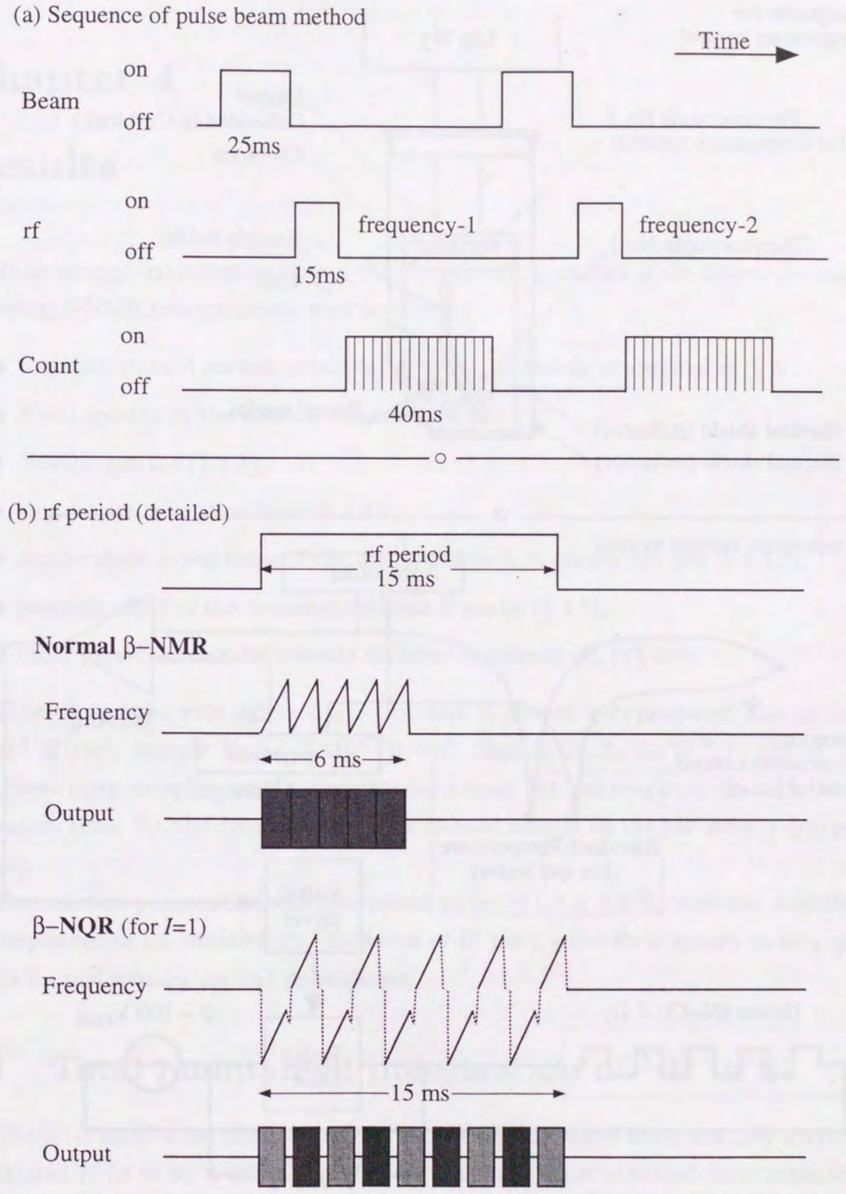

Figure 3.10 (a) Timing program of the pulsed beam method. (b) Two rf applying techniques were used in this experiment.

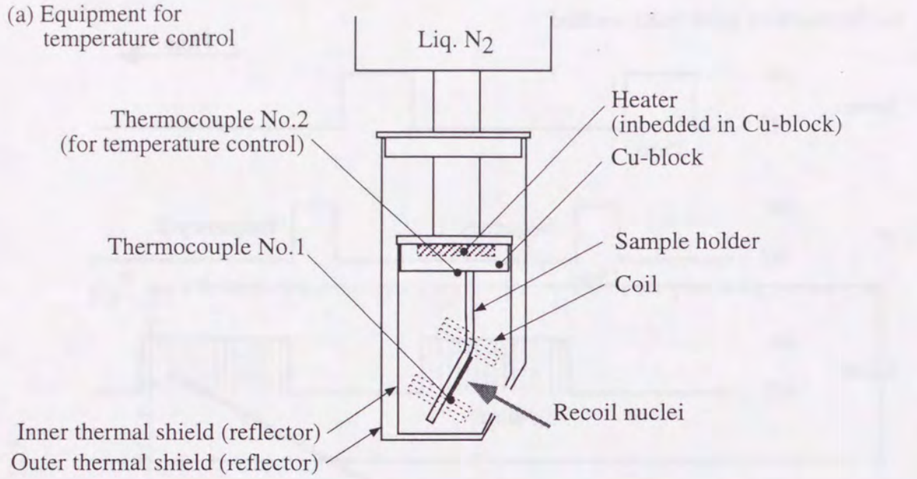

Figure 3.11 (a) Equipment for temperature control. Heat generated by the heater flows to the (LN_2) dewar. (b) Block diagram of temperature control system. External resister was used for supplying low power constantly, if needed.

Chapter 4

Results

To determine implantation sites of ^{12}B and to study dynamics of the defects annealing, following β-NMR measurements were performed;

- total maintained nuclear polarization by use of widely modulated rf (§ 4.1),
- NMR spectra at the Larmor frequency (§ 4.2),
- β-NQR spectra (§ 4.3),
- spin-lattice relaxation time (§ 4.4.1)
- temperature dependence of the fraction of each implantation site (§ 4.4.2),
- jumping effect of the nonsubstitutional B nuclei (§ 4.5),
- other measurements for a newly detected resonance (B_x) (§ 4.6).

Three Si samples with different concentration of dopant were prepared; Sample No.1: 3×10^{14} B/cm^3, Sample No.2.: 7×10^{17} B/cm^3, Sample No.3: 6×10^{14} P/cm^3 (§ 3.6). For these three samples, results were similar except for jumping rate and spin-lattice relaxation time. So, the descriptions will be focused mainly on the low density p-type Si sample.

The reaction polarization was determined to be -11.3 ± 0.2 %, from the β-NMR on ^{12}B implanted in an annealed Pt (thickness of 15 μm), since Pt is known to be a good media for maintaining nuclear polarization.

4.1 Total maintained polarization of ^{12}B in Si

The total maintained polarization of ^{12}B in Si was measured using a widely frequency modulated rf ($\nu = \nu_L \pm 200$ kHz). Fig.4.1 (a) shows thus obtained total maintained polarization of ^{12}B. Since the reaction polarization is determined to be -11.3 ± 0.2 % from the measurement of ^{12}B in Pt, almost all the polarization of implanted ^{12}B is kept at temperatures below 260 K and above 550K. Above 260 K, the fraction of the detectable polarization decreases rapidly and reached approximately 60 %. In the temperature

range from 300 K to 450 K, the fraction was kept constant (60 %), and increases rapidly again to 100 % at about 500 K. Similar results were obtained for other two samples No.2 and No.3 as shown in Fig.4.2(a) and (b).

In order to check that all the ^{12}B which maintained the polarization was manipulated by the present frequency range $\nu = \nu_L \pm 200$ kHz, polarization was also deduced from the ratio of the counting rate in up and down counters as described blow. Since the full polarization was detected by the β-NMR at 100 K or 550 K, the polarization was totally destroyed by an rf at these temperatures. Therefore, the maintained polarization at any temperature can be obtained by comparing the counting rate ratio at the temperature with that at 100 K, where the polarization completely destroyed with rf on

$$2AP = \frac{(U(T)/D(T))_{\rm off}}{(U(100\ {\rm K})/D(100\ {\rm K}))_{\rm on}} - 1,$$

where $U(T)$, and $D(T)$ are the β-ray counts at the temperature T. Subscripts shows whether the rf is on or off. The result is shown in Fig.4.1 (b). Thus obtained polarization was almost the same as the result obtained by use of the direct β-NMR detection at temperature T. From the analysis of the result, it is concluded that all the resonance frequencies are covered within the present frequency range $\nu = \nu_L \pm 200$ kHz. The similar results were obtained for other samples as well.

4.2 Resonance line of ^{12}B nuclei at the substitutional sites (B_S)

As mentioned in §1.1, McDonald and McNab determined that only the ^{12}B nuclei in the substitutional site contributed to the sharp resonance at the Larmor frequency [MM76]. In the present experiment, NMR spectra at the Larmor frequency which come from the substitutional ^{12}B were observed at various temperatures (100 K $\leq T \leq$ 750 K). The experimental conditions are listed in Table 4.1. Typical NMR spectra are shown in Fig.4.3–4.5. Remarkable change was shown in the amplitude of the spectra with increasing temperature.

The spectra were fitted with Lorentzians to extract resonance amplitude. The fraction of the substitutional ^{12}B was determined from the amplitude of the resonance. The rf field H_1 of about 0.5 Oe was strong enough to saturate the spectra. The fraction of ($^{12}B_s$) was defined as the resonance amplitude normalized by the reaction polarization, which is the full polarization of ^{12}B in Pt.

The results are shown in Fig.4.6. Below 100 K, the fraction is almost zero. As the

Table 4.1 Experimental conditions for the Larmor resonance.

External magnetic field (H_0)	6 kOe
Beam bombardment time	25 ms
rf time	15 ms
	(on: 6 ms / off: 9ms)
Counting time	40 ms
rf intensity (H_1)	0.5
rf modulation	no modulation
Crystal orientation	$\langle 110 \rangle \parallel H_0$

temperature goes up, the substitutional fraction gradually increases to reach 80 % at 650 K. The slope of the increase seems to change slightly at 400 $\sim$ 450 K as is seen in the literature as well.

The observed line widths ($\sim$850Hz FWHM) were broader than the natural width (Table 1.2) due to the relatively intense H_1 field, and were consistent with the present power broadening $\gamma H_1/2\pi \approx 760$ Hz (FWHM).

The polarization was observed as a function of time and the spin-lattice relaxation time T_1 was obtained by χ^2-fitting analysis. The results are shown in Fig.4.6. Relaxation of the polarization was not observed at any temperatures and dopant density. Thus, the spin-lattice spin relaxation time T_1 was long enough compared with the nuclear lifetime, expected from the low conduction electron density. (Fig.4.11).

4.3 β-NQR spectra (B_x, B_{ns})

β-NQR spectra were observed at the frequency range from $\nu_{Q\rm split} = 0$ kHz to 400 kHz. Here, the $\nu_{Q\rm split}$ means the full span between the two resonance-frequencies split due to quadrupole interaction, or twice of the distance between the Larmor frequency and one of the resonance frequency. Experimental conditions are tabulated in Table 4.2.

The typical spectra are shown in Fig.4.6–4.9. Two resonance lines are clearly seen in the observed β-NQR spectra around $\nu_{Q\rm split} = 270$ kHz and 0kHz.

The sharp resonance at $\nu_{Q\rm split} = 270$ kHz comes from the nonsubstitutional ^{12}B (B_{ns})

Table 4.2 Experimental conditions for β-NQR spectra.

External magnetic field H_0	6 kOe
Beam bombardment time	25 ms
rf time	15 ms
	(on: 12 ms / off: 3 ms)
Counting time	40 ms
rf intensity	1 Oe
rf modulation	$\pm$ 10 kHz in $\nu_{Q\mathrm{split}}$
Crystal orientation	$\langle 110 \rangle \parallel H_0$

which have an $\langle 111 \rangle$ axial symmetry, which have been found also by Fischer *et al.* by the conventional β-NMR [FSD+92].

The broad resonance around $\nu_{Q\mathrm{split}} = 0$ kHz was detected for the first time. This resonance corresponds to the missing fraction of ^{12}B implanted in Si, which was predicted from the previous experiments by Minamisono *et al.* [MNDA83]. Although the resonance line overlapped with the sharp resonance line for the substitutional ^{12}B, the two resonances could be separated since their line widths are very much different. From now on, the ^{12}B nuclei contributed to this newly detected broad resonance is labeled as $^{12}\mathrm{B_x}$, which will be discussed later in § 4.6.

For the resonance for $\mathrm{B_{ns}}$, it have been known that the quadrupole interaction has the $\langle 111 \rangle$ axial symmetry with the coupling constant $|eqQ/h| = 2\nu_Q/3 = 360(15)$ kHz [SFD+92]. We confirmed the $\langle 111 \rangle$ symmetry. As shown in Fig.4.10–(a), the β-NQR spectra were observed for three crystal orientations, *i.e.*, $\alpha = 0°$ ($\langle 001 \rangle$), 22.5° and 45° ($\langle 011 \rangle$), where α is angle between H_0 and $\langle 001 \rangle$ axis in the $\{100\}$ plane. The resonance frequency for $\mathrm{B_{ns}}$ is far from the Larmor frequency at $\alpha = 45°$. It comes closer to the Larmor frequency as α decreases, because all the four $\langle 111 \rangle$ axis become to form the magic angle with the external magnetic field H_0. The obtained $\nu_{Q\mathrm{split}}$ is shown as a function of α in Fig.4.10 (b). Assuming the asymmetry parameter $\eta = 0$, the fit to the Eq.2.11 proves that $\mathrm{B_{ns}}$ nuclei are at the site where q is parallel to the $\langle 111 \rangle$ axis with its quadrupole coupling constant $|eqQ/h|$ of 364(7) kHz.

While the $\mathrm{B_{ns}}$ resonance was clearly observed at 150 K and 250 K as seen Fig.4.6–4.9, it disappeared at 350 K. This temperature dependence will be described later in § 4.4.

Table 4.3 Experimental conditions for measurement of fractions.

Experiment	for $\mathrm{B_{ns}}$	for $\mathrm{B_s}$+ $\mathrm{B_x}$
External magnetic field H_0	6 kOe	
Beam bombardment time	25 ms	
rf time	15 ms	15 ms
	(on: 12 ms / off: 3 ms)	(on: 6 ms / off: 9 ms)
Counting time	40 ms	
rf intensity	5 Oe	
rf modulation	$\pm$ 100 kHz in $\nu_{Q\mathrm{split}}$	
Crystal orientation	$\langle 110 \rangle \parallel H_0$	

From these β-NMR spectra, it was revealed that there are at least three implantation sites of $^{12}\mathrm{B}$ – $\mathrm{B_s}$, $\mathrm{B_{ns}}$, and $\mathrm{B_x}$.

4.4 Temperature dependence of the fraction and the spin-lattice relaxation time for each implantation site

Fractions of $\mathrm{B_{ns}}$ and $\mathrm{B_x}$ sites as well as the $\mathrm{B_s}$ site were measured as a function of temperature. The fraction of $\mathrm{B_s}$ was determined from the amplitude of the sharp resonance at Larmor frequency as is already described in § 4.2. The fractions of $\mathrm{B_{ns}}$ were determined from the amplitude of the peak at $\nu_Q = 270$ kHz in the β-NQR spectra using a wide rf modulation $\nu_{Q\mathrm{split}} = 270 \pm 100$ kHz for the crystal orientation $\langle 110 \rangle \parallel H_0$. Sum of the fractions for ($\mathrm{B_s}$+ $\mathrm{B_x}$) was determined from the polarization destruction method in the β-NMR with a wide rf modulation ($\nu = \nu_L \pm 50$ kHz). Experimental conditions are tabulated in Table 4.3. Applied rf intensity, H_1, was enough to destroy the polarization corresponding to each site completely.

4.4.1 Spin-lattice relaxation time T_1

Before describing the result of the fractions, time-dependent phenomena must be clarified. In all β-NMR measurements, the time-development of the polarization was also measured to extract the relaxation time. Experimental conditions for (B_s+ B_x) and B_{ns} measurements were the same as mentioned above (Table 4.3). For B_s, several data points near the Larmor frequency were summed up.

Although no significant relaxation was seen for (B_s+ B_x) and B_s, T_1 for B_{ns} around 300 K was very fast as seen in Fig.4.12–4.14. All these time dependence of the polarization were analyzed by χ^2-fitting using exponential decay. Resultant relaxation rates for B_s or (B_s+ B_x) are shown in Fig. 4.11. The relaxation rate $1/T_1$ and the initial polarization, which is defined by the polarization that was at the production time, are shown in Fig.4.15 – Fig.4.17. From the figures, fixed fraction of ^{12}B is located in B_{ns} site and the reduced polarization of the $^{12}B_{ns}$ nuclei is due to the polarization reduction by short relaxation time T_1.

While the spin-lattice relaxation time T_1 becomes shorter as the temperature increases, the fraction of B_{ns} is almost constant of about 35 % below 325 K. The polarization for B_{ns} nuclei was completely disappeared above 350 K, because of the too short relaxation time.

It should be noted that the behavior of the relaxation time with temperature for the highly doped sample is slightly steeper than the one for the sample with lower density of dopant.

4.4.2 Fraction for each location

The observed polarization during the counting time of 40 ms is shown in Fig.4.18–4.20 (a). Inner consistency of the present procedure was checked by comparing the sum of the polarizations change of the ones for B_s, B_x and $B_{ns}$with the total maintained polarization. Fig.4.18–4.20 (b) shows the fraction of each implantation site. The B_{ns} fractions are the one deduced as described in §4.4.1. The B_x fraction was obtained by subtracting B_s fraction from the sum of the (B_s+ B_x) fraction.

As seen in Fig.4.18–4.20 (a), the total amount for the (B_s+ B_x) fraction stays nearly constant in the temperature range from 100 K to 450 K, although the B_s increases with temperature. It may imply that ^{12}B in the B_x site, which is the majority at the lower temperature, seems to be converted into B_s site at higher temperatures.

While almost 100 % of polarization of ^{12}B is detected at temperature below 260 K, the

"total" polarization decreases to about 60 % above 300 K. This decrease is mainly because of the decrease of the B_{ns} component because the fraction of (B_s+ B_x) is constant. At temperatures above 260 K, the observed polarization for the B_{ns} nuclei rapidly decreases and disappears at a temperature higher than 350 K. Although the polarization of B_{ns} couldn't be observed above the temperature, it is natural to conclude that even at the temperatures higher than 350 K, about 35 % of implanted ^{12}B nuclei is located in the B_{ns} site and its polarization is destroyed due to the fast T_1 for B_{ns} nuclei.

At 450 K, the (B_s+ B_x) fraction starts to increase and completely recovers to 100 % at 550 K, while at higher temperatures above 650 K, the fraction of B_s is reached to about 80 % and seems to be saturated (the measurement in this temperature range was performed only on the low doped p-type Si).

4.5 Jumping effect of B_{ns} nuclei

It has been suggested by Ackermann *et al.* (§1.1) that the direction change of q-axis was caused by thermal activated atomic jumps. In order to see the effect caused by the direction change of q-axis at the location of B_{ns} atom, the polarization change was measured by applying just one resonance frequency among the two frequencies split by the quadrupole interaction. When only one transition frequency is applied, the nuclear polarization is just partially destroyed without jumping effect. If the direction of q-axis did not change at least within the rf period, the polarization change is expected to be about 1/4 of that in the case of complete destruction, assuming zero initial spin alignment. This situation is illustrated in Fig.4.21.

As shown in Fig.4.22–4.24 by B_{ns}(H or L), at low temperatures below about 200 K, just 1/4 of the total B_{ns} is observed for the single transition, which implies the nuclei are indeed immobile at least in the time range of the present experiment (~40 ms). Above 200 K, however, the polarization change increases as the temperature and reached total B_{ns} at about 275 K, which implies the direction change of the q-axis due to the jump between four identical locations. Above the temperature, it rapidly reduced to zero coincident with the decrease of the total B_{ns} signal, because of its fast spin-lattice relaxation time. This phenomena due to fast thermal jumping was the one also reported in the previous experiment by Frank *et al.* [FDE+94]. However, they couldn't deduce the jumping rate, mainly because of the lack of the knowledge on the polarization relaxation and the total polarization for B_{ns}. The jumping rate deduced from the present result will be discussed in the next chapter.

4.6 Other features for B_X

In order to understand the nature of the broad resonance from ^{12}B in B_x site nuclei, three other measurements were performed.

(1) Fig.4.25 shows three kinds of polarization changes for B_x; the polarization (P_X) was measured by the β-NQR method with $\nu = \nu_L \pm 35$ ($\Delta\nu = 25$ kHz), the other two (P_X(H or L)) were measured when only on the higher or lower side of the Larmor frequency was applied ($\nu = \nu_L$ - 35 or + 35 kHz ($\Delta\nu = 25$ kHz)). Since P_X(H or L) is about 1/4 of P_X, the broad resonance around the Larmor frequency is due to static electric quadrupole interaction on the same reason discussed for B_{ns} in § 4.5. If it is due to any other static shift of magnetic field, the P_X(H or L) has to be about half of P_X. If it is due to the dynamic shift, it will be the same as P_X.

(2) The spectra for B_x at room temperature (~300 K) were measured at two different crystal orientations, $\angle(\langle 001\rangle \cdot H_0) = 22.5\,°$, and 45° in {100} plane, as seen in Fig.4.26. No angular dependence of spectra was observed. Therefore, it can be concluded that the principal axis of the quadrupole interaction is randomly distributed.

(3) As seen in β-NQR spectra (Fig.4.6), the resonance from B_x nuclei is narrower at higher temperatures. To see the narrowing of the spectrum more clearly, the β-NMR spectra were analyzed by χ^2-fitting assuming Gaussian distribution of $\nu_{Q\mathrm{split}}$. In this analysis, data points for $\nu_{Q\mathrm{split}} < 10$ kHz were rejected, since these data may be affected from the ^{12}B in B_s site. The obtained width are plotted as a function of temperature in Fig.4.27.

At $T \leq 200$ K the widths are constant (about 45 kHz). As increasing temperature from 200 K to 400 K, the width becomes narrower and reaches to approximately 20 kHz at 400 K. Above 400 K, the width is kept constant.

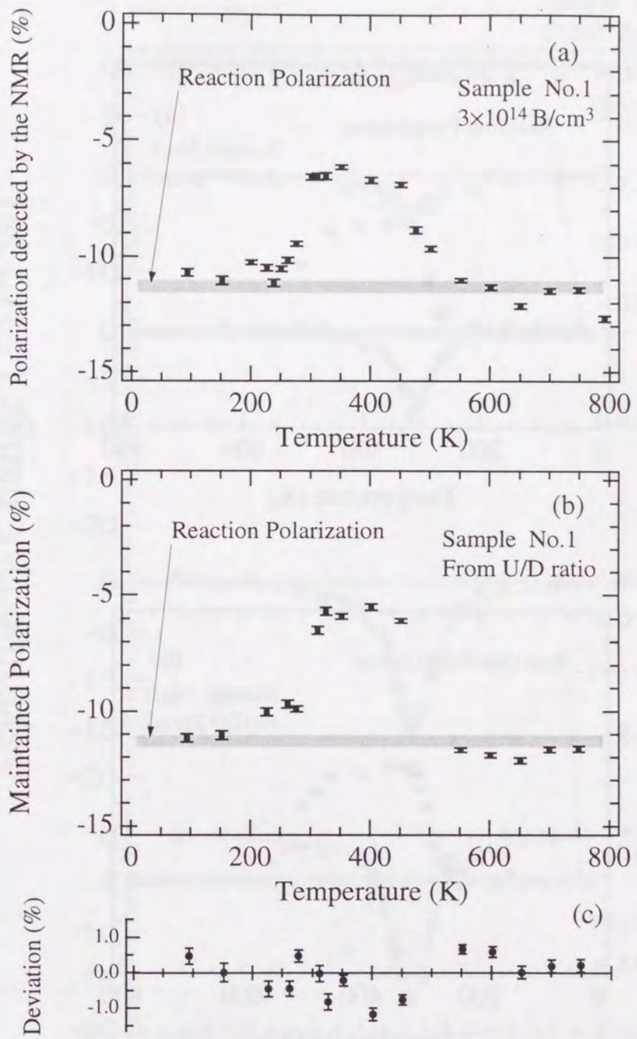

Figure 4.1 (a) NMR effect of ^{12}B in p-Type Si (3×10^{14} B/cm^3). The experimental conditions were $H_0 = 6$ kOe, and $f = 4591 \pm 200$ kHz, $H_1 \sim 10$ Oe. (b) Maintained polarization estimated from up/down count rate ratio. (See text.) (c) Deviations of NMR effects from maintained polarization.

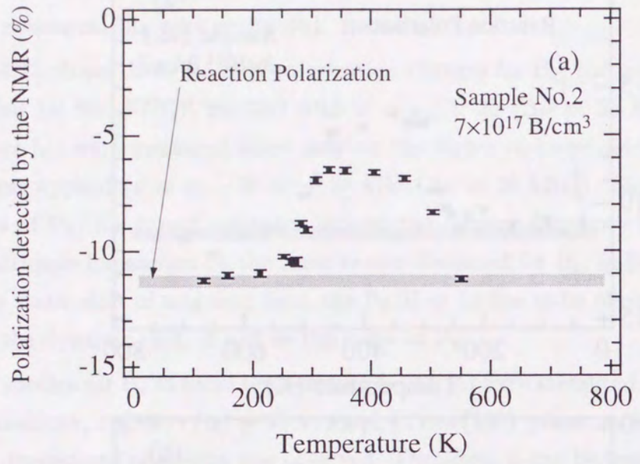

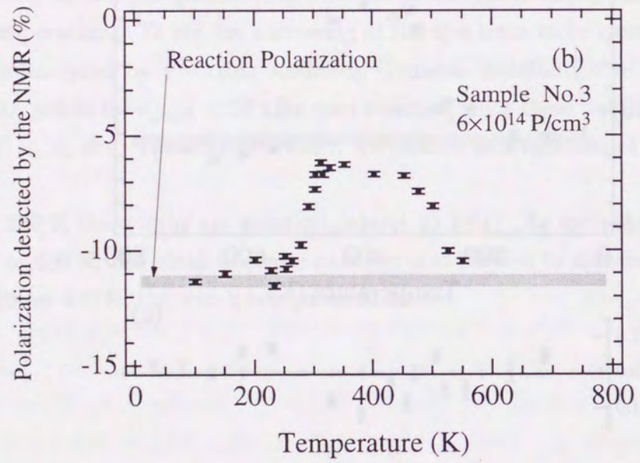

Figure 4.2 NMR effects of ^{12}B in (a) p-Type Si (7×10^{17} B/cm^3), (b) n-Type Si (6×10^{14} P/cm^3). The experimental conditions were $H_0 = 6$ kOe, $f = 4591 \pm 200$ kHz, and $H_1 \sim 10$ Oe.

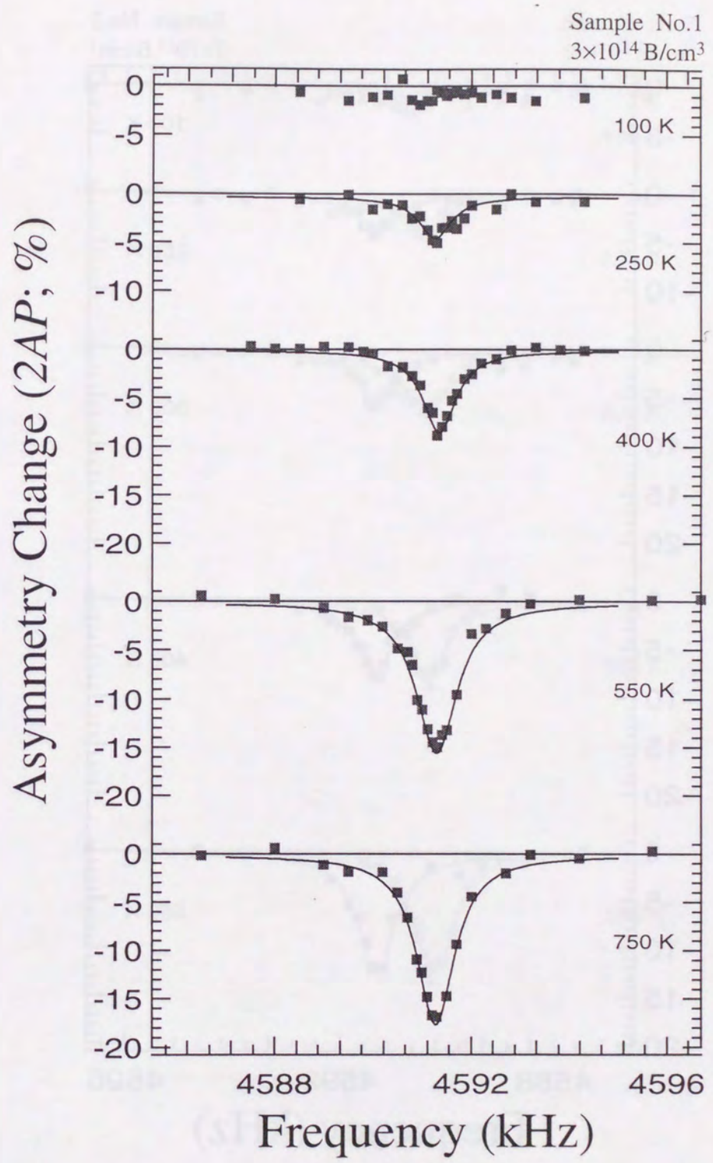

Figure 4.3 NMR spectra at the Larmor frequency of ^{12}B in p-type Si (3×10^{14} B/cm^3). The statistical error of each data point is about ± 0.5 %. The solid line is the Lorentzian curve best fit to each spectrum.

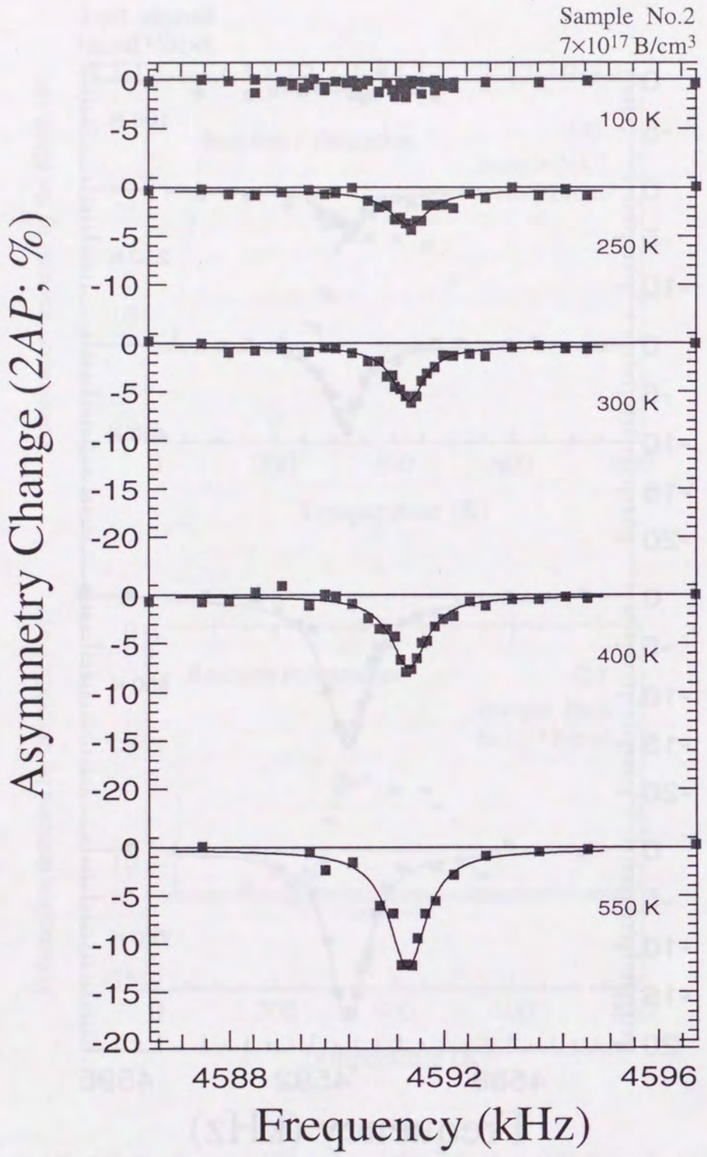

Figure 4.4 NMR spectra at the Larmor frequency of ^{12}B in p-type Si (7×10^{17} B/cm^3). The statistical error of each data point is about ± 0.5 %. The solid line is the Lorentzian curve best fit to each spectrum.

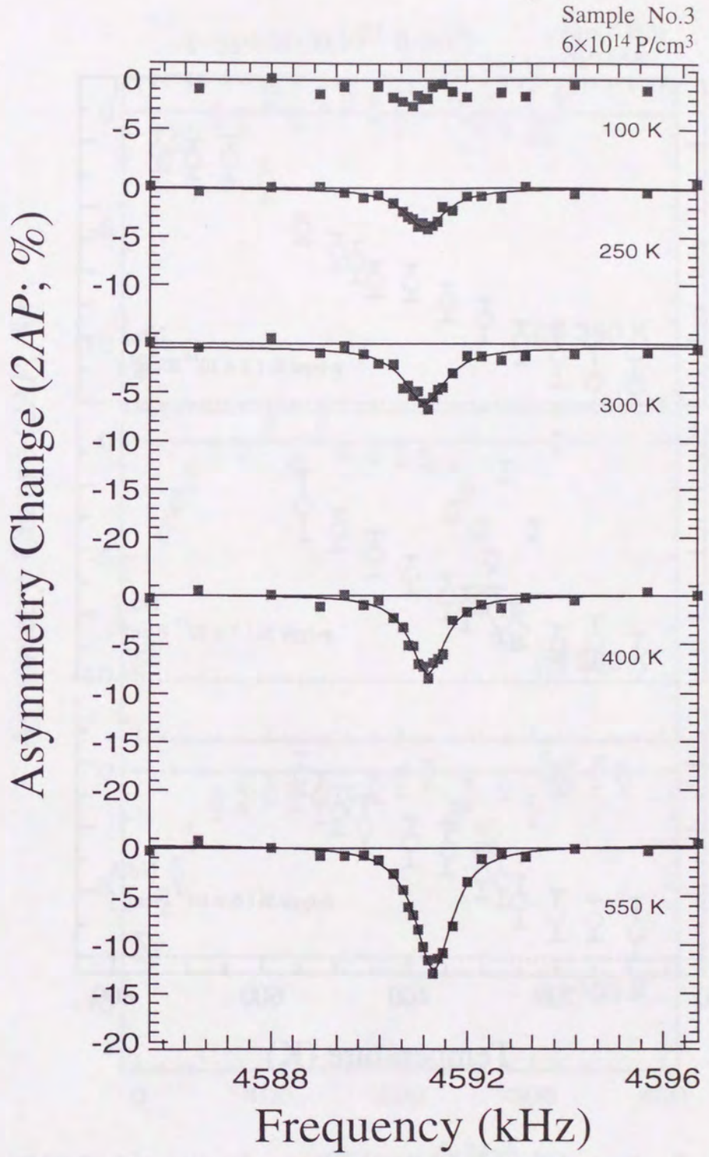

Figure 4.5 NMR spectra at the Larmor frequency of ^{12}B in n-type Si (6×10^{14} P/cm^3). The statistical error of each data point is about ± 0.5 %. The solid line is the Lorentzian curve best fit to each spectrum.

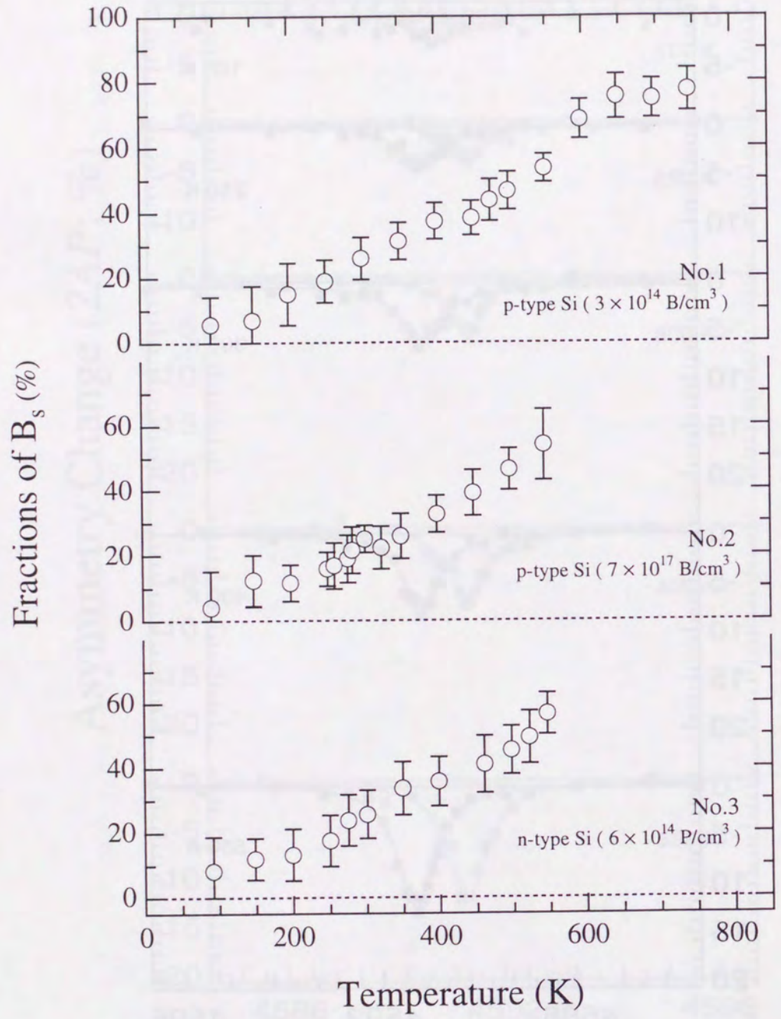

Figure 4.6 Fractions of the substitutional ^{12}B as a function of temperature. β-NQR spectra at (a) 350 K, (b) 250 K and (c) 150 K are given. Fractions are normalized by the total polarization obtained through nuclear reaction.

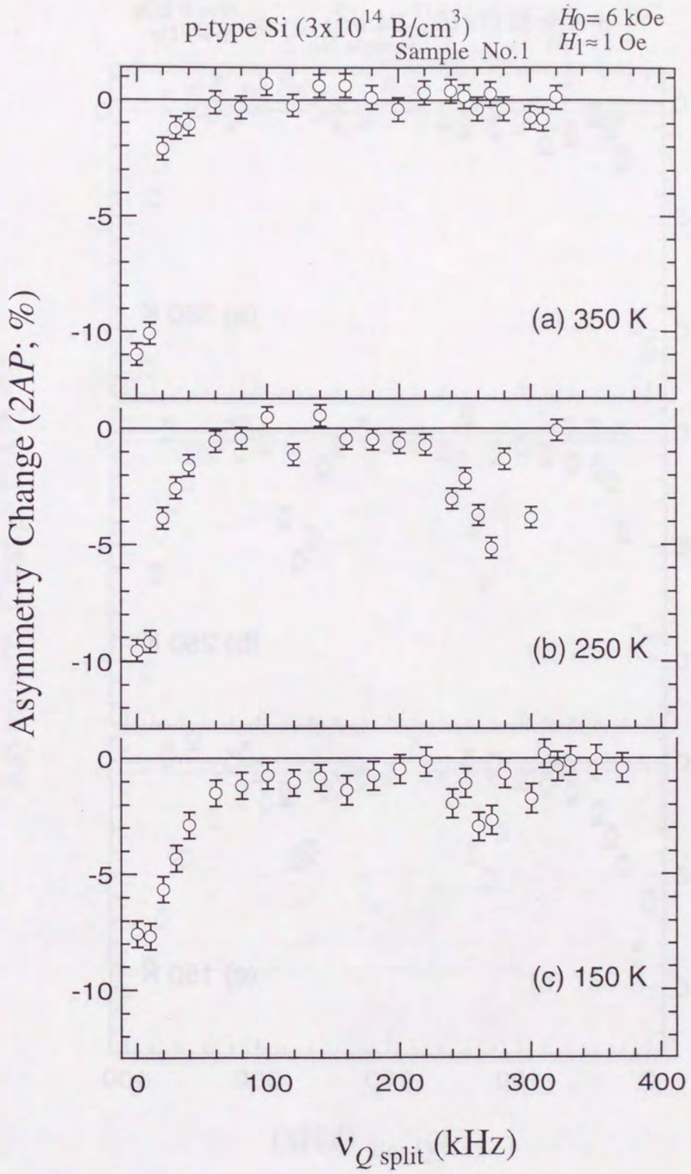

Figure 4.7 β-NQR spectra of ^{12}B in p-type Si (3×10^{13} B/cm^3). The width of the frequency modulation for $\nu_{Q\mathrm{split}}$ was $\pm$ 10 kHz.

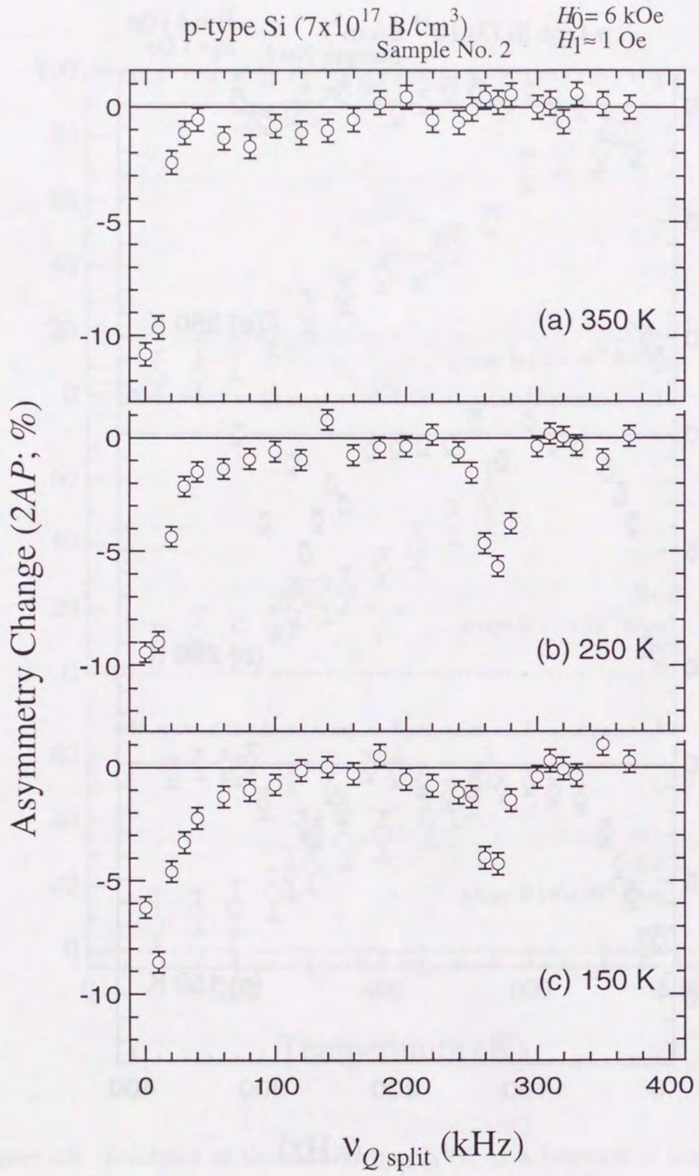

Figure 4.8 β-NQR spectra of ^{12}B in p-type Si (7×10^{17} B/cm^3). The width of the frequency modulation for $\nu_{Q\text{split}}$ was $\pm$ 10 kHz.

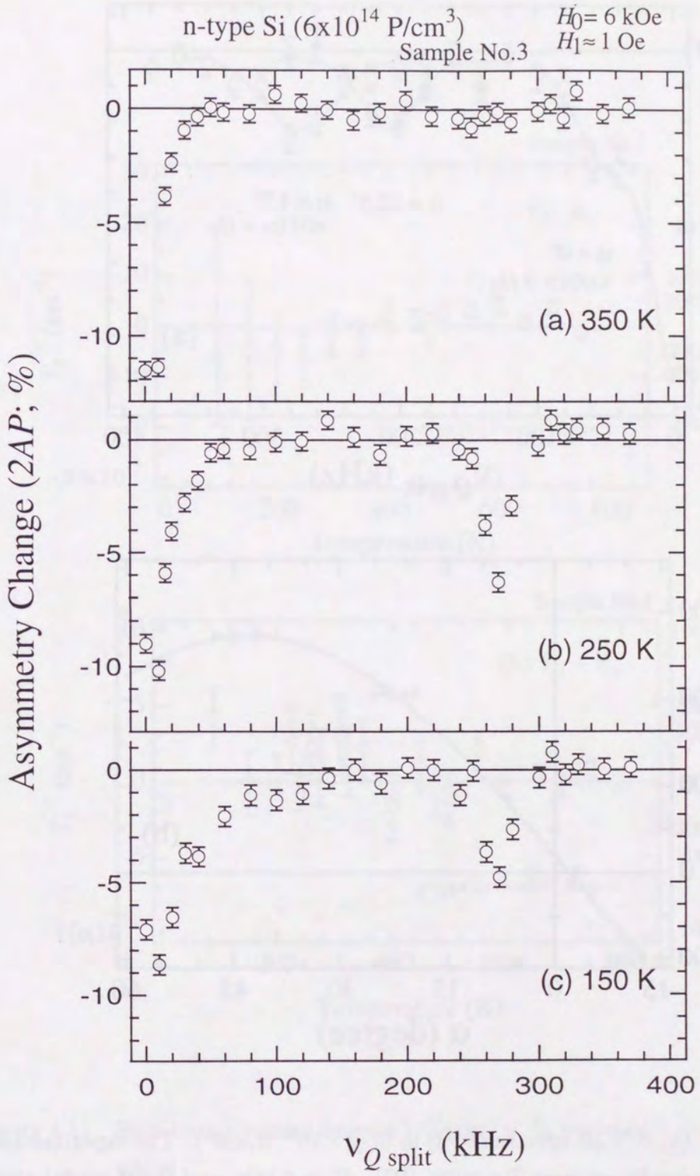

Figure 4.9 β-NQR spectra of ^{12}B in n-type Si (6×10^{14} P/cm^3). The width of the frequency modulation for $\nu_{Q\text{split}}$ was $\pm$ 10 kHz.

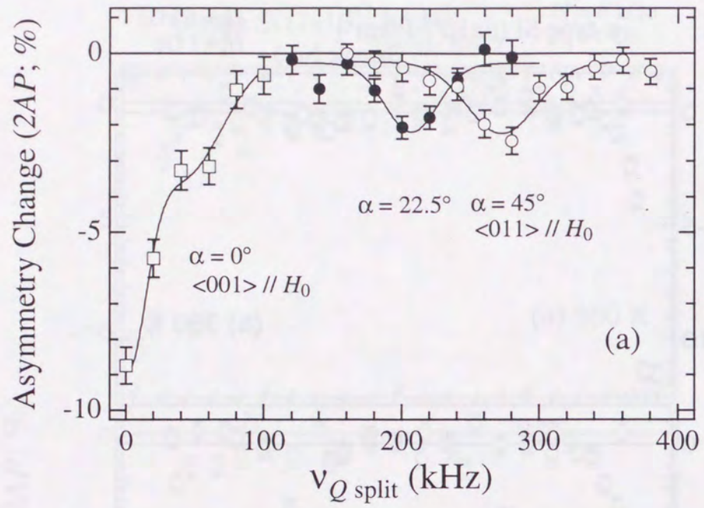

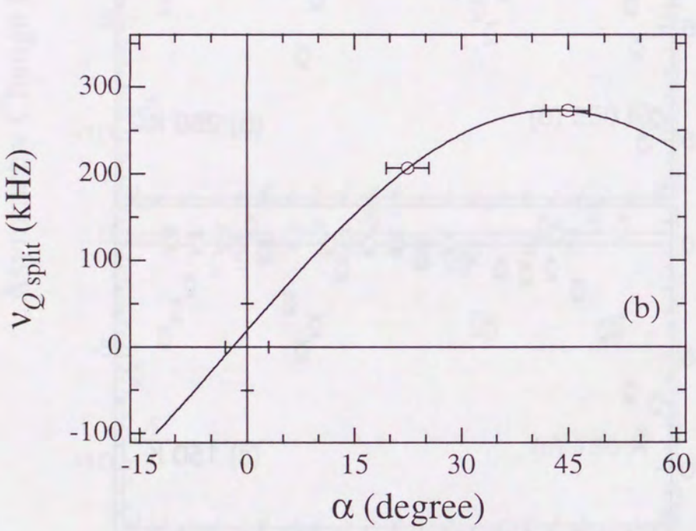

Figure 4.10 (a) β-NQR spectra of ^{12}B in Si (3×10^{14} B/cm^3). The experimental conditions were T $\sim$ 300K (RT), $H_0 = 6$ kOe, and the rf modulation $\Delta\nu_{Q\mathrm{split}} = \pm 10$ kHz. The solid line for $\alpha = 22.5°$, or 45° is Gaussian curve best fit to each spectrum. (The curve for $\alpha = 0°$ is given to guide the eyes.) (b) Angular dependence of $\nu_{Q\mathrm{split}}$. Solid line is the best fit to the data, which shows $\langle 111 \rangle$ axial symmetry.

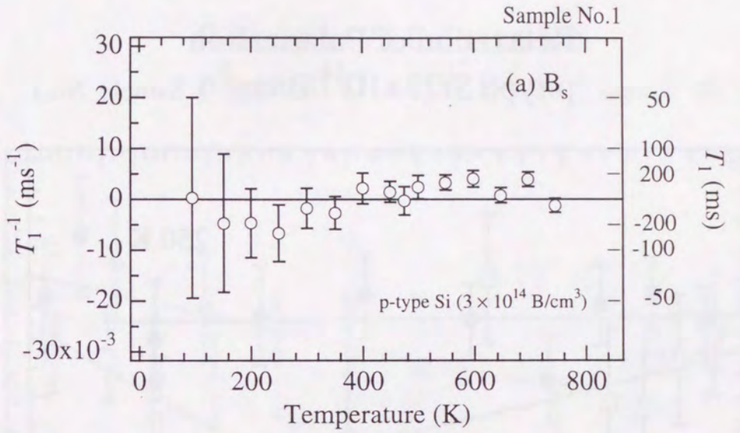

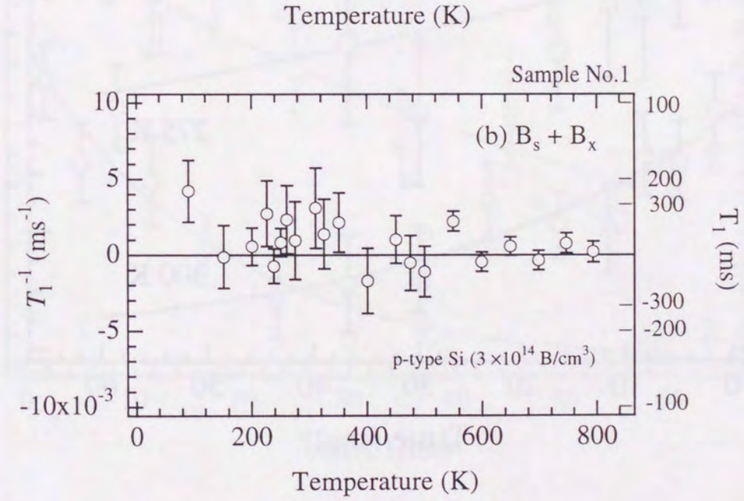

Figure 4.11 Spin-lattice relaxation rate $1/T_1$ for (a) B_s nuclei and (b) (B_s+ B_x) nuclei.

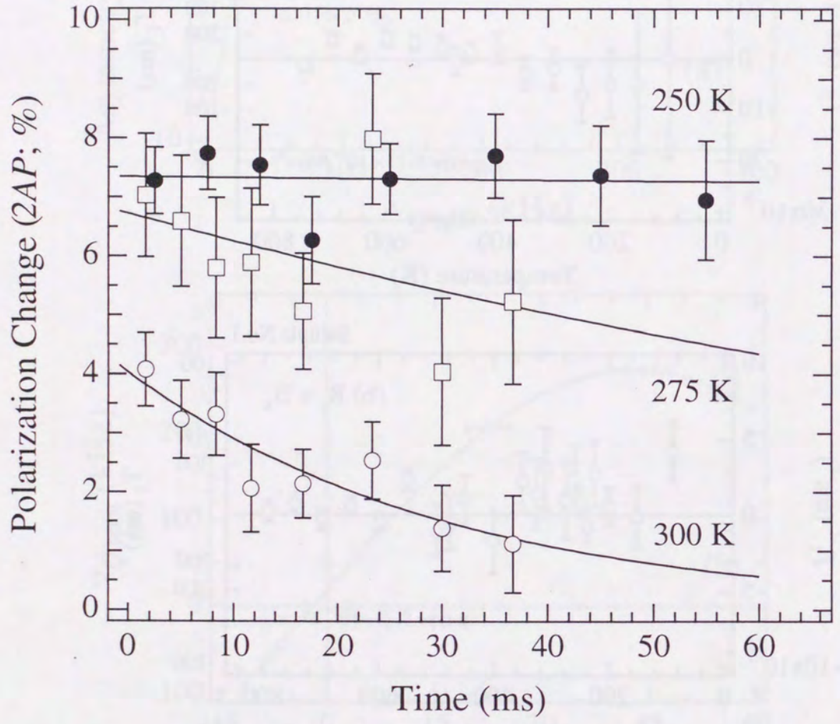

Figure 4.12 Spin-lattice relaxation times for B_{ns} nuclei in p-type Si (3×10^{14} B/cm^3). The solid curves are the exponential function best fit to the data.

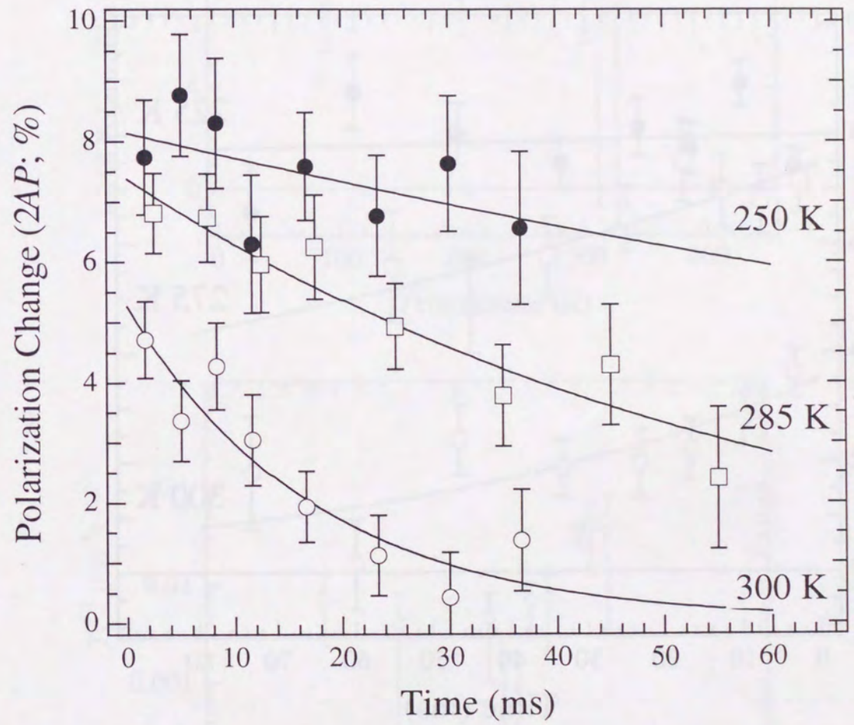

Figure 4.13 Spin-lattice relaxation times for B_{ns} nuclei in p-type Si (7×10^{17} B/cm^3). The solid curves are the exponential function best fit to the data.

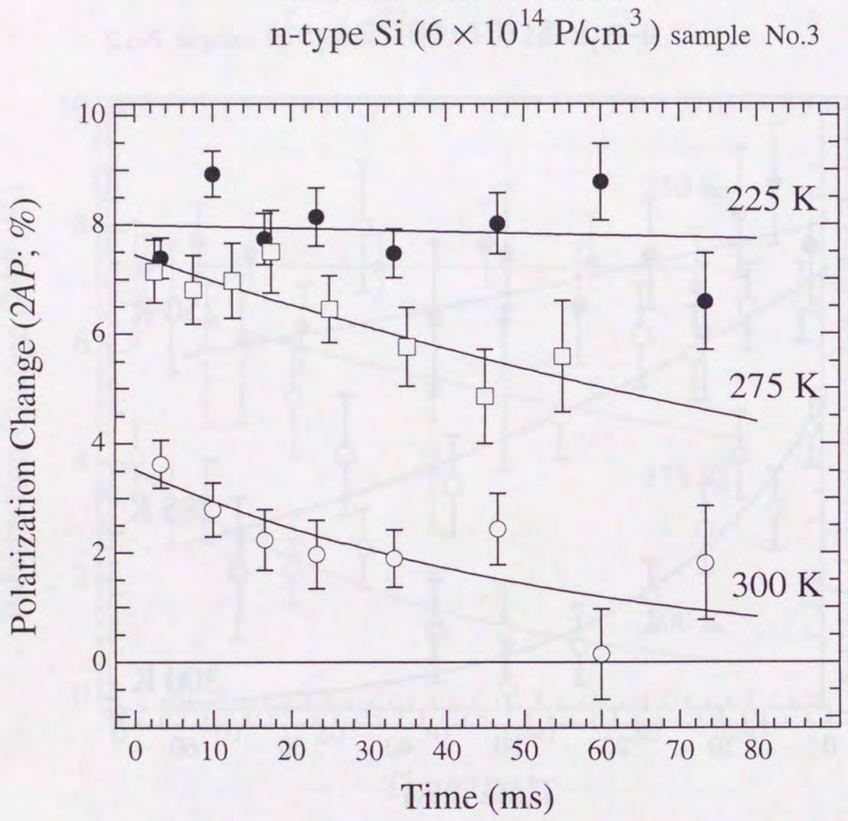

Figure 4.14 Spin-lattice relaxation times for B_{ns} nuclei in n-type Si (6×10^{14} P/cm^3). The solid curves are the exponential function best fit to the data.

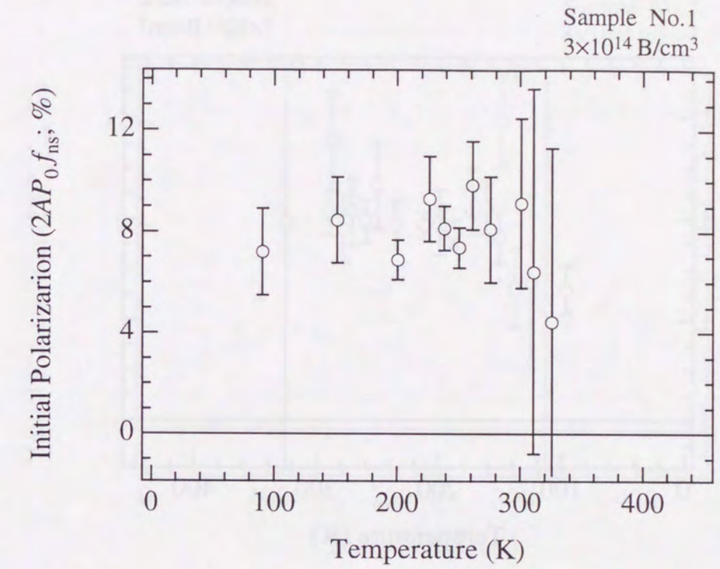

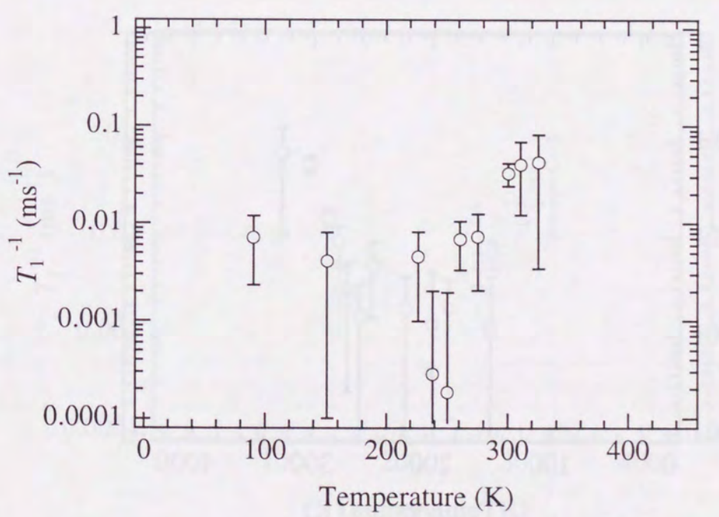

Figure 4.15 Initial polarization at the production time, and spin-lattice relaxation time for the B_{ns}nuclei in p-type Si (3×10^{14} B/cm^3).

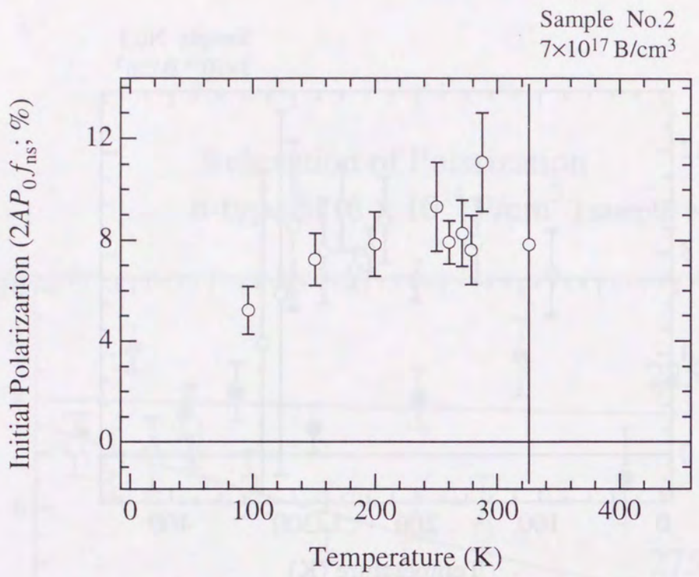

Figure 4.16 Initial polarization at the production time, and spin-lattice relaxation time for the B_{ns}nuclei in p-type Si (7×10^{17} B/cm^3).

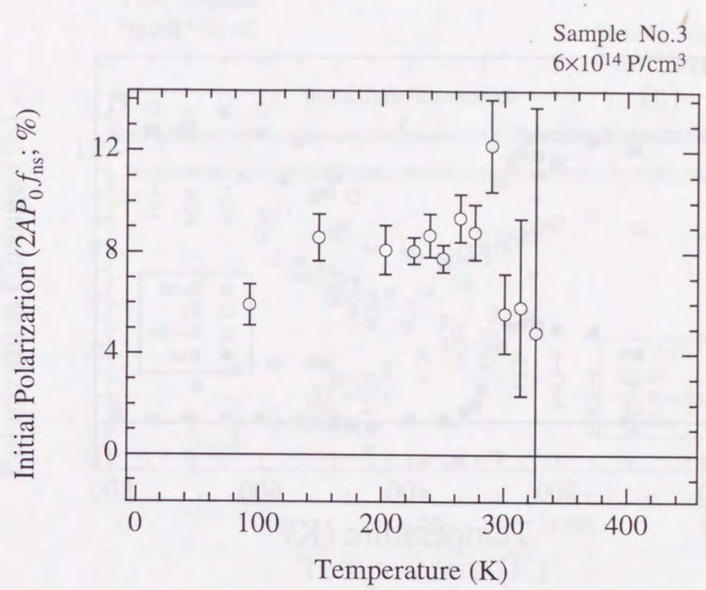

Figure 4.17 Initial polarization at the production time, and spin-lattice relaxation time of the B_{ns}nuclei in n-type Si (6×10^{14} P/cm^3).

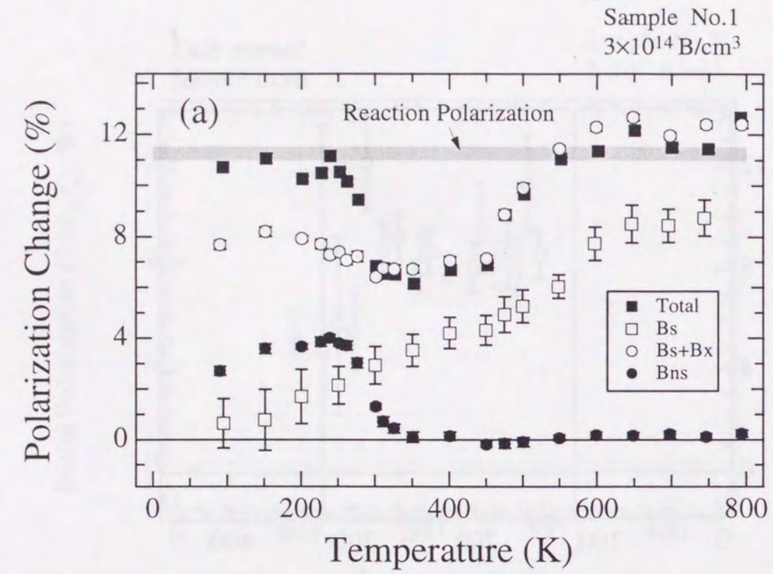

Figure 4.18 (a) Observed polarization changes of ^{12}B in p-type Si (3×10^{14} B/cm^3). (b) Fractions for each implantation site. The fraction for B_x was deduced by subtracting the fraction for B_s from the one for (B_s+ B_x).

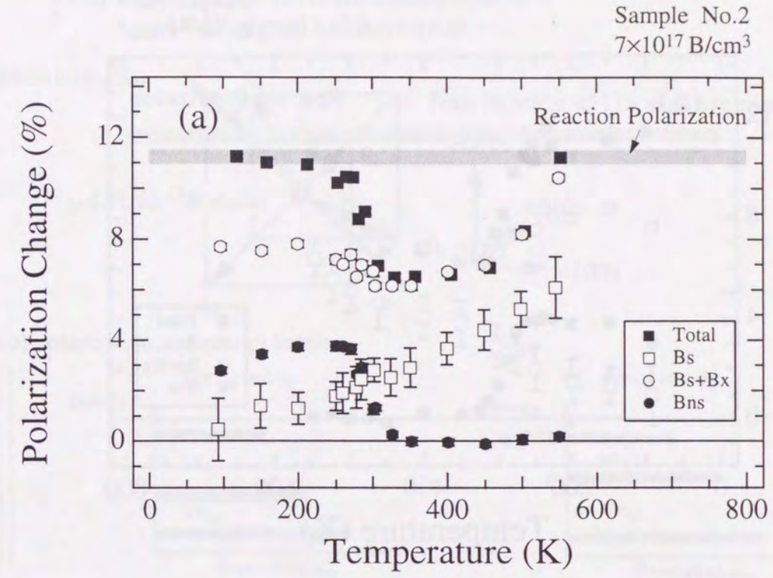

Figure 4.19 (a) Observed polarization changes of ^{12}B in p-type Si (7×10^{17} B/cm^3). (b) Fractions for each implantation site.

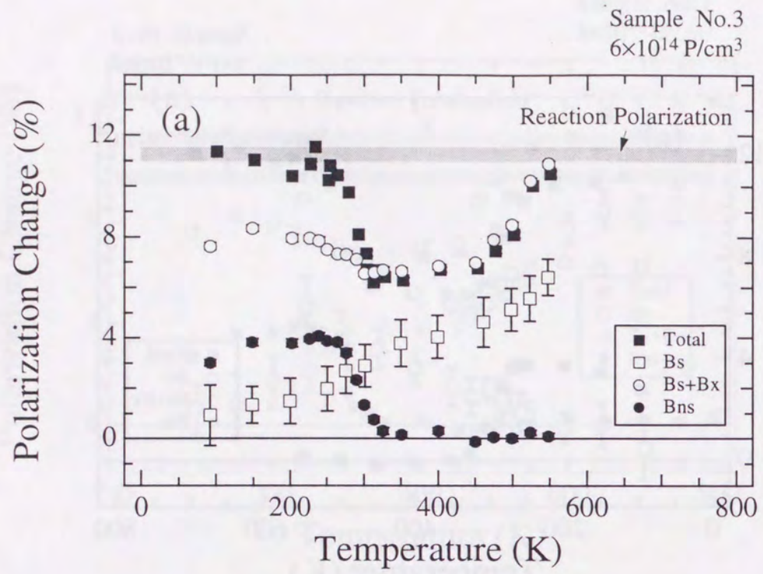

Figure 4.20 (a) Observed polarization changes of ^{12}B in p-type Si (6×10^{14} B/cm^3). (b) Fractions for each implantation site.

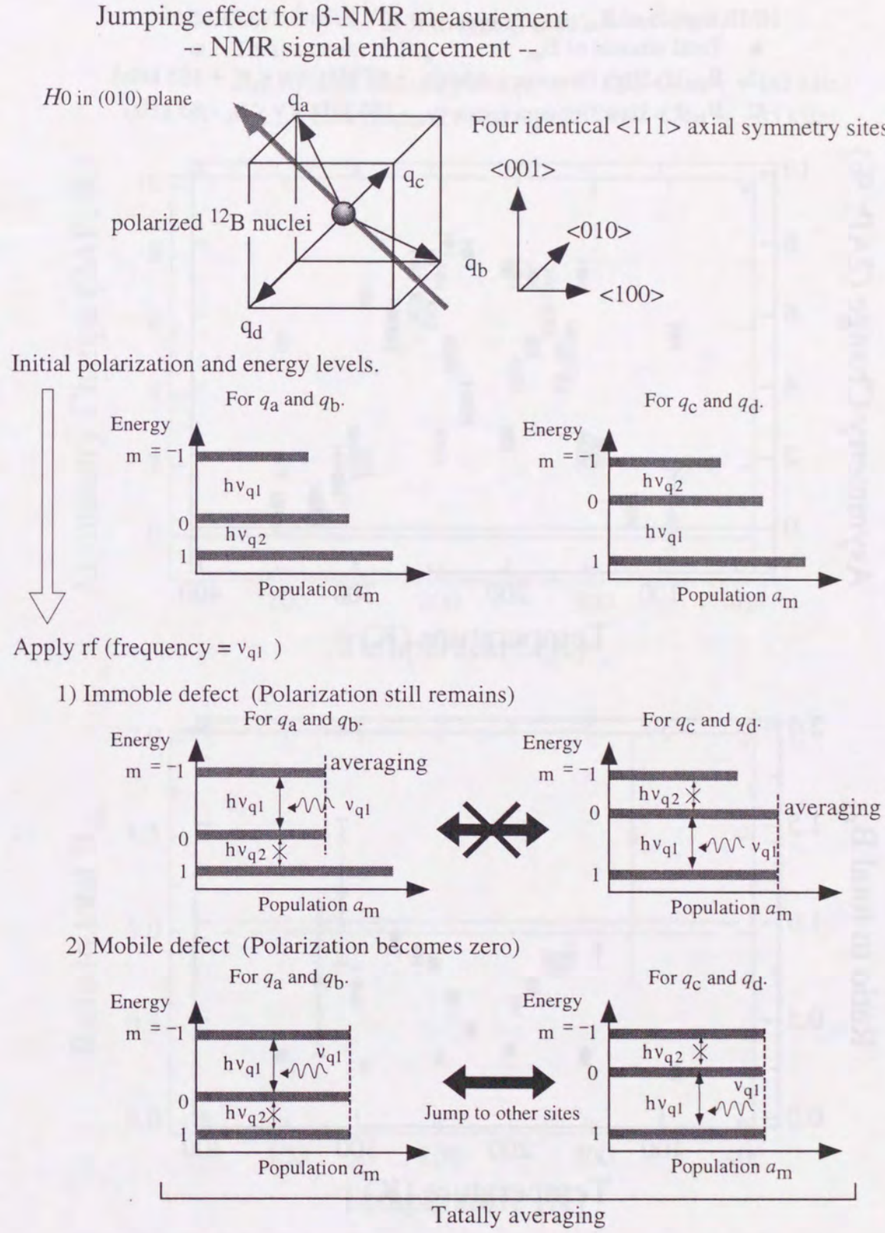

Figure 4.21 Jumping effect for an β-NMR measurement.

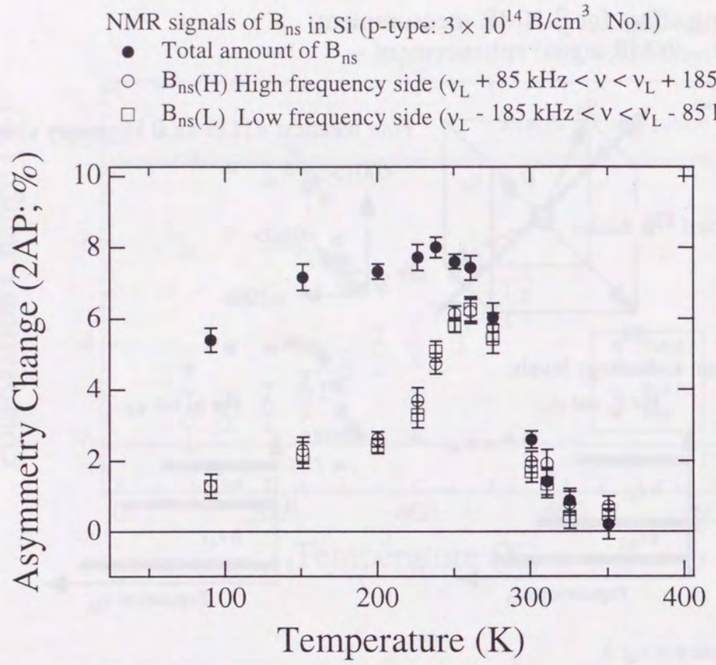

Figure 4.22 Enhancement of NMR signal for B_{ns} nuclei in p-type Si (3×10^{14} B/cm^3). Experimental conditions, except for the rf frequency, were same as the measurement of B_{ns} fraction.

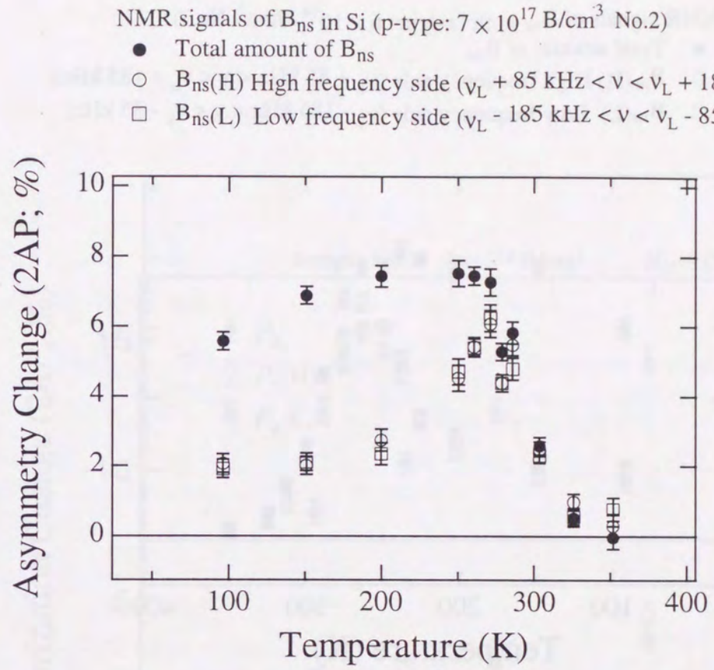

Figure 4.23 Enhancement of NMR signal for B_{ns} nuclei in p-type Si (7×10^{17} B/cm^3). Experimental conditions, except for the rf frequency, were same as the measurement of B_{ns} fraction.

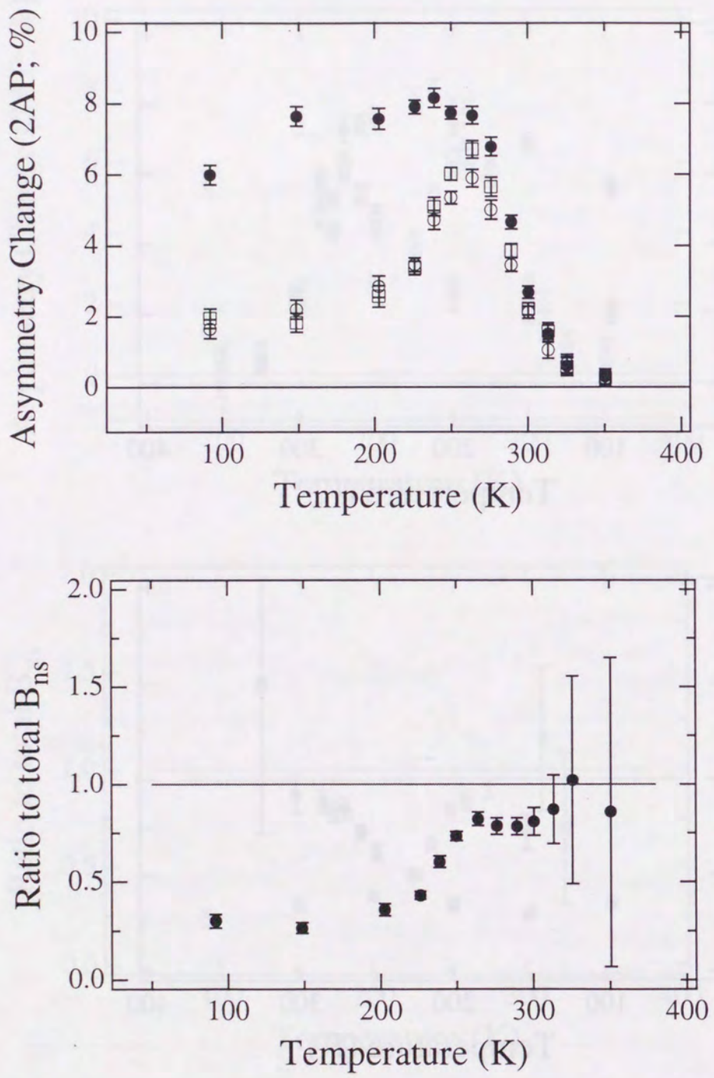

Figure 4.24 Enhancement of NMR signal for B_{ns} nuclei in n-type Si (6×10^{14} P/cm^3). Experimental conditions, except for the rf frequency, were same as the measurement of B_{ns} fraction.

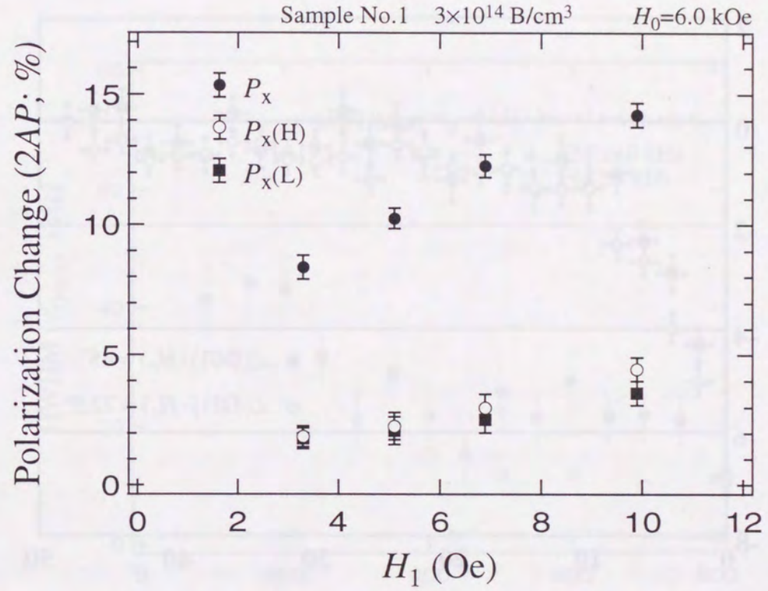

Figure 4.25 Asymmetry change of ^{12}B settled at B_x at temperature of 150 K. Closed circles represent the change in the rf frequency range of $\nu_{Q\text{split}} = 70 \pm 50$ kHz by use of the β-NQR method. Open circles and closed squares represent the change in the case of single rf, 70 + 50 kHz and 70 − 50 kHz respectively

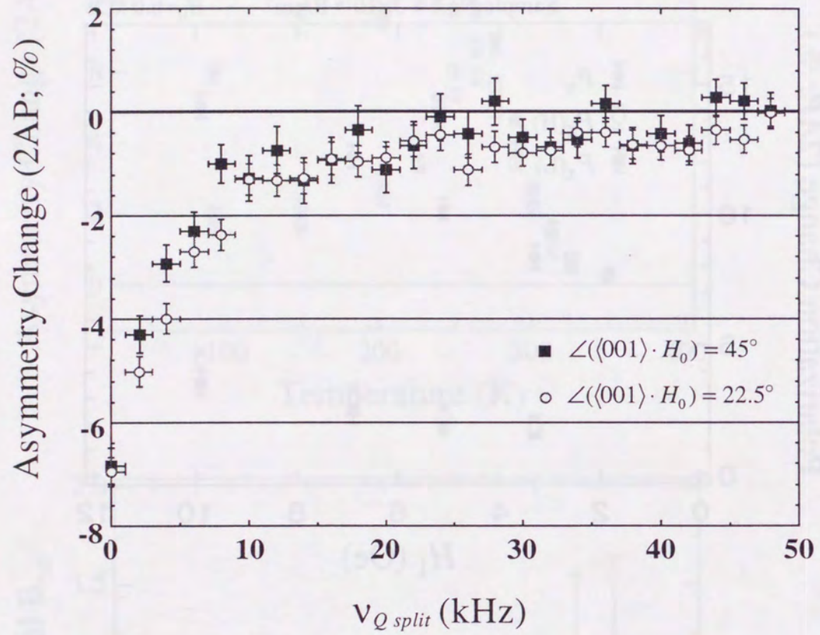

Figure 4.26 β-NMR spectrum with two crystal orientations. No significant difference was observed. (T = RT, $H_0 = 6.0$ kOe, $H_1 = 0.6$ Oe, p-type Si (7×10^{17} B/cm^3)

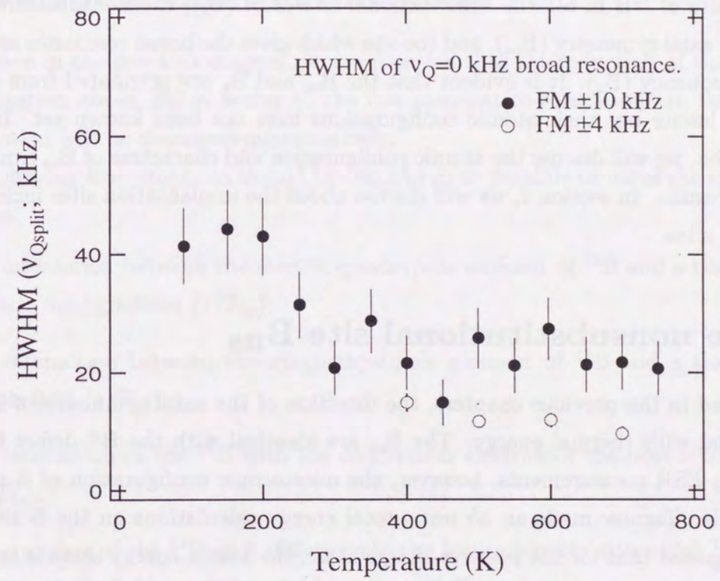

Figure 4.27 The HWHM of the resonance from B_x in the p-type Si (3×10^{13} B/cm^3).

Chapter 5

Discussions

In the previous chapter, it was disclosed that there are three components for the implantation site of ^{12}B in Si: the substitutional site of Si (B_s), the nonsubstitutional site with $\langle 111 \rangle$ axial symmetry (B_{ns}), and the site which gives the broad resonance around the Larmor frequency (B_x). It is evident that the B_{ns} and B_x are originated from some defects of the lattice but their atomic configurations have not been known yet. In the following section, we will discuss the atomic configuration and characters of B_{ns} from the experimental results. In section 2, we will discuss about the implantation sites including the B_s and B_x sites.

5.1 The nonsubstitutional site B_{ns}

As described in the previous chapters, the direction of the axial symmetry of B_{ns} is jumping around with thermal energy. The B_{ns} are identical with the B^+ defect found by (Watkins's) ESR measurements, however, the microscopic configuration of it is not known certainly. Tarnow made an *ab initio* total energy calculations on the B sites in Si. It was suggested that for the positive-charge state, the lowest energy state is neither simple interstitial B nor bond-centered B, but a substitutional B combined with a Si atom [Tar91](we denote this configuration as (B_s- Si_i) (Fig.5.1)). According to this calculation, since substitutional B is singly negative-charged and the interstitial Si is doubly positive-charged, the (B_s- Si_i) has an attractive coulomb interaction, which cause the slight lattice deformation: as the $\langle 111 \rangle$ direction is compressed, the perpendicular directions are expanded as shown in Fig.5.1. This model explains the variation of the direction of $\langle 111 \rangle$ axial symmetry by the jumping the Si_i atom through hexagonal interstitial site to other tetrahedral interstitial site with the activation energy of about 0.6 eV.

In the followings, through the discussion of the present results assuming this model, the validity of it will be examined. In accordance with this model, the present experimental results can be illustrated below. The implanted ^{12}B loses its energy by atomic collision in crystal and is finally settled in the substitutional site pushing out the Si atom

to the interstitial site. Then the lattice is compressed by the coulomb attraction between them. Thus formed dumbbell structure is assumed to be the similar one as is predicted by Tarnow. With the thermal energy, the interstitial Si is jumping around the ^{12}B, not the substitutional ^{12}B is jumping. By this jumping, the direction of the field gradients varies its axis.

In the following two sections, the observed relaxation and recovery of the polarization are explained in terms of the atomic jump of this B_{ns} configuration.

5.2 Jumping effect of the atoms

As shown in the previous chapter, it was revealed that the reduction of the observed B_{ns} polarization above 250 K is due to the fast spin-lattice relaxation. In this section, this relaxation will be discussed quantitatively.

The following four processes should be considered as possible cause of the spin-lattice relaxation:

(1) the interaction between the electric quadrupole moment of ^{12}B and a time-varying electric field gradient ($1/T_{1q}$);

(2) the interaction between the magnetic dipole moment of ^{12}B and a time-varying dipole field ($1/T_{1d}$);

(3) the interaction of the ^{12}B with the conduction electron of the host silicon crystal ($1/T_{1e}$);

(4) the trapping of the ^{12}B as it diffuses into the low-symmetry site which has a large paramagnetic field or electric field gradient ($1/T_{1t}$).

Thus the relaxation is expressed by,

$$\frac{1}{T_1} = \frac{1}{T_{1q}} + \frac{1}{T_{1d}} + \frac{1}{T_{1e}} + \frac{1}{T_{1t}}. \tag{5.1}$$

Under the (B_s- Si_i) model of Tarnow, the interstitial Si_i is jumping thermally around the B_s more rapidly with increase of the temperature. This thermal jump is evident from the previous β-NMR studies and our experiment (§ 4.5). This atomic jump leads to the changes of direction of the electric field gradient. Therefore this time-varying electric field gradient [(1)] can be the dominant process for the relaxation.

As for the relaxation due to the time-varying dipole field [(2)], it has negligible contribution to the relaxation, since the ^{29}Si which is the only stable isotope that has a magnetic moment (μ = -0.555 μ_N, $I^\pi = 1/2^+$) has small natural abundance (4.7 %).

Contribution from the conduction electron [(3)] is also negligible. The nuclear polarization relaxation rate of silicon host with n-type dopant due to the conduction electrons is given as [Abr63],

$$\frac{1}{T_{1e}} = \frac{64}{3}\gamma_e^2\gamma_n^2 N\,|\phi(0)|^4\,\sqrt{2\pi m_1 m_2 m_3 kT}, \tag{5.2}$$

where γ_e and γ_n are the gyromagnetic ratios of the electron and the nucleus, respectively, N is the carrier density, $m_1m_2m_3$ is the product of anisotropic effective masses, and $|\phi(0)|^2$ is the electron density at the nucleus. As all the carrier is active above about 100 K, the carrier density is the same as the dopant density in the case of the present experiment. Based on eq.(5.2), the relaxation rate due to conduction electrons for the silicon with the n-type dopant density of 6×10^{14} P/cm^3, which is the typical one used in the present experiment, is estimated as about 1000 seconds. Actually, the relaxation time of about 100 seconds was observed for the ^{29}Si in n-type Si with 10^{14} cm^{-3} dopant density. For the one with 10^{18} cm^{-3} dopant density, the relaxation was about several tens seconds ([SW56]). Similar relaxation time is also expected for the ^{12}B assuming similar electron density at the nucleus, because of the similar gyromagnetic ratio γ_n. Therefore the contribution from conduction electrons cannot be the order of several milli-second observed in the present experiment. In addition, the steep change of relaxation rate as a function of temperature, as seen in Fig.4.15, can not be explained by eq.(5.2) which is proportional to $T^{1/2}$.

Lastly, the trapping mechanism [(4)] will be considered. This process should be possible since the temperature dependence of the relaxation rate of the present results shows a exponential function curve as is typical for a thermal diffusion process. However this trapping mechanism can't explain the NMR-signal enhancement (Fig.4.22) which arises at 200 K and persistent to about 250 K where the relaxation is observed.

Then we will treat the fluctuating quadrupole field [(1)] through the atomic jump as the dominant process of the relaxation. Under the assumption of the (B_s- Si_i) model, using the activation energy E_a and the jumping frequency ν, relaxation rate is expressed as the following equation.

$$\frac{1}{T_1} = \frac{(eqQ)^2}{8\hbar^2}\left\{k_1(\omega_0) + 4k_2(2\omega_0)\right\} + \text{Constant}, \tag{5.3}$$

$$k_1(\omega_0) = \frac{1}{4}\frac{2\tau_c}{1+\omega_0^2\tau_c^2},$$

$$k_2(2\omega_0) = \frac{5}{16}\frac{2\tau}{1+4\omega_0^2\tau_c^2},$$

Table 5.1 Activation energy for the atomic jumping of (B_s - Si_i) pair. (Fit to the polarization data)

Sample number	Dopant (cm^{-3})	Activation energy Ea(eV)	Logarithm of pre-exponent factor $\log_{10}(\nu_0$ (kHz))	Initial polarization (%)	χ^2–Value (normalized)
1	3×10^{14} B	0.46 ± 0.07	9.2 ± 1.1	3.8 ± 0.1	1.4
2	7×10^{17} B	0.49 ± 0.06	9.6 ± 0.9	3.2 ± 0.1	2.8
3	6×10^{14} P	0.47 ± 0.05	9.3 ± 0.6	4.0 ± 0.1	2.4

$$\frac{1}{\tau_c} = \nu \;=\; \nu_0 \exp(-\frac{E_a}{kT}).$$

The observed polarizations with the actual experimental timing program were analyzed by the eq.(5.3) which was deduced in § 2.3.3, since the data on the relaxation rate is not precise enough. The detail of the path of the atomic jump and the fitting function used in the analysis is described in APPENDIX C. As a result, the activation energy E_a and the prefactor ν_0 are obtained as listed in Table 5.1.

As seen in Fig.5.2∼Fig.5.4–(a), the present analysis well reproduces the steep change of the polarization at 275 K ∼325 K. As seen in the solid lines in Fig.5.2∼Fig.5.4–(b), the observed relaxation rates were also well reproduced with the obtained parameters.

In the next step, the $1/T_1$ data obtained from the time development of the polarization are fitted with the function 5.3 to see the consistency. The fitting results are shown in Table 5.2 and the doted line in the Fig.5.2 ∼ Fig.5.4–(b). The actual $1/T_1$ data is almost constant below 200 K, while the above mentioned jumping mechanism predicts continuous steep change. This saturation, however, can be naturally understood by a minor contribution from the interactions with the conduction electron and the fluctuating dipole field *etc.*. So the constant contribution was considered in the actual fitting function.

The results from these two analyses agreed within the error. However, the former analysis is more accurate and reliable because of the statistics. So we take former analysis (Table 5.1).

There is no significant difference between the obtained values for the samples of different type and dopant density. This point is seems to contradict with the results from the old experiments. The activation energy E_a and the prefactor ν_0 are determined

Table 5.2 Activation energy for the atomic jumping of (B_s - Si_i) pair.(Fit to the $1/T_1$ data)

Sample number	Dopant (cm^{-3})	Activation energy Ea(eV)	Logarithm of pre-exponent factor $\log_{10}(\nu_0$ (kHz))	χ^2–Value (normalized)
1	3×10^{14} B	0.37 ± 0.13	7.7 ± 1.4	1.0
2	7×10^{17} B	0.46 ± 0.08	9.6 ± 1.0	0.81
3	6×10^{14} P	0.34 ± 0.06	7.2 ± 0.8	2.2

from the weighted mean of these results for three samples; to be

$$\begin{aligned} E_a &= 0.47 \pm 0.04 \quad \text{eV}, \\ \log_{10}\nu_0 &= 9.4 \pm 0.5 \quad \text{(in kHz)}. \end{aligned} \tag{5.4}$$

This obtained prefactor $\nu_0 = 2.5 \times 10^9$ kHz of the jumping frequency is in agreement with a theoretical value of the effective attempt frequency ($\sim 10^{10}$ kHz [MB93]) or the Debye frequency ($\sim 8 \times 10^{10}$ kHz). The activation energy of 0.47 eV is comparable with the theoretical values of the migration energy for the interstitial Si of 0.5 eV [Has66], 0.4 eV [NVP89], or the sum of the Si interstitial migration energy of 0.5 eV and the extra Coulomb energy of 0.07 eV [Tar91]. These values will be taken up again in section 5.4.

Through ESR experiment, Watkins determined the jumping rate for the $\langle 111 \rangle$ axial symmetry of the B^+ defect as

$$\nu = 5 \times 10^9 \exp(-0.60 \pm 0.05 \ \text{(eV)}/kT) \quad \text{(kHz)}.$$

This rate is shown in Fig.5.5 together with our present experimental rate. The present result shows slightly higher jumping rate compared with the ESR data, although the activation energies and the prefactors are in agreement. This slight deference may show a question in the identification of the sites between the one observed by Watkins [Wat75] and the one by us. This is an open problem in this stage.

We point out that an explanation for the steep decrease of the B_{ns} fraction suggested by Frank *et al.* who made similar β-NMR experiments is wrong [FDE+94]. They measured the temperature dependence of the amplitude of the resonance line at only the higher frequency $\nu_L + \nu_{Qsplit}$ from the B_{ns} nuclei. They found that the amplitude makes a

peak around 300 K. Their interpretation of the increase of the amplitude as the temperature is due to the direction change of the $\langle 111 \rangle$ symmetry associated with the atomic jump, which is correct. As for the steep decrease of the amplitude with the temperature, however, their interpretation is wrong. They explained it by a matter of rf applying technique, *i.e.*, lack of effective rf-applying time compared with a mean residence time τ_c, which becomes shorter as temperature rises. As was made clear in the present study, the diminishing of the maintained polarization in this temperature range is due to the fast spin–lattice relaxation time, not the matter of rf applying technique.

5.3 Recovery of maintained polarization

In this section we will discuss the increasing of the maintained polarization in the temperature range of 450 K $\sim$ 550 K, which was described in the previous chapter.

The experimental results (Fig.4.1, 4.2) shows that all of the polarization produced by the nuclear reaction was fully maintained at the temperature below 275 K and above 550 K. In the intermediate temperature it shows constant quenched polarization ($\sim$50 % of the reaction polarization). As discussed in the previous section the steep polarization change of it around 300 K is due to the fast T_1 for the B_{ns} component associated with the atomic jumps. It is natural to suppose that the increasing polarization at the temperature above 450 K could be due to the vanishing of the cause of this spin–lattice relaxation. Added to it, the recovered polarization is emerged not in the B_{ns} site but in the B_s or the B_x sites.

The discussion will be made based on the assumption of the (B_s-Si_i) pair model, too. The followings seem to be possible cause of this recovery;

(1) the vanishing of the quadrupole effect and the relaxation due to the motional averaging by the rapid atomic motion;

(2) the dissociation of the the (B_s-Si_i) pair.

From the following reason, the motional averaging [(1)] may not be the cause of this recovery. When the frequency of the fluctuation is higher than the Larmor frequency, the relaxation time due to the fluctuating field becomes longer in inverse proportion to the correlation time τ_c, because the destructive Fourier component of the rf field at the Larmor frequency is reduced. So the polarization could be recovered when the motion of the (B_s-Si_i) pair are extremely rapid compared with the Larmor frequency. In this case, because the averaging of the field leads to the narrowing of the resonance line, *i.e.*, the

resonance will no longer show eqQ split lines but appear around the Larmor frequency. This mechanism, if it works, is simple, because the steep decrease and the recovery could both be explained by a single mechanism.

Solid and dotted lines in Fig.5.6 show the polarization change and the relaxation rate $1/T_1$ using the present value of the E_a and the ν_0 determined from analysis of the steep decrease of B_{ns} polarization. This shows that the recovery of the polarization will be observed above ~1000 K, which contradicts the present observation. Consequently, we reject this motional averaging mechanism for the recovery.

Idea of the dissociation of the (B_s-Si_i) pair is quite natural, because the dissociation of the pair leave the substitutional B alone separated from the interstitial Si. Resultant substitutional B naturally shows a resonance at the Larmor frequency if its nuclear polarization still be maintained.

In the following, this dissociation process will be treated quantitatively based on the (B_s-Si_i) pair model. The measured polarization change are fitted to a function considering the thermally induced dissociation rate $\nu_r = \nu_{r0} \exp(-E_r/kT)$ and relaxation of the polarization induced by the atomic jump in the (B_s-Si_i) pair as was made clear in the previous section. The explicit form of the function is described in APPENDIX C. The fitting results are listed in Table 5.3. Though, it was unable to fit the data for the sample no.2 because of the lack of the data at higher temperatures. The difference of the fitting parameters depending on the type and density of the dopant was not seen within the error. So, we determine the activation energy E_r and the prefactor ν_{r0} from the average of these data as

$$\begin{aligned} E_r &= 0.84 \pm 0.06 \quad \text{eV}, \\ \log_{10} \nu_{r0} &= 9.7 \pm 0.5 \quad (\text{in kHz}). \end{aligned} \tag{5.5}$$

As seen in Fig5.7, these parameters well produces the experimental results.

Based on the above mentioned discussion, the outline on the polarization change can be illustrated as follows. Fig.5.8 shows the deduced dissociation rate and the jumping rate of the (B_s-Si_i) pair, and the relaxation rate due to the jumping. Below 275 K, full of the reaction polarization is observed because the relaxation rate due to the jumping are slow compared with the time scale of the nuclear lifetime and hence the β-NMR detection. Above the temperature, the relaxation rate becomes faster and the observed polarization for B_{ns} becomes smaller as the temperature rise, resulting in also the decrease of the total detected polarization. At 325 K, the polarization of B_{ns} totally vanishes. From the temperature up to 450 K, the B_{ns} is not detected. At 450 K, the dissociation rate of the (B_s-Si_i) pair becomes comparable with the relaxation rate, and the fractions of

Table 5.3 Activation energy for the dissociation of (B_s - Si_i) pair.

Sample number	Dopant (cm^{-3})	Activation energy Er(eV)	Logarithm of pre-exponent factor $\log_{10}(\nu_{r0}$ (kHz))	χ^2–Value (normalized)
1	3×10^{14} B	0.80 ± 0.08	9.5 ± 0.6	10.2
3	6×10^{14} P	0.88 ± 0.12	9.9 ± 0.7	5.4

B_s and B_x grow. Above 550 K, the dissociation rate completely overcome the relaxation rate and then all of the reaction polarization is detected as the B_s and/or B_x. Thus, the temperature dependence of the maintained polarization is explained convincingly. It is noted that through out the present temperature range, almost all the ^{12}B implanted in Si, regardless the type and density of the dopant, is suggested to be in diamagnetic states which can be detected by the β-NMR technique, since the total polarization detected is supposed to be close to that in Pt sample all the time.

5.4 On the lattice location of B_{ns}

As described before, the deduced prefactors of the B_{ns} jump rate (eq.(5.4)) and the (B_s-Si_i) pair dissociation rate (eq.(5.5)) are both reasonable value, as they are of the order of 10^{9} kHz which coincides with the order of lattice vibration frequency.

The activation energies of the B_{ns} jump and the the (B_s-Si_i) pair dissociation are listed in Table 5.4 together with the theoretical values of migrations of the self-interstitial and impurities which form defects in Si. The deduced activation energy of the jump is in agreement with the one that was deduced by ESR study within the experimental errors. And the activation energy of about 0.5 eV is almost the same with the theoretical values for the migration energy of the self-interstitial Si. Thus, the atomic jump and the polarization relaxation of B_{ns} can be understood by the migration of interstitial Si around the substitutional B in the (B_s-Si_i) pair model.

The activation energy of the dissociation of (B_s-Si_i) pair shows a slight difference with the one obtained by the Watkins' ESR measurement [Wat75], though the experimental errors of the ESR measurement was not shown. Tarnow gave the lower bound on the barrier of 0.54 eV which is the total energy difference between the initial and final configuration [Tar91]. Also he gave the Coulomb energy of 1.2 eV which is required for

the Si atom to leave the (B_s-Si_i) pair alone. Our activation energy of 0.84 eV for the dissociation is an intermediate value between these two limit, to support the present (B_s-Si_i) pair model.

From what has been said, the behavior of the B_{ns} atom and the temperature dependence of the nuclear polarization is well explained by the (B_s-Si_i) pair model. Although, the present experiment can't exclude the other configuration of the B_{ns} definitely, however, following two points are conclusive;

- the B_{ns} atom migrates between the four identical sites with the rate of $\nu \sim 2.5 \times 10^9 \exp(0.47\text{eV}/kT)$ kHz as deduced in section 5.2,
- the B_{ns} defect dissociates with the rate of $\nu_r \sim 5.0 \times 10^9 \exp(0.84\text{eV}/kT)$ kHz as deduced in section 5.3.

Now, the other candidates for the B_{ns} configuration are considered. Watkins suggested three probable configurations for this B defect [Wat75]; the bond centered site, the interstitial B - substitutional Si pair with slight compression along the $\langle 111 \rangle$ axis, and the hexahedral site.

When the B atom jumps into a Si–Si bond center, the bond should be broken by the B atom. Hence, the activation energy of the jump will be at least the binding energy of the bond, which is about 1.8 eV [Gil80]. Since the present obtained activation energy is too small to break the bond, the bond centered site is unrealistic.

If the other configurations, the interstitial boron or the hexahedral boron, are formed, the migration of the interstitial B will go through the interstitial of the lattice. Since the activation energy of 0.5 eV is typical value for the migration between interstitials as shown in Table 5.4, it cannot reject these configurations cannot be rejected in terms of the activation energy. In these configuration, the recovery of the polarization at higher temperature may be understood by the combination of the interstitial boron and the vacancy.

Of course, the most probable configuration is the (B_s-Si_i) pair as mentioned above, because Tarnow's calculation shows that (Bs-Sii) pair is more stable than the interstitial boron, channeling experiments also denied the undistorted tetrahedral interstitial B, and no reliable microscopic evidence for it has been reported so far.

It may be worth mentioning that ESR studies in aluminum-doped Si had demonstrated that the interstitial aluminum produced by electron irradiation at 20.4 K settles at the undistorted tetrahedral interstitial site and is stable to above 500 K [BL83]. This has been interpreted that the interstitial silicon atom, produced in the primary event, is mobile and kicks the substitutional aluminum atom into the interstitial site. Although

Table 5.4 Comparison of the activation energies E_a for migrations with theories.

	Experimental E_a (eV)	Theoretical E_a (eV)
Jumping (reorientation) of B_{ns} atom	0.47±0.8 (present) 0.60±0.5 [Wat75]	0.5 [Tar91]
Dissociation of the B_{ns}defect	0.84±0.06 (present) 0.6 [Wat75]	> 0.54 [Tar91] (1.2 * [Tar91])
Si Interstitial	-	0.5 [Has66] 0.4 [NVP89]
Si – Vacancy	-	1.1 [Has66] 0.3 [NVP89] 0.7 [D+76]
B interstitial	-	0 [NVP89]
B – Vacancy	-	1.0 [NVP89]
P interstitial	-	0.8 [NVP89]
P – Vacancy	0.94 [HHS69]	-
As interstitial	-	0.4 [NVP89]
As – Vacancy	1.07 [HHS69]	-
Sb interstitial	-	0.2 [NVP89]
Sb – Vacancy	1.28 [HHS69]	-

* The Coulomb energy required for the Si atom to leave alone.

boron and aluminum are the same group-III elements, B prefers forming (B_s-Si_i) pair, while Al prefers (Al_i–Si_s) pair. This is an interesting issue to be solved.

Up to here we discussed about the polarization change of B_{ns} nuclei, we obtain another important information of the electric field gradient q of it. The $|q(B_{ns})|$ is $(1.14\pm0.04)\times10^{17}$ V/cm^2, and η=0.0. The ESR measurements obtained the $|q(B^-)|$ of the $(1.02\pm0.04)\times10^{17}$ V/cm^2, and η=0.18±0.05 [Wat75]. To make sure the configuration of B_{ns}, a theoretical calculation for these field gradients are planned. In APPENDIX B, the electric field gradients of other defects related with impurity are listed.

5.5 On the broad resonance from B_X nuclei

It was disclosed that the broad resonance (~10 kHz) from B_x site is due to static quadrupole interactions with no special symmetry. The fraction of B_x decreases as increasing temperature. From these results, the most probable site for the B_x component is also the substitutional site with small electric field gradient due to crystal defects like vacancies. However, the detail of the character and the cause of this defect need further advanced investigation.

(a) Configuration for B^+.

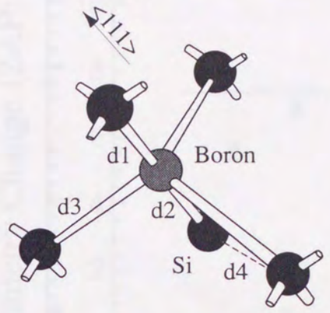

Interatomic distance

(B^+)
d1 = 2.08 Å
d2 = 2.07 Å
d3 = 2.51 Å
d4 = 2.51 Å

(b) Configuration for B^0 and B^-.

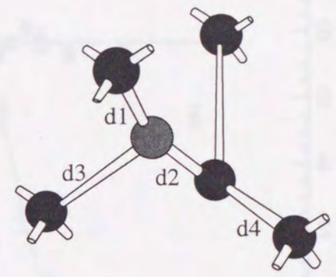

Interatomic distance

(B^0)	(B^-)
d1 = 2.03 Å	d1 = 2.05 Å
d2 = 2.01 Å	d2 = 2.01 Å
d3 = 2.20 Å	d3 = 2.12 Å
d4 = 2.35 Å	d4 = 2.31 Å

(c) Si Lattice

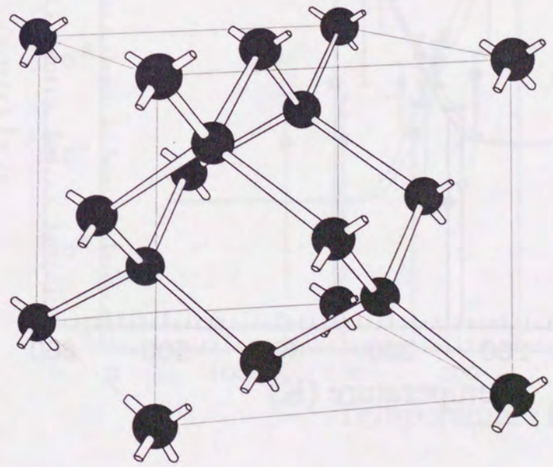

Lattice constant $a = 5.43$ Å

$\left(\frac{\sqrt{3}}{4}a = 2.35\text{Å}\right)$

Figure 5.1 Proposed metastable atomic configurations [Tar91] (a) for positive charge state B^+ in Si, which is almost at the substitutional site combined with an interstitial Si, (b) for neutral and negative charge states. (c) Si lattice (just for a reference).

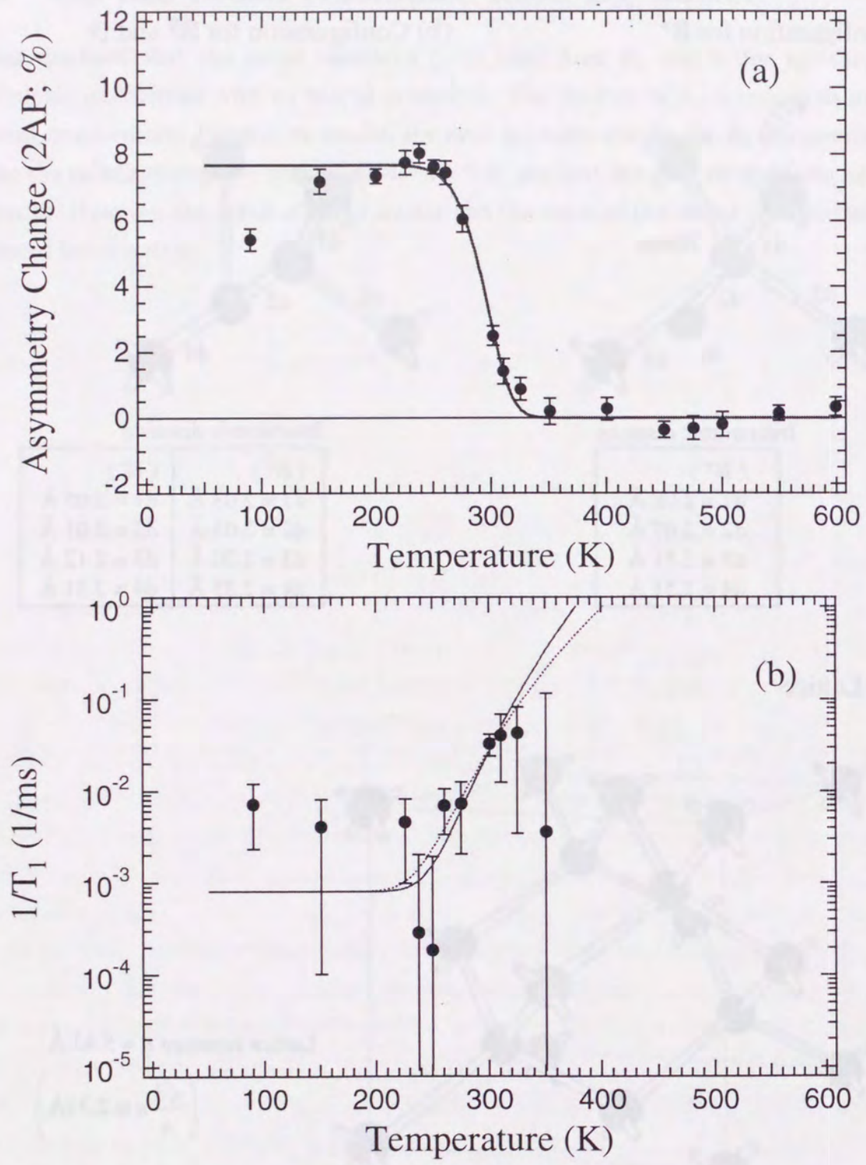

Figure 5.2 The effect of the spin–lattice relaxation time T_1 in p-type Si (3×10^{14} B/cm^3). (a) The best fit line to the observed polarization change within the counting time of 40 ms. (b) The solid line shows the calculated $1/T_1$ as a function of temperature using the activation energy and the prefactor obtained from the fitting of (a). The dotted line is the best fit line to the data of the $1/T_1$ (closed circles) which was deduced in the section 4.4.1.

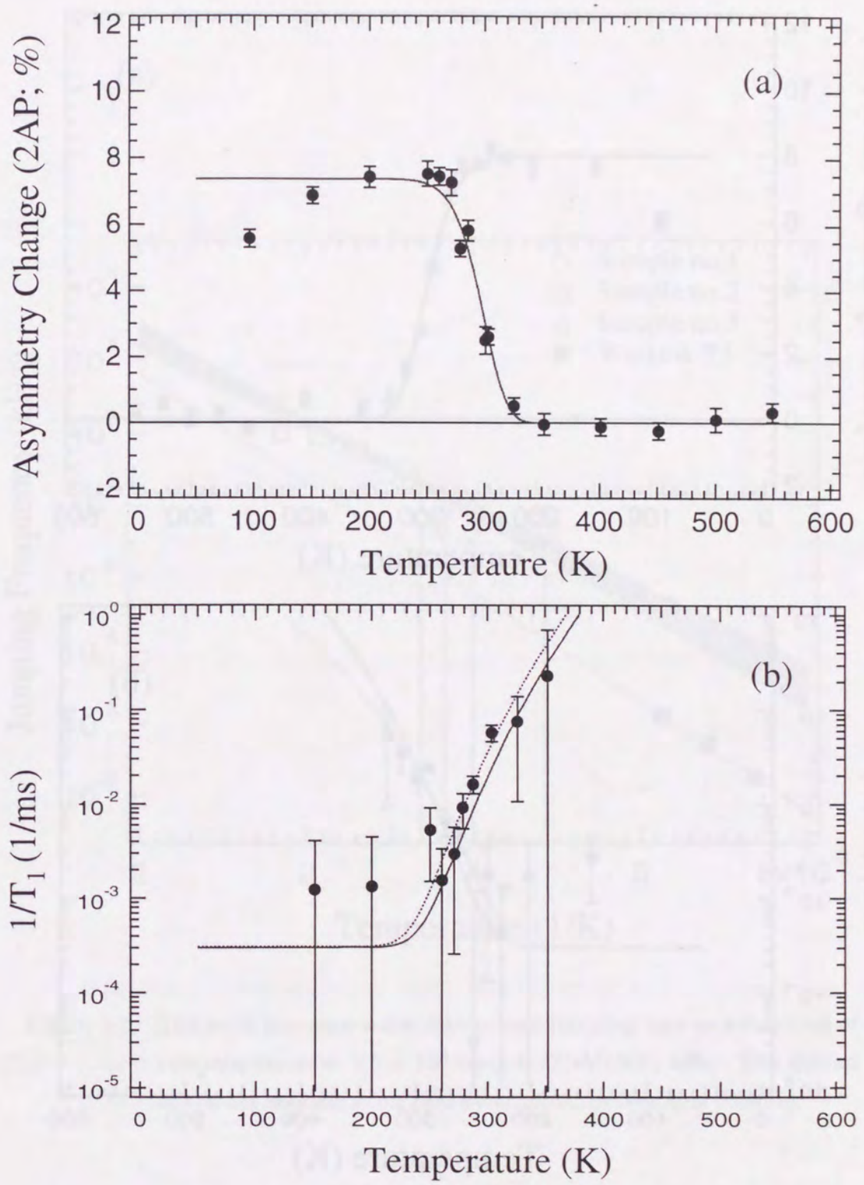

Figure 5.3 The effect of the spin–lattice relaxation time T_1 in p-type Si (7×10^{17} B/cm^3). (a) The best fit line to the observed polarization change within the counting time of 40 ms. (b) The solid line shows the calculated $1/T_1$ as a function of temperature using the activation energy and the prefactor obtained from the fitting of (a). The dotted line is the best fit line to the data of the $1/T_1$ (closed circles) which was deduced in the section 4.4.1.

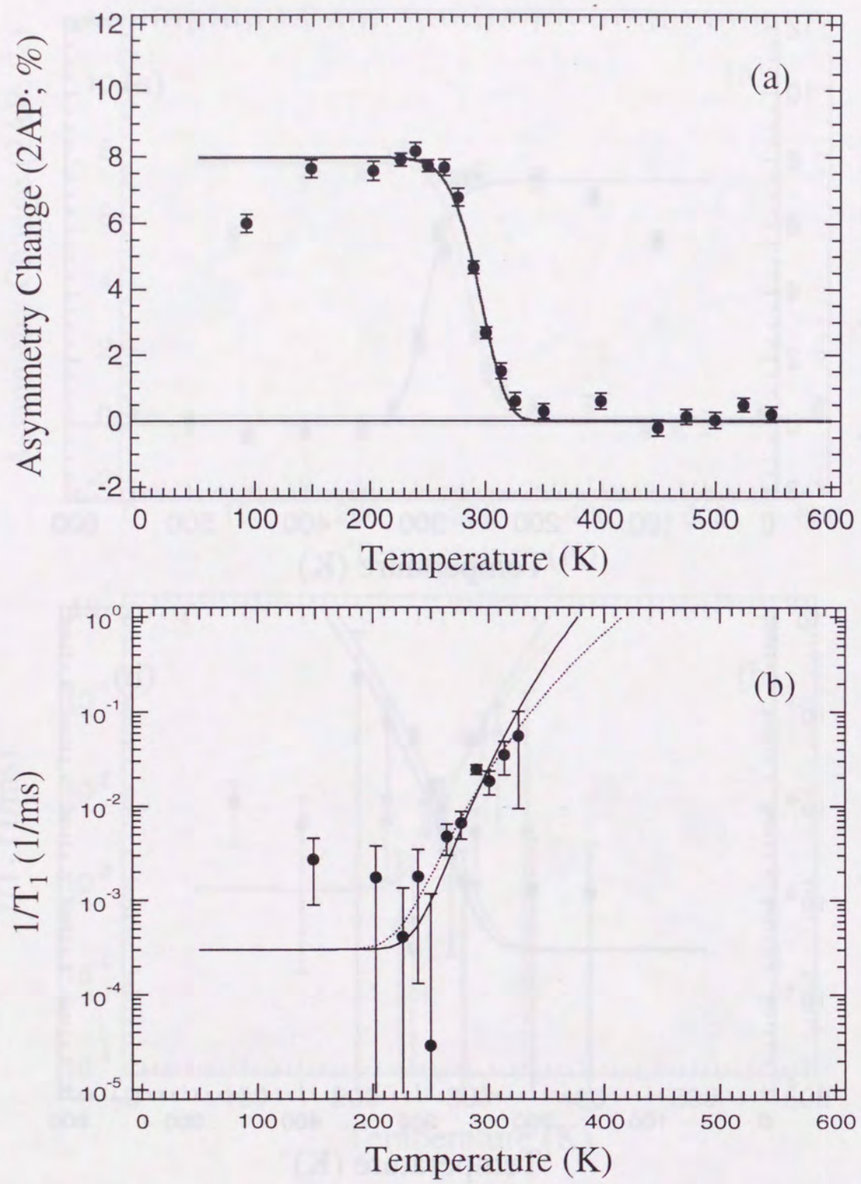

Figure 5.4 The effect of the spin–lattice relaxation time T_1 in n-type Si (6×10^{14} P/cm^3). (a) The best fit line to the observed polarization change within the counting time of 40 ms. (b) The solid line shows the calculated $1/T_1$ as a function of temperature using the activation energy and the prefactor obtained from the fitting of (a). The dotted line is the best fit line to the data of the $1/T_1$ (closed circles) which was deduced in the section 4.4.1.

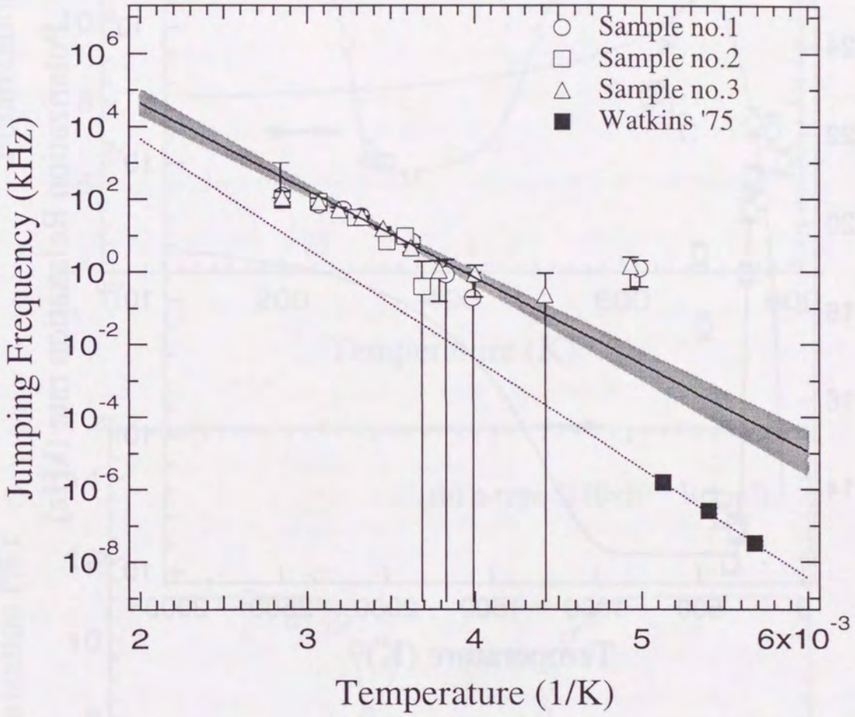

Figure 5.5 The solid line shows the determined jumping rate as a function of temperature $\nu = 2.5 \times 10^9 \exp(-0.47(\mathrm{eV})/kT)$ kHz. The dotted line is the reorientation rate determined by Watkins [Wat75].

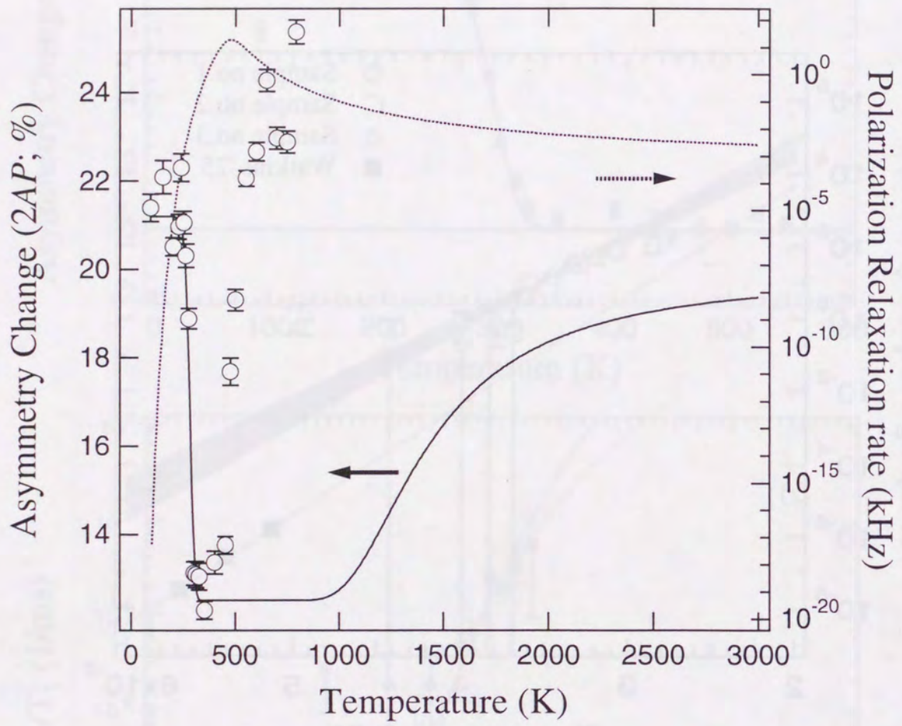

Figure 5.6 The solid line shows the the effect of the motional averaging on the polarization, when the motion obeys $\nu = 2.5 \times 10^9 \exp(-0.47(\mathrm{eV})/kT)$ kHz determined in previous section. The open circles represents the observed polarization. The dotted line is the polarization relaxation rate, just for a reference.

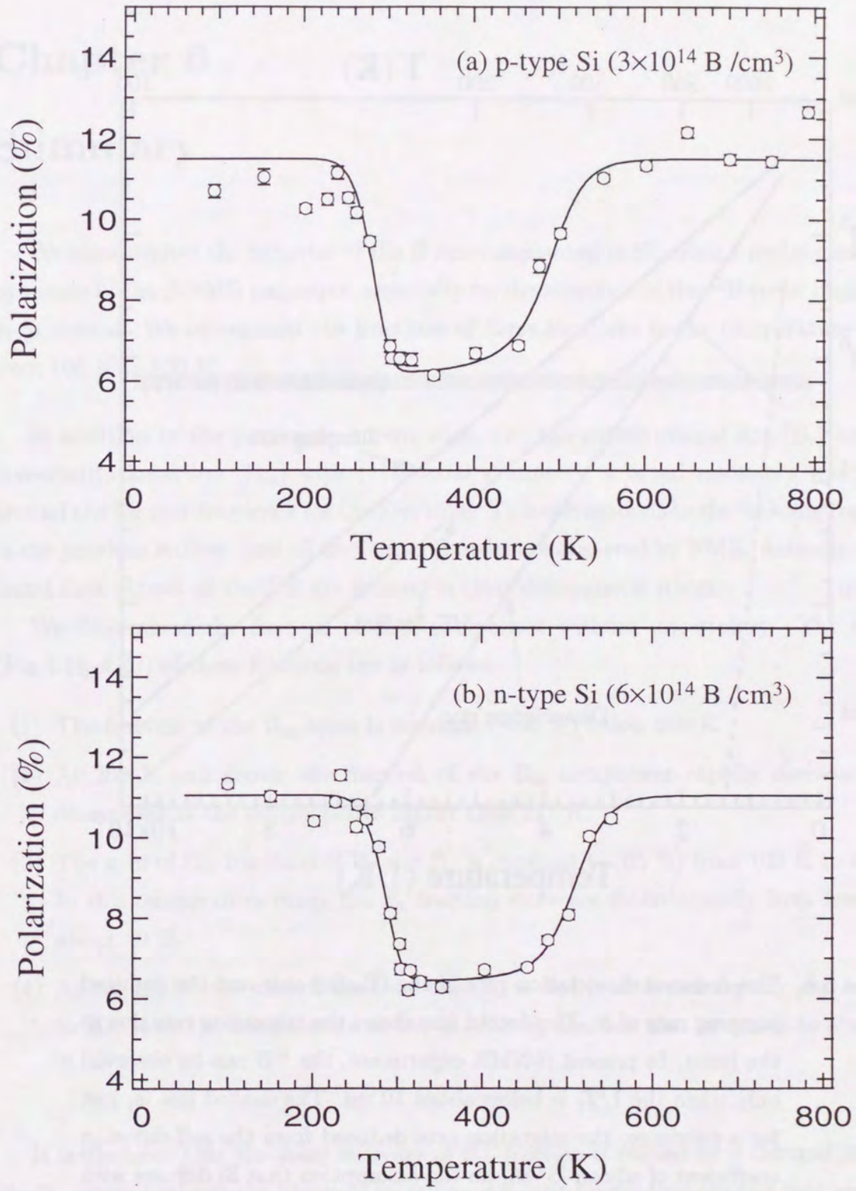

Figure 5.7 The best fit lines to the observed polarization change on the assumption of (B_s-Si_i) pair dissociation. The fitting region is above 320 K. The lines below 320 K are calculated using the values determined in the section 5.1.

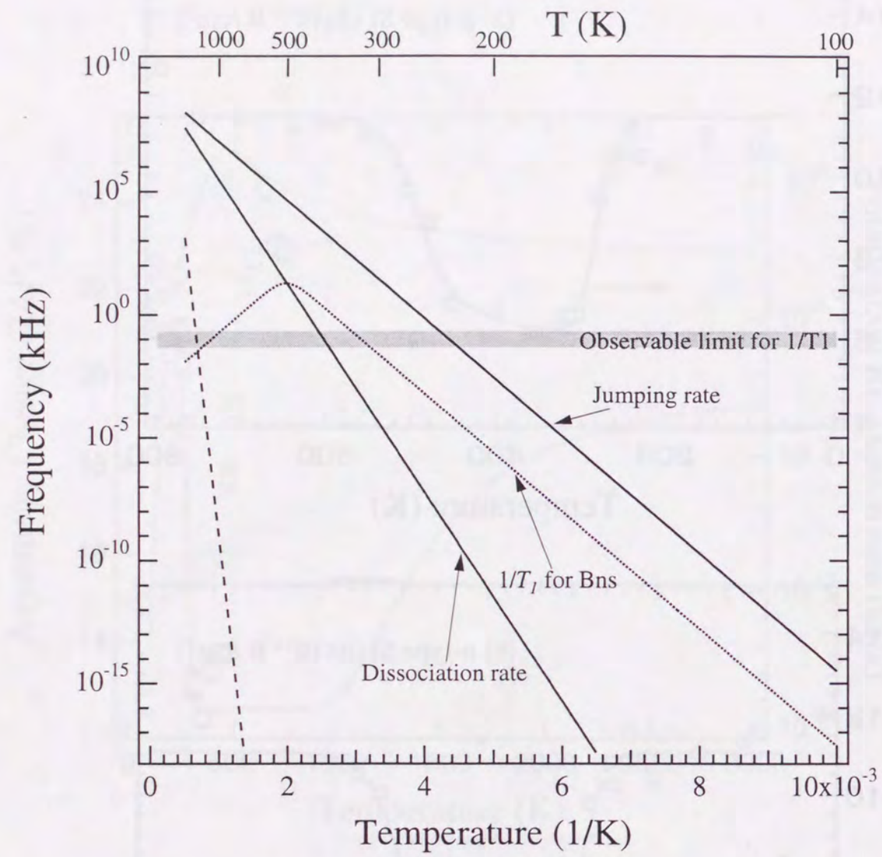

Figure 5.8 The deduced dissociation rate of the (B_s-Si_i) pair and the deduced jumping rate of it. The dotted line shows the relaxation rate due to the jump. In present β-NMR experiment, the ^{12}B can be observed only when the $1/T_1$ is below about 10 ms. The dashed line is, just for a reference, the migration rate deduced from the self-diffusion coefficient of silicon [S$^+$86] on the assumption that Si diffuses with the interstitial mechanism and that its activation energy equals the migration energy itself.

Chapter 6

Summary

We have studied the behavior of the B atom implanted in Si, using a probe nuclei ^{12}B by means of the β-NMR technique, especially on the locations of the ^{12}B recoil implanted in Si crystal. We determined the fractions of three locations in the temperature range from 100 K to 800 K.

In addition to the previously known sites, *i.e.*, the substitutional site (B_s) and the nonsubstitutional site (B_{ns}) with $\langle 111 \rangle$ axial symmetry, a broad resonance was found around the Larmor frequency for the first time. This corresponds to the 'missing fraction' in the previous studies, and all implanted B atom are observed by NMR. Actually it was found that almost all the ^{12}B are located in their diamagnetic states.

We determined the fraction of each component without uncertainty. The results (Fig.4.18–4.20) of these fractions are as follows.

(1) The fraction of the B_{ns} atom is constant (∼35 %) below 260 K.

(2) At 260 K and above, the fraction of the B_{ns} component rapidly decreases and disappears at the temperatures higher than 325 K.

(3) The sum of the fractions of B_s and B_x is constant (∼ 65 %) from 100 K to 450 K. In this temperature range the B_s fraction increases monotonically from few % to about 40 %.

(4) Above 450 K, the sum of the fractions (B_s + B_x) is increases rapidly and reaches to 100 % at the temperature of 550 K. The B_s fraction also increases to about 80 %.

It is disclosed that the steep decrease of B_{ns} fraction is caused by a thermal jump of the B_{ns} atom between the identical locations, *i.e.*, the fluctuating electric field gradient due to the thermal jump causes the fast spin-lattice relaxation of the nuclear polarization of ^{12}B in B_{ns} sites. Assuming the Arrhenius behavior of the thermal jump, the jump rate of the B_{ns} was deduced based on the (B_s- Si_i) pair model for the atomic configuration

which was predicted theoretically to be most probable. The obtained jumping rate is (2.5×10^9) $\exp(-0.47 \pm 0.04(\mathrm{eV})/kT)$ kHz (the error of the pre-exponential factor is $+6\times10^9$, -1.5×10^9). As well as the decrease of the B_{ns} fraction, the recovery of the ^{12}B fraction in the B_s site or the B_x site above 450 K is successfully understood by the dissociation of (B_s- Si_i) pair with the dissociation rate of $5 \times 10^9 \exp(-0.84 \pm 0.06(\mathrm{eV})/kT)$ kHz (the error of the pre-exponential factor is $+1.1\times10^{10}$, -3.5×10^9).

Thus the steep decrease of B_{ns} fraction above 260 K and the polarization recovery around 500 K are consistently explained by the thermal jump and the dissociation within the (B_s- Si_i) pair model.

The electric field gradient q at the B_{ns} site was precisely determined to be $1.14 \pm 0.04 \times 10^{17}$ V/cm^2. In order to make sure the atomic configuration for B_{ns} site, a theoretical calculation based on the KKR method for the energy minimum configuration and for the field gradient is planned.

A new broad resonance line from the B_x site was found to have the two features; (1) a static quadrupole interaction makes the resonance broad, (2) the quadrupole field has no special symmetry axis. As a consequence of these, the most probable site for the B_x component is supposed to be also the substitutional site with small electric field gradient due to crystal defects like vacancies. To clarify what interaction is accompanied with the B_x atom, the cause of this defect should be investigated.

Future prospect

Although it is revealed that the spin-lattice relaxation is caused by the atomic jump of B_{ns}, the lifetime of a probe nuclei restricts the time window for the measurement to several tens milli-second. The ^{8}B($T_{1/2}$= 760 ms, $I^\pi = 2^+$) nuclei is available to measure the relaxation phenomena in the longer time window than the present case of the ^{12}B. The long lifetime of ^{8}B is expected to help to study the atomic jump at higher temperatures.

As the the relaxation time is determined by the relation between the mean residence time and the Larmor frequency, the relaxation time will be changed in accordance with the Larmor frequency which can be controlled by the external magnetic field. That is the β-NMR measurements at different external magnetic fields should be helpful.

As the crystal has four equivalent $\langle 111 \rangle$ axis; $\langle 111 \rangle$, $\langle \bar{1}11 \rangle$, $\langle 1\bar{1}1 \rangle$, and $\langle \bar{1}\bar{1}1 \rangle$, the partial destruction, *e.g.*, the polarization destruction of the B_{ns} nuclei with $\langle 1\bar{1}1 \rangle$ axial symmetry,

the B_{ns} atomic jump can be directly observed as the polarization change in another site with different symmetry. So the experiment with different crystal orientation may be helpful for the clear understanding of the thermal jump for B_{ns}.

In summary, we detected for the first time all the diamagnetic states of the implanted B and revealed a dynamic behavior of the boron related defects. In order for the better understanding of the behavior of B in Si, we extend the present β-NMR study in many directions.

Appendix A

NMR

A.1 Magnetic interaction

The motion of the magnetic moment in a magnetic field can be described by the classical dynamics as follows.

A magnetic moment $\boldsymbol{\mu}$ in a static magnetic field $\boldsymbol{H}_0$ receives the torque $\boldsymbol{\mu} \times \boldsymbol{H}_0$.

This magnetic interaction leads to the precession of $\boldsymbol{\mu}$ around the direction of H_0 with a frequency $\nu_L = \gamma H_0/2\pi$ (*Larmor frequency*), where the gyromagnetic ratio γ is the ratio of the $\boldsymbol{\mu}$ and the angular moment $\boldsymbol{I}\hbar$. Defining z-axis is along the direction of H_0, additional rotating magnetic field $H_1(t)$ is supposed to be applied, *i.e.*,

$$\boldsymbol{H}_1(t) = H_1(\boldsymbol{i}\cos\omega t + \boldsymbol{j}\sin\omega t) \tag{A.1}$$

perpendicular to H_0. In a rotating frame fixed to the rotating field with an angular frequency of ω, the magnetic moment rotates around the effective magnetic field $H_{eff} = \boldsymbol{k}\,(H_0 + \omega/\gamma) + \boldsymbol{i}'\,H_1$ (Fig.A.1). When ω is equal to $-\gamma H_0$, the effective field is just H_1 as shown in Fig.A.1, and the moment will precess around it. As a results, the time averaged expectation value of the magnetic moment along the z-direction becomes zero.

This resonance phenomena can be also understood as follows quantum mechanically. The Hamiltonian of the magnetic moment $\boldsymbol{\mu} = \gamma\hbar\boldsymbol{I}$ is

$$\begin{aligned} \mathcal{H} &= -\boldsymbol{\mu}\cdot\boldsymbol{H}_0 \\ &= -\gamma\hbar H_0 I_z. \end{aligned} \tag{A.2}$$

The eigenstates of this Hamiltonian are split into $2I+1$ levels (Zeeman splitting) with energies;

$$E_m = -\gamma\hbar H_0 m \qquad m = I, I-1, \cdots, -I. \tag{A.3}$$

They are illustrated in Fig.A.2 for the case of $I = 1$, as is in the case of ^{12}B. These energy levels are equally separated with the energy gap of $h\nu_L$.

The transitions between the relevant levels are induced by the rotating magnetic field $\boldsymbol{H}_1(t)$ (Eq. A.1). If the rotating field can be treated as a perturbation $\mathcal{H}_1 = -\gamma\hbar\boldsymbol{H}_1\cdot\boldsymbol{I}$, the transition probability between magnetic substates m and $m+1$ is given as

$$\begin{aligned} W_{m+1,m} &= \frac{2\pi}{\hbar}|\langle m|\mathcal{H}_1|m+1\rangle|^2\delta(E_m - E_{m+1} - \hbar\omega_L) \\ &= \frac{\pi\hbar}{2}\omega_1^2\left\{I(I+1) - m^2 - m\right\}\delta(E_m - E_{m+1} - \hbar\omega_L), \end{aligned} \tag{A.4}$$

where $\omega_1 = -\gamma H_1$. Therefore, when the rotating field with the Larmor frequency is applied to the spins, the probabilities of occupation of both states are equalized.

In a actual experiment, the energy levels spread around the central values, due to spread of the local field originated from the nuclear spin-spin interaction. Therefore, the δ-function in Eq.A.4 has to be replaced by the line shape function $f(\hbar\omega)$.

A.2 Electric quadrupole interaction

In an electric field gradient, a nucleus with the quadrupole moment Q interacts with it in addition to the magnetic interaction. The 3×3 tensor of the electric field gradient, which is the second derivative of the electrostatic potential $V(\boldsymbol{r})$, can be simplified by selecting a principal axes in good symmetries so that off-diagonal components vanishes: $V_{ij} = 0$ for $i \neq j$. Then the Hamiltonian of the electric quadrupole interaction is given as

$$H_Q = \frac{eQ}{4I(2I-1)}[V_{ZZ}(3I_Z^2 - \boldsymbol{I}^2 + \frac{1}{2}(V_{XX} - V_{YY})(I_+^2 + I_-^2)] \tag{A.5}$$

$$= \frac{eqQ}{4I(2I-1)}[3I_Z^2 - \boldsymbol{I}^2 + \frac{\eta}{2}(I_+^2 + I_-^2)]. \tag{A.6}$$

Here, the asymmetry parameter η and the largest component of the field gradient q are defined as

$$eq = V_{ZZ} \tag{A.7}$$

$$\eta = \frac{V_{XX} - V_{YY}}{V_{ZZ}} \tag{A.8}$$

$$|V_{XX}| \leq |V_{YY}| \leq |V_{ZZ}|. \tag{A.9}$$

In the present study where high field H_0 was employed, this quadrupole interaction can be treated as a perturbation to the magnetic interaction, since $eqQ \ll \mu H_0$. In order to derive the perturbation energies, the perturbation Hamiltonian H_Q is expressed in

the coordinate system with the z axis parallel to H_0. Using the Euler angles defined in Fig.A.3:

$$\begin{aligned} H_Q = \frac{h\nu_Q}{4}\Big[&\left\{I_z^2 - \frac{1}{3}I(I+1)\right\}\left\{3\cos^2\theta - 1 + \eta\cos 2\phi\sin^2\theta\right\} \\ &+ \left(\frac{1}{2}\sin 2\theta - \frac{\eta}{6}\cos 2\phi\sin 2\theta + \imath\frac{\eta}{3}\sin 2\phi\sin\theta\right)(I_+I_z + I_zI_+) \\ &+ \left(\frac{1}{2}\sin 2\theta - \frac{\eta}{6}\cos 2\phi\sin 2\theta - \imath\frac{\eta}{3}\sin 2\phi\sin\theta\right)(I_-I_z + I_zI_-) \\ &+ \left(\frac{1}{2}\sin^2\theta + \frac{\eta}{6}\cos 2\phi\left(1+\cos^2\theta\right) - \imath\frac{\eta}{3}\sin 2\phi\cos\theta\right)I_+^2 \\ &+ \left(\frac{1}{2}\sin^2\theta + \frac{\eta}{6}\cos 2\phi\left(1+\cos^2\theta\right) + \imath\frac{\eta}{3}\sin 2\phi\cos\theta\right)I_-^2\Big], \end{aligned} \tag{A.10}$$

where $\nu_Q = \frac{3eqQ}{2I(2I-1)h}$ is the coupling frequency of the quadrupole interaction. By means of the first and the second order perturbation theory, the energy levels of the magnetic substates are given as

$$E_m = E_m^{(0)} + E_m^{(1)} + E_m(2) + \cdots \tag{A.11}$$

$$E_m^{(0)} = -h\nu_L m \tag{A.12}$$

$$E_m^{(1)} = \frac{1}{4}h\nu_Q(3\cos^2\theta - 1 + \eta\cos 2\phi\sin^2\theta)\left(m^2 - \frac{1}{3}I(I+1)\right) \tag{A.13}$$

$$\begin{aligned} E_m^{(2)} = -\frac{h\nu_Q^2}{16\nu_L}m\Big[&2B\left(-2m^2 + 2I(I+1) - 1\right) \\ &+C\left(8m^2 - 4I(I+1) + 1\right)\Big]. \end{aligned} \tag{A.14}$$

Here,

$$B = \left(\frac{3}{4}\sin^2\theta + \frac{\eta}{4}(\cos^2\theta + 1)\cos 2\phi\right)^2 + \left(\frac{\eta}{2}\cos\theta\sin 2\phi\right)^2$$

$$C = \left(\frac{3}{4}\sin 2\theta - \frac{\eta}{4}\sin 2\theta\cos 2\phi\right)^2 + \left(\frac{\eta}{2}\sin\theta\sin 2\phi\right)^2. \tag{A.15}$$

The effect of the quadrupole interaction is shown in Fig.A.4 for the case of a spin $I = 1$. The transition frequency between m and $m+1$ is shifted by about ΔE which is proportional to m from the Larmor frequency. As a consequence the $2I$ resonances lines are observed.

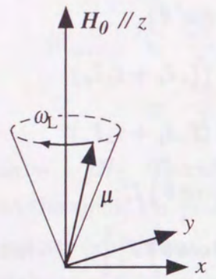

A magnetic moment precesses along the external magnetic field H_0 with the Larmor frequency.
($\omega_L = -\gamma H_0$)

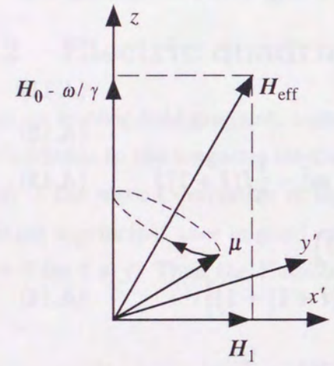

The effective magnetic field and the Larmor precession in the rotating frame fixed to the rotating field H_1 with the angular velocity ω.

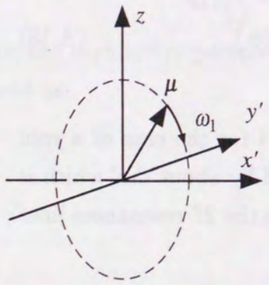

The precession at the $\omega = \omega_L$.
The magnetic moment rotates in the $y'z$ plane with the angular velocity $\omega_1 = -\gamma H_1$.

Figure A.1 The motion of a magnetic moment.

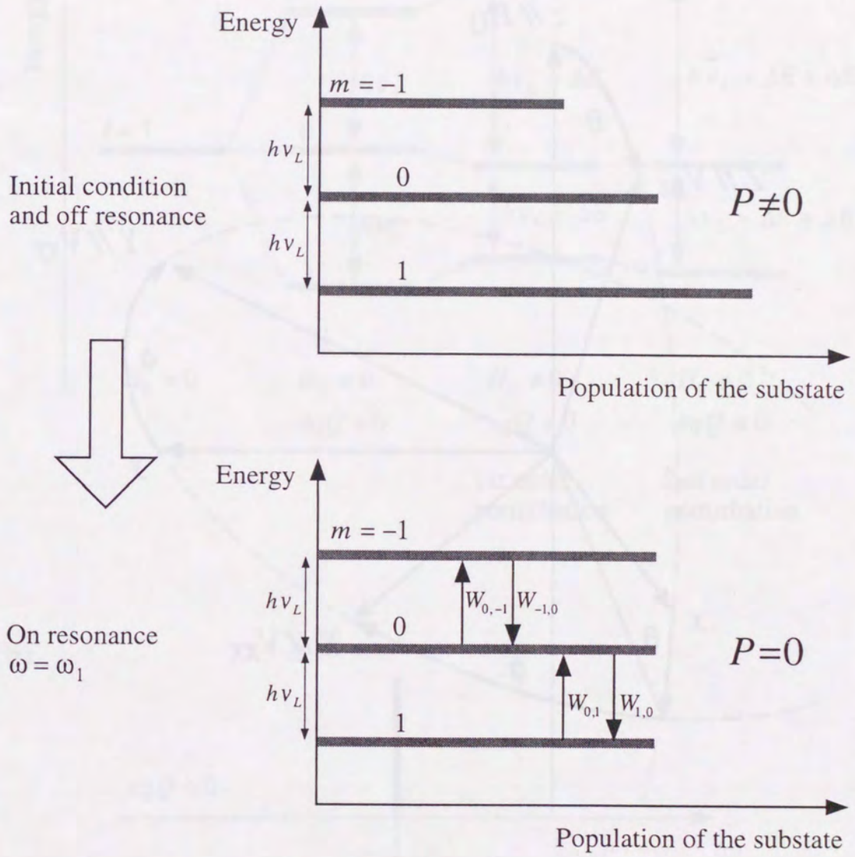

Figure A.2 The energy levels for $I = 1$ nuclear spin ensemble.
At the on resonance condition, the relevant transitions between the substates are induced, and all of the populations are equalized.
The polarization is defined by $P = \frac{\langle I_z \rangle}{I}$.

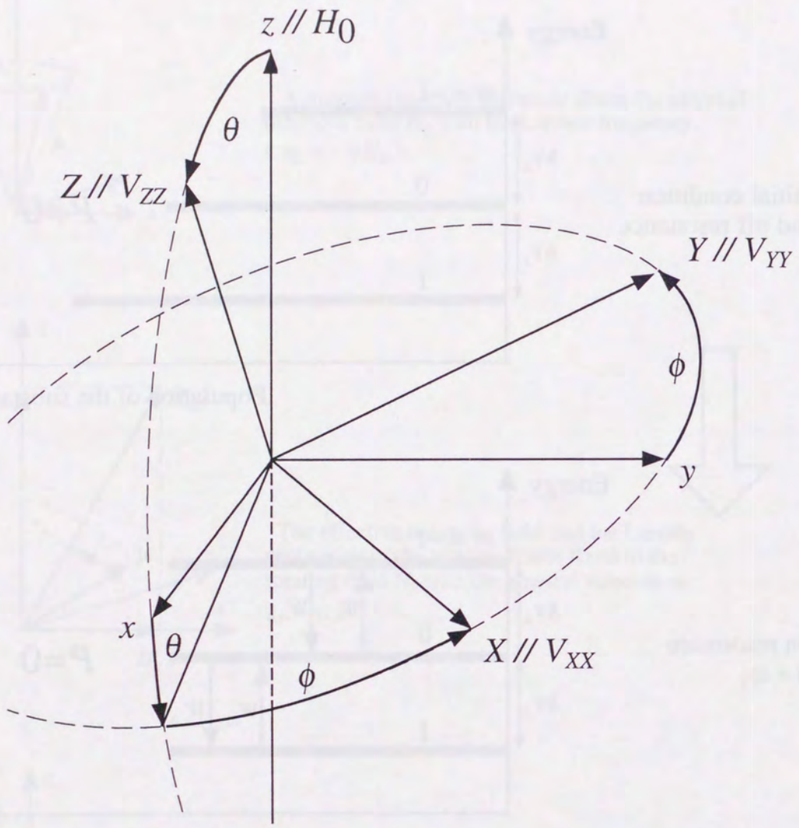

Figure A.3 Euler angle rotations.

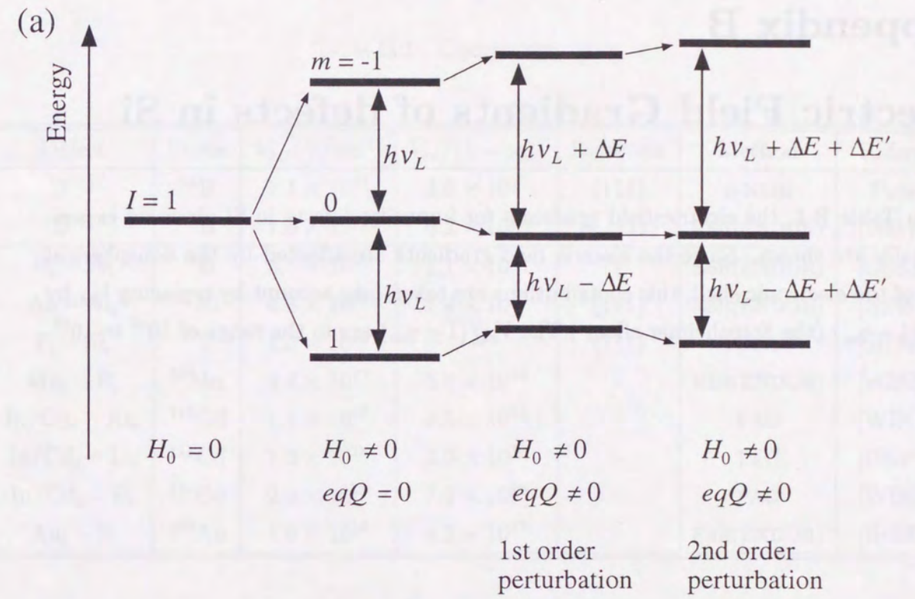

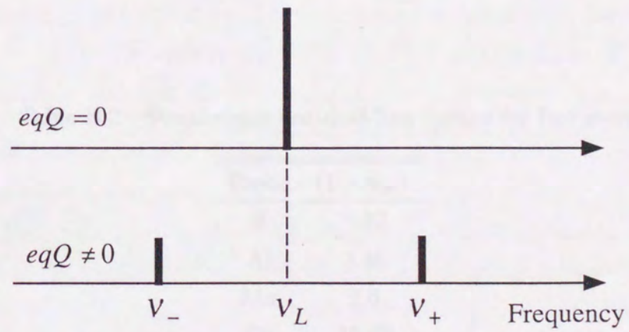

Figure A.4 Energy and transition-frequency shifts for the case of $I = 1$ caused by the quadrupole effect in high field.

Appendix B

Electric Field Gradients of defects in Si

In Table B.1, the electric field gradients for impurity-defects in Si observed experimentally are shown. Since the electric field gradients are affected by the nonspherical part of the electronic shell, this contributions are taken into account by replacing V_{zz} by $V_{zz}/(1-\gamma_\infty)$ (the Sternheimer effect).The $V_{zz}/(1-\gamma_\infty)$ are in the range of 10^{16} to 10^{18}.

Table B.1 Comparison of q.

Defect	Probe	V_{zz} (V/cm^2)	$V_{zz}/(1-\gamma_\infty)$	Direction	Method	Reference
$B^{(+)}$	^{12}B	1.1×10^{17}	3.6×10^{17}	$\langle 111 \rangle$	β-NMR	Present
$B^{(0)}$	^{11}B	1.0×10^{17}	3.2×10^{17}	$\sim \langle 111 \rangle$	ESR(ENDOR)	[Wat75]
$B_s - Fe_i$	^{11}B	3.5×10^{16}	1.1×10^{17}	-	ESR(ENDOR)	[GS83]
$Al_i - Al_s$	^{27}Al	4.8×10^{16}	1.4×10^{16}	$\langle 111 \rangle$	ESR(ENDOR)	[NSW85]
$F_i - Si_s$	^{19}F	1.3×10^{18}	–	$\langle 111 \rangle$	TDPAD	[SHM95]
$Mn_i - B_s$	^{55}Mn	4.4×10^{17}	5.8×10^{16}	-	ESR(ENDOR)	[kG82]
$In/Cd_s - As_s$	^{111}Cd	1.1×10^{18}	3.5×10^{16}	-	PAC	[WDG$^+$89]
$In/Cd_s - Li_i$	^{111}Cd	1.2×10^{18}	3.9×10^{16}	-	PAC	[DKP$^+$89]
$In/Cd_s - H_i$	^{111}Cd	2.2×10^{18}	7.2×10^{16}	-	PAC	[WDG$^+$89]
$Au_i - Si$	^{197}Au	1.6×10^{19}	4.2×10^{17}	-	ESR(ENDOR)	[Hoh86]

Table B.2 Sternheimer antishielding factors for free atoms

Probe	$(1-\gamma_\infty)$.
B	0.32
Al	3.46
Mn	7.6
Cd	30.27
Au	39.14

Appendix C

Fitting Functions

In this section, we will describe the experimental fitting functions for the polarization relaxation due to fluctuating electric field gradients.

The general formula for the polarization relaxation rate were obtained as equations (2.35) and (2.36) in § 2.3.3. For the special case of spin $I = 1$ nuclei, the eq.(2.35) can be simplified as

$$\frac{1}{T_1} = \frac{(eqQ)^2}{8\hbar}\left\{k_1(\omega_0) + 4k_2(2\omega_0)\right\}. \tag{2.37}$$

The correlation function $k_q(\omega_q)$ depends on a specific model of the fluctuation. For the analysis of the present experimental results, the correlation function were calculated on the assumption of the (B_s- Si_i) pair model.

In this model, there are four identical sites corresponding to the four direction of the $\langle 111\rangle$ axes, *i.e.*, $\langle 111\rangle$, $\langle \bar{1}11\rangle$, $\langle 1\bar{1}1\rangle$, and $\langle \bar{1}\bar{1}1\rangle$. For the explanation, we label the site with $\langle 111\rangle$ axial symmetry as A, in the same manner, B for $\langle \bar{1}11\rangle$,C for $\langle 1\bar{1}1\rangle$, and D for $\langle \bar{1}\bar{1}1\rangle$. The fluctuation is caused by the jumping of the Si_i atom from a $\langle 111\rangle$ axial symmetry site to other $\langle 111\rangle$ axial symmetry site through hexagonal interstitial sites. Therefore the atom jumps from A to B (or C, D), not from A to A.

Assuming each jump obeys the Poisson process with the mean occurrence of $1/\bar{\tau}_c$, the probability for n times of events in a period τ represent as

$$w_n(\tau) = \frac{1}{n!}\left(\frac{\tau}{\tau_c}\right)^n \mathrm{e}\left(-\frac{\tau}{\tau_c}\right). \tag{C.1}$$

Therefore, when the atom is in site A at $t = 0$, the probability for the atom to be in the same site A after $t = \tau$ is

$$P_A(\tau) = \sum_{n=1}^{\infty} w_n(\tau) P_{A,n}. \tag{C.2}$$

Here, the $P_{A,n}$ is the probability that the atom is still in the same site A after n jumps, which is calculated in this case as

$$P_{A,n} = \frac{1}{4}\left[1 + 3\left(-\frac{1}{3}\right)^n\right]. \tag{C.3}$$

In the same manner, the probability for the atom to be in another site B at $t = \tau$ is

$$P_B(\tau) = \sum_{n=1}^{\infty} w_n(\tau) P_{B,n}, \tag{C.4}$$

$$P_{B,n} = \frac{1}{4}\left[1 - \left(-\frac{1}{3}\right)^n\right]. \tag{C.5}$$

Then we can calculate the correlation function for this case using eq.(2.38) as

$$k_1(\omega_0) = \frac{1}{4}\frac{2\tau}{1+\omega_0^2\tau_c^2}, \tag{2.41}$$

$$k_2(2\omega_0) = \frac{5}{16}\frac{2\tau}{1+4\omega_0^2\tau_c^2}. \tag{2.42}$$

Fitting Function for the jumping effect

The relaxation rate Λ due to the fluctuating field is,

$$\Lambda = \frac{1}{T_1} = \frac{(eqQ)^2}{8\hbar^2}\left\{k_1(\omega_0) + 4k_2(2\omega_0)\right\} + K(\text{Constant}), \tag{C.6}$$

$$k_1(\omega_0) = \frac{1}{4}\frac{2\tau_c}{1+\omega_0^2\tau_c^2}, \tag{C.7}$$

$$k_2(2\omega_0) = \frac{5}{16}\frac{2\tau}{1+4\omega_0^2\tau_c^2}, \tag{C.8}$$

$$\frac{1}{\tau_c} = \nu = \nu_0 \exp(-\frac{E_a}{kT}). \tag{C.9}$$

Here, the constant K in the relaxation rate Λ is for the contribution from the other cause than the preset fluctuating electric field gradient. This is a fitting function used in the analysis of the polarization relaxation.

For the calculation of the actually observed average polarization change in the β-ray counting period, the correction due to the relaxation is necessary for the actual timing program of the β-NMR detection. Thus, the observed polarization is given as

$$\Delta P = \frac{P_0\lambda^2(1-\mathrm{e}^{-(\Lambda+\lambda)t_1})(1-\mathrm{e}^{-(\Lambda+\lambda)t})\mathrm{e}^{-\Lambda t_2}}{(\Lambda+\lambda)^2(1-\mathrm{e}^{-\lambda t_1})(1-\mathrm{e}^{-\lambda t})}, \tag{C.10}$$

where Λ is the polarization relaxation rate, λ is the nuclear decay rate, P_0 is the initial polarization at the production time, t_1 is the beam bombardment time, t_2 is the rf time, and t is counting time.

Fitting Function for the dissociation of (B_S - Si_i) pair

For the analysis of the the dissociation of (B_s- Si_i) pair, different correction is necessary because the polarization is kept after the dissociation. So, the function for average polarization taking into account of the dissociation rate ν_r is given as

$$\Delta P = \frac{P_0\lambda^2\Lambda(1-e^{-(\Lambda+\lambda+\nu_r)t_1})(1-e^{-(\Lambda+\lambda+\nu_r)t})e^{-(\Lambda+\lambda)t_2}}{(\Lambda+\lambda+\nu_r)^2(\Lambda+\lambda)(1-e^{-\lambda t_1})(1-e^{-\lambda t})e^{-\lambda t_2}} + \frac{\nu_r}{\Lambda+\nu_r}, \qquad \text{(C.11)}$$

where, ν_r is the dissociation rate of (B_s- Si_i) pair, ν_r=ν_{r0}e$(-E_r/kT)$. E_r is the activation energy and ν_{r0} is the prefactor of the thermal dissociation, the rest of the symbols are same as used in eq.(C.10).

Appendix D

Computer control program lists

We list computer programs for β-NMR and β-NQR method. These program are written by machine language MASM (macro assembler) for the 80286 CPU. They contain two part, main programs and macro libraries.

Table D.1 List of computer programs

File Name	Experimental mode
2APCNTRF.ASM	β-NMR
2APCNTRZ.ASM	β-NQR (5 rf repetitions)
2APCNTRI.ASM	β-NQR (1 rf repetition)
LIFCNTR.ASM	Time spectrum
LAB1CNTR.ASM	macro library
LAB2CNTR.ASM	macro library
IOCNTR.ASM	macro library

2APCNTRF.ASM

```
;       NMR測定実験制御
;
;       2AP MODE
;
;       2APCNTRF.M
; for camac scaler
        .sall
        title 2APCNTRF Main routine
        %out Now 2APCNTRF.ASM has
 been compiled
;
;       初期設定部インクルード
;
        include "lab"lab1cntr.asm
;
        ctadinc 3Ch
;
main:
st sem
        bpcntr  bmport,bmstart,off,lpulse
        rfdtout adrfdt
        wtloopl bmtime1,bmtime2
        bpcntr  bmport,bmstop,off,lpulse
in sem adctsem, ctch5
;
        bmcool
;
        rfcntr  rfon,rfoff,rftime1,rftime2
        rfkill
;
        count   00000001b,01h,04h,cttime3,cttime4
countin
        count   10000001b,01h,04h,cttime3,cttime4
        countin
        count   00000010b,01h,04h,cttime3,cttime4
        countin
        count   10000010b,01h,04h,cttime3,cttime4
        countin
        count   00010000b,01h,04h,cttime3,cttime4
        countin
        count   01010000b,01h,04h,cttime3,cttime4
        countin
        count   10010000b,01h,04h,cttime3,cttime4
        countin
        count   11010000b,01h,04h,cttime3,cttime4
        countin
        count   00000100b,01h,04h,cttime1,cttime2
countin
        count   10000100b,01h,04h,cttime1,cttime2
        countin
        count   00001000b,01h,04h,cttime1,cttime2
        countin
        count   10001000b,01h,04h,cttime1,cttime2
        countin
        count   00100000b,01h,04h,cttime1,cttime2
        countin
        count   01100000b,01h,04h,cttime1,cttime2
        countin
        count   10100000b,01h,04h,cttime1,cttime2
        countin
        count   11100000b,01h,04h,cttime1,cttime2
        countin
;
        rfadinc
        bpcntr  ctport,workend,off,lpulse
;
        dec     cx
        jcxz    extgl
        jmp     main
;
extgl:
;
;       終了処理部インクルード
;
        include "lab"lab2cntr.asm
;
        end
```

2APCNTRZ.ASM

```
;       NMR測定実験制御
;
;       2RF 2AP MODE (RF ON / OFF)
; RF 1,2 * 5 (3,4 are dummy)
; used by Frequency synsesizer
;
        2RF-2AP using frequency synsesizer
;
; RF data for '4RF 2AP MODE' can be used.
; Please set dummy data for No. 3 and 4 RF.
;
        2APCNTRZ.M
;
; by Moichi
;
                        modified by A.K.     1991/11/08
; This is the my Last
control program
; for LABCNTR system.
;
; for camac scaler
        title 2APCNTRZ Main routine
if1
        %out Now 2APCNTRZ.ASM has been compiled
endif
;
;       初期設定部インクルード
;
        include lab"lab1cntr.asm
;
        ctadinc 04h.
;
main:
st sem
        bpcntr  bmport,bmstart,off,lpulse
        wtloopl bmtime1,bmtime2
        bpcntr  bmport,bmstop,off,lpulse
        in sem  adctsem,ctch5
;
        bmcool
;
        bpcntr  rfport,rfon,rfon,lpulse
        push cx
mov cx,005h ; for 5 rf loop
rflp1: push cx
        rfdtout adrfdt
bpcntr rfport,045h,004h,lpulse
; select RG1  0100 0101
        wtloopl rftime1,rftime2
        rfadinc

        rfdtout adrfdt
bpcntr rfport,025h,004h,lpulse
; select RG2  0010 0101
        wtloopl rftime1,rftime2

        rfadinc

        rfadinc

pop cx
dec cx
jcxz cont1
rfaddec3
jmp rflp1
cont1: pop cx
        bpcntr  rfport,rfoff,rfoff,lpulse
        rfkill
;
;       count   00000001b,01h,3ch,cttime1,cttime2
        count   00000001b,01h,40h,cttime1,cttime2

        countin

        rfadinc

;
        dec     cx
        jcxz    extgl
        jmp     main
;
extgl:
;
;       終了処理部インクルード
;
        include lab"lab2cntr.asm
;
        end
```

2APCNTRI.ASM

```
;       NMR測定実験制御
;
;       2RF 2AP MODE (RF ON) 16sections
; RF 1,2  (3,4 are dummy)
; used by Frequency synsesizer
;
        2RF-2AP using frequency synsesizer
;
; RF data for '4RF 2AP MODE' can be used.
; Please set dummy data for No. 3 and 4 RF.
;
        2APCNTRI.M
;
; by Moichi
;
                        modified by A.K.     1991/11/08
; This is the my Last control program
; for LABCNTR system.
;     modified by Miyake. '93 X'mas Eve
;     modified by Miyake. '94 / 06/ 11
;
; for camac scaler 94/11/25
        title 2APCNTRI Main routine
if1
        %out Now 2APCNTRI.ASM has been compiled
endif
;
;       初期設定部インクルード
;
        include lab"lab1cntr.asm
;
        ctadinc 3Ch

;main:
st sem
        bpcntr  bmport,bmstart,off,lpulse
        wtloopl bmtime1,bmtime2
        bpcntr  bmport,bmstop,off,lpulse
        in sem  adctsem,ctch5
;
        bmcool
;
        bpcntr  rfport,rfon,rfon,lpulse
        rfdtout adrfdt
bpcntr rfport,045h,004h,lpulse
; select RG1  0100 0101
        wtloopl rftime1,rftime2
        rfadinc

        rfdtout adrfdt
bpcntr rfport,025h,004h,lpulse
; select RG2  0010 0101
        wtloopl rftime1,rftime2

        rfadinc

        rfadinc

        bpcntr  rfport,rfoff,rfoff,lpulse
        rfkill
;
        count   00000001b,01h,04h,cttime1,cttime2
        countin
        count   00000010b,01h,04h,cttime1,cttime2
        countin
        count   00000011b,01h,04h,cttime1,cttime2
        countin
        count   00000100b,01h,04h,cttime1,cttime2
        countin
        count   00000101b,01h,04h,cttime1,cttime2
        countin
        count   00000110b,01h,04h,cttime1,cttime2
        countin
        count   00000111b,01h,04h,cttime1,cttime2
        countin
        count   00001000b,01h,04h,cttime1,cttime2
        countin
        count   00001001b,01h,04h,cttime3,cttime4
        countin
        count   00001010b,01h,04h,cttime3,cttime4
        countin
        count   00001011b,01h,04h,cttime3,cttime4
        countin
        count   00001100b,01h,04h,cttime3,cttime4
        countin
        count   00001101b,01h,04h,cttime3,cttime4
        countin
        count   00001110b,01h,04h,cttime3,cttime4
        countin
        count   00001111b,01h,04h,cttime3,cttime4
        countin
        count   00010000b,01h,04h,cttime3,cttime4
        countin

        rfadinc

;
        dec     cx
        jcxz    extgl
        jmp     main
;
extgl:
;
;       終了処理部インクルード
;
        include lab"lab2cntr.asm
;
        end
```

LIFCNTR.ASM

```
;       NMR測定実験制御
;
;       life time
;
;       LIFCNTR .M
;
; 1994/11/30 BEAM * 2ch by T.M
; 1994/11/30 to use CAMAC by T.M
;
        .sall
        title LIFCNTR Main routine
if1
        %out Now LIFCNTR .ASM has been compiled
endif
;
;       初期設定部インクルード
;
        include lab"lab1cntr.asm
;
main:
        st beam
        bpcntr  bmport,bmstart,off,lpulse
        rfdtout adrfdt
        wtloopl bmtime1,bmtime2
        bpcntr  bmport,bmstop,off,lpulse
        in beam  adctsem,ctch5,ctch6
;
        bmcool
;
cloop:
        count   00010000b,01h,40h,cttime1,cttime2
        countin
;
        dec     cx
        jcxz    extgl
        jmp     cloop
;
extgl:
        bpcntr  ctport,workend,off,lpulse
;
;       終了処理部インクルード
;
        include lab"lab2cntr.asm
;
        end
```


LAB1CNTR.ASM

```
;
;       実験制御プログラム　初期設定ルーチン
;
;       for controller NEC PC9801VX
;
; 1991/01/25 by A.Kitagawa
;
; 1994.01.25 to use WAVETEK
modified by T.Miyake
; 1994.11.30 to use CAMAC modified by T.M
; 1995.10.12 modified WAVETEK control
;
if1
        %out    LABCNTR   v.11.10 l.01
endif
if2
        %out path2
endif
;
;=====================
;
;       インターフェイス　ポートアドレス
;
inport  equ     01ad0h          ; I／Oポート
bmport  equ     01ad4h          ;
rfport  equ     01ad2h          ;
ctport  equ     01ad4h          ;
pt1ctr  equ     01ad6h          ;
rfbitpl equ     01ad8h          ;
rfbitph equ     01adah          ;
secport equ     01adch          ;
pt2ctr  equ     01adeh          ;
;
synthe equ 20d4h
synt01  equ     020d2h          ; シンセサイザー用
synt10  equ     020dch          ;       I／Oポート
synt1k  equ     020dah          ;
synt100k equ    020d8h          ;
synt10m equ     020d0h          ;
syntstr equ     020d4h          ;
;
SCALLER1 equ 8
SCALLER2 equ 8
open equ 0ffh
hold equ 00h
rddt equ 0h
;
datalow equ 0D0h
datahi equ 0D2h
nacmnd equ 0D4h
contrl equ 0D6h
camacgo equ 0D7h
status equ 0D6h
;
; camac controll bit
;
c line equ 00000001b
i line equ 00000100b
done equ 00010000b
lint ei i equ 10001100b
lint ei equ 10001000b
;
ctch1   equ     0h
ctch2   equ     1h
ctch3   equ     2h
ctch4   equ     3h
ctch5   equ     4h
ctch6   equ     5h
;
;       データアドレスオフセット
;
adnrf   equ     900h            ; RFの点数の番地
adrfdt  equ     904h            ; RFデータの先頭番地
adctu1  equ     908h            ; 計測データU1の先頭番地
adctd1  equ     90ch            ;       D1
adctu2  equ     910h            ; 計測データU2の先頭番地
adctd2  equ     914h            ;       D2
adctsem equ     918h            ; SEMデータの先頭番地
adwtlp  equ     91ch            ; 待時間データの先頭番地
adnlp   equ     920h            ; ループ数の先頭番地
adwork  equ     924h            ; データアドレスの退避番地
aderror equ     91ch
; エラーフラグ（待時間データの先頭）
;
;       引数受渡し
;
npara1  equ     12h             ; パラメータの数＊2
npara2  equ     10h             ;       ＊2－2
npara3  equ     24h             ;       ＊4
;
;       WAITデータ　オフセット
;
dummyt  equ     0002h           ; dummy time
bmtime1 equ     0004h           ; ビームonタイム
bmtime2 equ     0006h           ; ビームonタイム微調整
afptime equ     0008h
; ポピュレーション変更用AFP
bmcoolt equ     000ah
; ビーム　クーリング　タイム
rftime1 equ     000ch           ; RF　onタイム
rftime2 equ     000eh           ; RF　onタイム微調整
rfkillt equ     0010h
; RFエフェクト　キル　タイム
cttime1 equ     0012h           ; カウント　タイム（中）
cttime2 equ     0014h           ; カウント　タイム微調整
cttime3 equ     0016h           ; カウント　タイム（前）
cttime4 equ     0018h           ; カウント　タイム微調整
cttime5 equ     001ah           ; カウント　タイム（後）
cttime6 equ     001ch           ; カウント　タイム微調整
```

```
;
;       ＲＦデータ　オフセット
;
bitdtl  equ     0h
bitdth  equ     1h
trdt    equ     10h ; Bit data for WAVETEK
;
;       ループ数
;
lpwait  equ     063Ch
;63Ch or 383h  長周期ＷＡＩＴループ用
lpulse  equ     02h
; コントロールパルス用
;
;       コントロール信号
;
bmstart equ     00010000b
bmstop  equ     00100000b
;
screset equ     00000001b
clock1  equ     00000010b
ctgate  equ     00000100b
clock2  equ     00001000b
ctgrst  equ     00000101b
ctgcl1  equ     00000110b
ctgcl2  equ     00001100b
workend equ     10000000b
workst equ      01000000b
;
rfstart equ     00000001b
rfstop  equ     00000010b
rfon    equ     00000100b
rfoff   equ     10000000b
afpbit  equ     10001000b
abreset equ     01000000b
rfgate  equ     00000000b
off     equ     00000000b
;
;       カウンターコントロールビット
;
holdall equ     00111111b
openall equ     11111111b
open1   equ     10111111b
open2   equ     01111111b
;
;       インプットビット
;
stopbit equ     00000010b
beamon  equ     00010000b
beamoff equ     00100000b
fton    equ     01000000b
ftoff   equ     00100000b
errfrg  equ     10001111b
;
;       シンセサイザーコントロールストロボ
;
remoton equ     10111111b
remoff  equ 11111111b
stroff  equ     10000000b
str01   equ     10000001b
str10   equ     10000010b
str1k   equ     10000100b
str100k equ     10001000b
;str10m equ     10010000b
strDB   equ     10110000b
;
;=======================
;
code    segment
        assume  cs:code,ds:code
;
;       マクロ部インクルード
;
        include lib"iocntr.asm
;
;       プログラムスタート
;
begin:
;
;       レジスタの退避
;
        push    ds
        push    es
        push    ax
        push    bx
        push    cx
        push    dx
        push    di
        push    si
        push    bp
;
;       割り込みのマスク
;
        mov     dx,02h
        mov     al,7fh
        out     dx,al
        mov     dx,0ah
        mov     al,0efh
        out     dx,al
        mov     dx,1fh
        mov     al,0fh
        out     dx,al
;
;       引数の受け渡し
;
        mov     bp,bx
        mov     di,adnlp
        mov     cx,npara1
loop0:
        mov     bx,ds:[bp]
        mov     ds:[di],bx
        add     di,0002h
        add     bp,0002h
        loop    loop0
;
        mov     bp,adnlp
        les     si,ds:dword ptr [bp]
        mov     cx,es:[si]
;
;       スケーラーの初期化
;
counter hold
ctreset
;
; シンセサイザー　ｒｅｍｏｔｅ
;
mov  al,remoton
mov dx,synthe
out dx,al
;
gloop:
        push    cx
        mov     bp,adwork
        mov     di,adnrf
        mov     cx,npara2
loop1:
        mov     bx,ds:[bp]
        mov     ds:[di],bx
        add     di,0002h
        add     bp,0002h
        loop    loop1
;
        mov     bp,adnrf
        les     si,ds:dword ptr [bp]
        mov     cx,es:[si]
;
        %out 3
;
;       メインルーチン
;
```

LAB2CNTR.ASM

```
;
; 1995.10.12 modified WAVETEK control
;
;       終了処理部
;
        pop     cx
        dec     cx
        ercheck aderror
        jcxz    retn
        jmp     gloop
;
;       エラー、ストップ時のフラグセット
; (ercheck マクロ内より)
;
erretn:
        mov     bp,adnlp
        les     si,ds:[bp]
        mov     es:[si],cx
;
;       ＢＡＳＩＣへの復帰
;
retn:
;
        bitcntr bmport,off
;
; シンセサイザー　ｒｅｍｏｔｅ
;
mov  al,remoff
mov dx,synthe
out dx,al
;
;       割り込みマスクの解除
;
        mov     dx,02h
        mov     al,01h
        out     dx,al
        mov     dx,0ah
        mov     al,0e7h
        out     dx,al
        mov     dx,1fh
        mov     al,00h
        out     dx,al
;
;       退避レジスタの復帰
;
        pop     bp
        pop     si
        pop     di
        pop     dx
        pop     cx
        pop     bx
        pop     ax
        pop     es
        pop     ds
;
retbas  proc    far
        iret
retbas  endp
;
code    ends
;
if2
        %out end
endif
```


IOCNTR.ASM

```
;=====================
;       マクロルーチンライブラリ
;
;       for LABCNTR SYSTEM      by  A. Kitagawa
;
;               1991/01/25
;
;                       modified by T. Miyake
;                       to use New Synthesizer
;                       1994/1/25
; 1994/11/18 CAMAC
if1
        %out    IOCNTR    v.11.00 l.01
%out BEAM*2 mode
endif
        %out 1
;
;       LBL & VdG System
;
;=====================
;
;       ビットコントロール：Ｉ／Ｏポートにビットをたてる
;
;         port    :ポートアドレス
;         data    :８ビットのデータ
;
bitcntr macro   port,data
        push    dx
        mov     dx,port
        mov     al,data
        out     dx,al
        pop     dx
        endm
;
;---------------------
;
;       制御パルス：Ｉ／Ｏポートよりパルスを送出する
;
;         adrs    :ポートアドレス
;         before  :送出時のビット
;         after   :送出後のビット
;         length  :パルス長（定周期ループの回数）
;
bpcntr  macro   adrs,before,after,length
        even
        push    dx
        mov     dx,adrs
        mov     al,before
        out     dx,al
        wtloopc length
        mov     al,after
        out     dx,al
        pop     dx
        endm
;
;---------------------
;
;       ビームウェイト：設定したビットが入力されるまで待機
;
;         xx      :設定ビット（０：マスク、１：設定）
;         inport  :インプットポート
;
bmwait  macro   xx
        local   wait
        even
        push    dx
        mov     dx,inport
wait:
        in      al,dx
        and     al,xx
        mov     ah,00h
        cmp     ah,al
        jz      wait
        pop     dx
        endm
;
;---------------------
;
;       エラーチェック：エラーフラグメモリを調べ、条件分岐
;
;         adrs    :エラーフラグの格納番地
;         erretn  :エラー時の飛び先
;
ercheck macro   adrs
        local   cont
        mov     bp,adrs
        les     si,ds:[bp]
        mov     ax,0000
        cmp     ax,es:[si]
        jz      cont
        jmp     erretn
cont:
        endm
;
;---------------------
;
;       エラーストップ検出：入力信号を指定フラグに積算する
;
;         port    :エラーの入力ポート
;         frg     :エラーフラグのマスク（０：マスク）
;         adrs    :エラーフラグの格納番地
;         ah      :入力信号以外のエラー
;
errin   macro   port,adrs,frg
        mov     dx,port
        in      al,dx
        and     ax,frg
        mov     bp,adrs
        les     si,ds:[bp]
        or      es:[si],ax
        endm
;
;---------------------
;
;       定周期ループ：指定回数、空ループする
;
;         wtime   :ループ回数
;
wtloopc macro   wtime
        local   loop3
        even
        push    cx
        mov     cx,wtime
loop3:
        loop    loop3
        pop     cx
        endm
;
;---------------------
;
;       短周期ループ：指定したアドレス内の回数、空ループする
;
;         adwtlp  :ループ回数格納番地の先頭
;         wtime   :オフセット
;
wtloop  macro   wtime
        local   loop3
        even
        nop
        push    cx
        push    es
        push    si
        push    bp
        mov     bp,adwtlp
        les     si,ds:[bp]
        add     si,wtime
        mov     cx,es:[si]
loop3:
        loop    loop3
        pop     bp
        pop     si
        pop     es
        pop     cx
        endm
;
;---------------------
;
;       長周期ループ：二重ループ
;
;         adwtlp  :ループ回数格納番地の先頭
;         wtime1  :オフセット（大ループ）
;         wtime2  :オフセット（小ループ）
;         lpwait  :空ループの回数（大ループ）
;
wtloopl macro   wtime1,wtime2
        local   loop3
        local   loop4
        local   loope
        even
        push    cx
        push    es
        push    si
        push    bp
        mov     bp,adwtlp
        les     si,ds:[bp]
        add     si,wtime1
        mov     cx,es:[si]
        jcxz    loope
loop3:
        push    cx
        mov     cx,lpwait
loop4:
        loop    loop4
        pop     cx
        loop    loop3
loope:
        pop     bp
        pop     si
        pop     es
        pop     cx
        wtloop  wtime2
        endm
;
;---------------------
;
; データ取り込み：ＣＡＭＡＣよりデータを取り込む。
;
; xx:データ格納アドレス
;       yy:チャンネル番号
;
in_data macro   xx,yy
        local   exit
        local   exit2
        local carry
        push    dx
        push    bp
        push    si
        push    ds
        push    es
push bx
;;
cmcset yy,SCALLER1
cmcread rddt
mov bh,00h
shl bx,1h
mov  bp,xx
;
        les     si,ds:dword ptr [bp]
        add     ax,es:[si]
        jc carry
```

```
        jns     exit
        inc     bx
        sub     ax,8000h
        jmp     exit2
carry:
        inc     bx
        inc     bx
exit:
        nop
        nop
        nop
exit2:
        mov     es:[si],ax
        add bx,es:[si+2]
        mov es:[si+2],bx
        pop bx
        pop     es
        pop     ds
        pop     si
        pop     bp
        pop     dx
        endm
;
;-------------------------------------------
;
;       RFデータ転送、RF出力
;
;.....................................................
;
;       (I/O controll sub routine):  指定番地の内容を出力
;
;         ad      :ポートアドレス
;         n       :出力データのオフセット
;         si reg  :RF data address
;
dtout   macro   ad,n
        push    di
        mov     di,si
        add     di,n
        mov     al,es:[di]
        mov     dx,ad
        out     dx,al
        pop     di
        endm
;
;.....................................................
;
;       (Bit Out mode)：ｒｆポートにデータを出力
;
bitout  macro
        dtout   rfbitpl,bitdtl
        bitcntr rfbitpl,00h
        endm
;
;.....................................................
;
;       WAVETEK 5135A mode：シンセサイザーコントロール
;
dtsend macro adr
        mov     al,es:[si]
mov dx,adr
out dx,al
        inc     si
        inc     si
endm
;
strsend macro stdt
        local wait
mov dx,syntstr
mov al,stdt
out  dx,al
mov cx,02h
wait:
loop wait
mov al,stroff
out dx,al
endm
;
trdtout macro   adrs
        push cx
        mov     bp,adrs
        les     si,ds:dword ptr [bp]
add si,trdt
;
dtsend synt100k
strsend str100k
dtsend synt1k
strsend str1k
dtsend synt10
strsend str10
dtsend synt01
strsend str01
dtsend synt10m
strsend strDB
;;
;;      エラーストップ検出
;;
        errin   inport,aderror,errfrg
;;
        pop cx
        endm
;
;.....................................................
;
;       (main routine)
;
;         rfdata  :ｒｆデータの先頭番地
;         aderror :エラーフラグの格納番地
;         errfrg  :エラーフラグ
;
rfdtout macro   rfdata
        even
        push    dx
        push    bp
        push    si
        push    ds
        push    es
;;
        trdtout rfdata
;;
;;      エラーストップ検出
;;
        errin   inport,aderror,errfrg
;;
        pop     es
        pop     ds
        pop     si
        pop     bp
        pop     dx
        endm
;
;-------------------------------------------
;
;       カウンターオープン，ホールドセレクト
;
;         hldsel  :セレクトフラグ      ｏｐｅｎ：全ｃｈオープン
;                                      その他  ：全ｃｈホールド
;
counter macro hldsel
        local openall
local other
mov al,hldsel
cmp al,open
jz openall
sti
jmp other
openall:
clri
other:
endm
;
;-------------------------------------------
;
;       カウンターリセット
;
ctreset macro
execc
endm
;
;-------------------------------------------
;
;       ｒｆ制御セクション
;
rfcntr  macro   before,after,t1,t2
        even
        bpcntr  rfport,rfstart,rfoff,lpulse
        bitcntr rfport,before
        in data adctu1,ctch1
        in data adctd1,ctch2
        in data adctu2,ctch3
        in data adctd2,ctch4
ctreset
        wtloopl t1,t2
        bitcntr rfport,after
        bpcntr  rfport,rfstop,after,lpulse
        endm
;
;-------------------------------------------
;
;       アドレスインクリメント
;
;         n       :インクリメント量
;
adrsinc macro   adress,n
        push    bp
        push    si
        push    ds
        mov     bp,adress
        mov     si,ds:[bp]
        add     si,n
        mov     [bp],si
        pop     ds
        pop     si
        pop     bp
        endm
;
;-------------------------------------------
;
;       アドレスデクリメント
;
;         n       :デクリメント量
;
adrsdec macro   adress,n
        push    bp
        push    si
        push    ds
        mov     bp,adress
        mov     si,ds:[bp]
        sub     si,n
        mov     [bp],si
        pop     ds
        pop     si
        pop     bp
        endm
;
```



```
;
;-------------------------------------------
;
;       カウントセクション
;
;       (sub routine)
;
;       (main routine)
;
;         section :出力されるセクションナンバー
;         n       :not use
;         ni      :データアドレスのインクリメント量
;         t1      :時間パラメータのオフセット
;         t2      :
;
count   macro   section,n,ni,t1,t2
        even
        bitcntr secport,section
counter open
bitcntr ctport,ctgate
        adrsinc adctu1,ni
        adrsinc adctd1,ni
        adrsinc adctu2,ni
        adrsinc adctd2,ni
        wtloopl t1,t2
        bitcntr ctport,off
counter hold
        bitcntr secport,off
        endm
;
;-------------------------------------------
;
;       ビームクーリングセクション
;
bmcool  macro
        even
        wtloop bmcoolt
        endm
;
;-------------------------------------------
;
;       ｒｆキルセクション
;
rfkill  macro
        even
        wtloop rfkillt
        endm
;
;-------------------------------------------
;
;       ｒｆデータアドレスのインクリメント
;
rfadinc macro
        even
        adrsinc adrfdt,0020h
        endm
;
;-------------------------------------------
;
;       ｒｆデータアドレスのインクリメント２
;
rfadinc2 macro
        even
        adrsinc adrfdt,0040h
        endm
;
;-------------------------------------------
;
;       ｒｆデータアドレスのインクリメント３
;
rfadinc3 macro
        even
        adrsinc adrfdt,0060h
        endm
;
;-------------------------------------------
;
;       ｒｆデータアドレスのインクリメント４
;
rfadinc4 macro
        even
        adrsinc adrfdt,0080h
        endm
;
;-------------------------------------------
;
;       ｒｆデータアドレスのデクリメント
;
rfaddec macro
        even
        adrsdec adrfdt,0020h
        endm
;
;-------------------------------------------
;
;       ｒｆデータアドレスのデクリメント２
;
rfaddec2 macro
        even
        adrsdec adrfdt,0040h
        endm
;
;-------------------------------------------
;
;       ｒｆデータアドレスのデクリメント３
;
rfaddec3 macro
        even
        adrsdec adrfdt,0060h
        endm
;
;-------------------------------------------
;
;       ｒｆデータアドレスのデクリメント４
;
rfaddec4 macro
        even
        adrsdec adrfdt,0080h
        endm
;
;-------------------------------------------
;
;       データアドレスのインクリメント
;
ctadinc macro   n
        even
        adrsinc adctu1,n
        adrsinc adctd1,n
        adrsinc adctu2,n
        adrsinc adctd2,n
        endm
;
;-------------------------------------------
;
;       カウントデータの読み込み
;
countin macro
        even
        in data adctu1,ctch1
        in data adctd1,ctch2
        in data adctu2,ctch3
        in data adctd2,ctch4
ctreset
endm
;;
;
;-------------------------------------------
;
;       ＳＥＭ取り込み：ＳＥＭパルスの積算
;
;         xx      :ＳＥＭの格納アドレス
;         yy      :ＳＥＭ読み込みのチャンネル番号
;
st sem macro
ctreset
counter open
endm
;
in sem macro xx,yy
local exit
local exit2
local carry
even
push dx
push bp
push si
push ds
push es
push bx
;;
mov bp,xx
        les     si,ds:dword ptr [bp]
;;
counter hold
cmcset yy,SCALLER2
cmcread rddt
mov bh,00h
shl bx,1h
;;
;;
        add     ax,es:[si]
        jc carry
        jns     exit
        inc     bx
        sub     ax,8000h
        jmp     exit2
carry:
        inc     bx
        inc     bx
exit:
        nop
        nop
        nop
exit2:
        mov     es:[si],ax
        add bx,es:[si+2]
        mov es:[si+2],bx
        ctreset
pop bx
pop es
pop ds
pop si
pop bp
pop dx
endm
;
st beam macro
ctreset
counter open
endm
;
in beam macro xx,yy1,yy2
even
```

```
push dx
push bp
push si
push ds
push es
push bx
;;
;;
counter hold
;
in beam2 xx,yy1,00h
in beam2 xx,yy2,04h
;
        ctreset
pop bx
pop es
pop ds
pop si
pop bp
pop dx
endm
;
in beam2 macro xx,yy,zz
local exit
local exit2
local carry
;
mov bp,xx
        les     si,ds:dword ptr [bp]
add si,zz
;
cmcset yy,SCALLER2
cmcread rddt
mov bh,00h
shl bx,1h
;;
;;
        add     ax,es:[si]
        jc carry
        jns     exit
        inc     bx
        sub     ax,8000h
        jmp     exit2
carry:
        inc     bx
        inc     bx
exit:
        nop
        nop
        nop
exit2:
        mov     es:[si],ax
        add bx,es:[si+2]
        mov es:[si+2],bx
endm
;
;;
;;
;; camac macro routines
;
;
; A Command set (break ax)
;
cmcset macro a,N
mov al,N ;set station number N
mov ah,a ;set sub address A
out nacmnd,ax ;write N,A to Command
endm
;
; Data Read (bl-data high 8bit,ax-data low 16bit)
;
cmcread macro f
local ckdone
in ax,status ;read Status
and ah,lint_ei_i ;clear noX,noQ
mov al,f ;set F (Read LAM reg-mask n)
out contrl,ax ;write F to Command
out camacgo,al ;Camac Go Command
ckdone: in ax,status ;read Status
test ah,done ;check Done
jz ckdone ;if not done  then wait
in ax,datahi ;read Data high
mov bx,ax
in ax,datalow ;read Data low
endm
;
; set I (inhibit line) cycle
;
seti macro
in ax,status
and ah,lint_ei_i ;hold LINT,EI,I
or ah,i_line ;set I
out contrl,ax
endm
;
; clear I (inhibit line) cycle
;
clri macro
in ax,status
and ah,lint_ei ;hold LINT,EI
out contrl,ax
endm
;
; execute C (clear) cycle
;
execc macro
in ax,status
and ah,lint_ei_i ;hold LINT,EI,I
or ah,c_line ;set C
out contrl,ax
endm
;
;=====================
;
%out 2
```

Bibliography

[Abr63] A. Abragam, *The principles of nuclear magnetism*, Oxford, 1963.

[AH73] Y. Akasaka and K. Horii, J. Appl. Phys. **44**, 3372 (1973).

[B+88] J. Bonn et al., in *Bericht Arbeitstreffen Kernphys. Meth. in Festkórperphysik u. Materialforschg*, edited by W. Witthuhn, page 37, Erlangen, 1988.

[BKS80] G. A. Baraff, E. O. Kane, and M. Schlüter, Phys. Rev. B **21**, 5662 (1980).

[BL83] J. Bourgoin and M. Lannoo, *Point defects in semiconductors II*, Springer-Verlag, 1983.

[Con59] D. Connor, Phys. Rev. Lett. **3**, 429 (1959).

[D+76] G. M. DeMunari et al., Phys. Stat. Sol. (a) **34**, 455 (1976).

[DKP+89] M. Deicher et al., Mater. Sci. Eng. **B4**, 25 (1989).

[EDJM69] L. Eriksson, J. A. Davies, G. E. Johanson, and J. W. Mayer, J. Appl. Phys. **40**, 842 (1969).

[F+83] D. Fink et al., Radiat. Eff. **77**, 11 (1983).

[FAD+93] H. P. Frank et al., Hyperfine Interact. **79**, 655 (1993).

[FBLS70] G. Fladda, K. Björkqvist, L.Eriksson, and D. Sigurd, Appl. Phys. Lett. **16**, 313 (1970).

[FDE+94] H.-P. Frank et al., Mat. Sci. Forum **143–147**, 135 (1994).

[FGP89] P. M. Fahey, P. B. Griffin, and J. D. Plummer, Rev. Mod. Phys. **61**, 289 (1989).

[FSD+92] B. Fischer et al., Mater.Sci.Forum **83-87**, 269 (1992).

[FSF+93] B. Fischer et al., Nucl. Instr. Meth. B **80/81**, 201 (1993).

[Gil80] L. A. Gilifalco, *Atomic migration in crystal*, Kyouritu Syuppan, 1980.

[GS83] W. Gehlhoff and K. H. Segsa, Phys. Stat. Sol. (b) **115**, 443 (1983).

[H+92] J. Haase et al., Chem. Phys. Letters **193**, 274 (1992).

[Has66] R. R. Hashiguti, J. Phys. Soc. Jpn. **21**, 1927 (1966).

[HHS69] M. Hirata, M. Hirata, and H. Saito, J. Phys. Soc. Jpn. **27**, 405 (1969).

[HK91] D.-Y. Han and H. Kessemeier, Phys. Rev. Lett. **67**, 346 (1991).

[HNN+76] H. Hamagaki, K. Nakai, Y. Nojiri, I. Tanihata, and K. Sugimoto, Hyperfine Interact. **2**, 187 (1976).

[HNW87] R. D. Harris, J. L. Newton, and G. D. Watkins, Phys. Rev. B **36**, 1094 (1987).

[Hoh86] M. Hohne, Phys. Stat. Sol. (b) **138**, 337 (1986).

[Irv62] J. C. Irvin, Bell. Syst. Tech. J. **41**, 387 (1962).

[K+86] E. Kanda et al., editors, *Denshi ion beam handbook*, Nikkan Kougyou Shinbun, 1986.

[kG82] J. keissl and W. Gehlhoff, Phys. Stat. Sol. (b) **112**, 695 (1982).

[M+92] T. Minamisono et al., Phys. Rev. Lett. **69**, 2058 (1992).

[MB93] D. Maroudas and R. A. Brown, Phys. Rev. B **47**, 15562 (1993).

[Min85] T. Minamisono, *Beta decay and hyperfine interactions*, J.C. Baltzer, 1985.

[MM74] R. E. McDonald and T. K. McNab, Phys. Rev. C **10**, 946 (1974).

[MM76] R. E. McDonald and T. K. McNab, Phys. Rev. B **13**, 39 (1976).

[MNDA83] T. Minamisono, Y. Nojiri, B. I. Deutch, and K. Asahi, Hyperfine Interact. **15/16**, 543 (1983).

[MNO81] T. Minamisono, Y. Nojiri, and S. Ochi, Phys. Lett. **106B**, 38 (1981).

[MNS74] T. Minamisono, Y. Nojiri, and K. Sugimoto, Nucl. Phys. **A236**, 416 (1974).

[Mos80] T. S. Moss, editor, *Handbook on semiconductors*, North-Holland, 1980.

[MSA+98] T. Minamisono et al., Z. Nat.forsch. A, Phys. Phys. Chem. Kosmophys. **53A**, 293 (1998).

[MSS+90a] H. Metzner et al., Phys. Rev. B **42**, 11419 (1990).

[MSS+90b] H. Metzner et al., Hyperfine Interact. **60**, 769 (1990).

[MY81] T. Minamisono and Y.Nojiri, Hyperfine Interact. **9**, 437 (1981).

[NG70] J. C. North and W. M. Gibson, Appl. Phys. Lett. **16**, 126 (1970).

[NG71] J. C. North and W. M. Gibson, Proc. 1st Int. Conf. on Ion Implantation , 143 (1971).

[NSW85] J. R. Niklas, J.-M. Spaeth, and G. D. Watkins, in *Proc. MRS*, volume 46, San Francisco, 1985.

[NVP89] C. S. Nichols, C. G. Van de Walle, and S. T. Pantelides, Phys. Rev. B **40**, 5484 (1989).

[ONM+93] T. Ohtsubo et al., Hyperfine Interact. **80**, 1051 (1993).

[S+66] K. Sugimoto et al., J. Phys. Soc. Jpn. **21**, 213 (1966).

[S+86] N. A. Stolwjik et al., Appl. Phys **A39**, 37 (1986).

[SB73] D. Sigurd and K. Björkqvist, Radiat. Eff. **107**, 209 (1973).

[SFD+92] W. Seelinger et al., Nucl. Instr. Meth. B **63**, 173 (1992).

[SH64] R. K. Sundfors and D. F. Holcomb, Phys. Rev. **136**, A810 (1964).

[SHM95] D. Surono, F.-J. Hambsch, and P. W. Martin, Hyperfine Interact. **96**, 23 (1995).

[SJF78] G. Schirmer, U. Jahn, and H. Frey, Wiss. Z. der Friedrich-Schiller-Universität Jena **27**, 199 (1978).

[Sli90] C. P. Slichter, *Principles of magnetic resonance*, Springer-Verlag, 3 edition, 1990.

[Sta98] M. Stavola, editor, *Identification of defects in semiconductors*, Academic Press, 1998.

[SW56] R. G. .Shulman and B. J. Wyluda, Phys. Rev. **103**, 1127 (1956).

[Syo76] K. Syouno, *Handoutai Gijyutu*, Tokyo university Press, 1976.

[T+76] M. Tanaka et al., Nucl. Phys. A **263**, 1 (1976).

[Tar91] E. Tarnow, Europhys.Lett. **16**, 449 (1991).

[TW80] J. R. Troxell and G. D. Watkins, Phys. Rev. B **22**, 921 (1980).

[Wat63] G. D. Watkins, J. Phys. Soc. Jpn. **18, Suppl. II**, 22 (1963).

[Wat69] G. D. Watkins, IEEE Trans. Nucl. Sci. **NS–16**, 13 (1969).

[Wat75] G. D. Watkins, Phys. Rev. B **12**, 5824 (1975).

[WDG+89] T. Wichert et al., Appl. Phys. **A48**, 59 (1989).

[Zie92] J. F. Ziegler, editor, *Handbook of ion implantation thechnology*, North-Holland, 1992.